3-2022

Global Sporadic-E Climatological Analysis using GPS Radio Occultation and Ionosonde Data

Travis J. Hodos

Global Sporadic-E Climatological Analysis using GPS Radio Occultation and Ionosonde Data

THESIS

Travis J. Hodos, Capt, USAF

AFIT-ENP-MS-22-M-096

DEPARTMENT OF THE AIR FORCE
AIR UNIVERSITY

AIR FORCE INSTITUTE OF TECHNOLOGY

Wright-Patterson Air Force Base, Ohio

AFIT-ENP-MS-22-M-096

GLOBAL SPORADIC-E CLIMATOLOGICAL ANALYSIS USING GPS RADIO OCCULTATION AND IONOSONDE DATA

THESIS

Presented to the Faculty

Department of Engineering Physics

Graduate School of Engineering and Management

Air Force Institute of Technology

Air University

Air Education and Training Command

in Partial Fulfillment of the Requirements for the

Degree of Master of Science in Applied Physics

Travis J. Hodos, B.S.

Capt, USAF

March 2022

AFIT-ENP-MS-22-M-096

GLOBAL SPORADIC-E CLIMATOLOGICAL ANALYSIS USING GPS RADIO OCCULTATION AND IONOSONDE DATA

THESIS

Travis J. Hodos, B.S.
Capt, USAF

Committee Membership:

Maj D. Emmons, Ph.D.
Chair

E. Dao, Ph.D.
Member

Lt Col O. Nava, Ph.D.
Member

Abstract

A climatology of sporadic-E (Es) derived from a combined data set of GPS radio occultation (GPS-RO) and ground-based ionosonde soundings is presented for the period from September 2006 to February 2019. The ionosonde soundings were measured using the Lowell Digisonde International (LDI) Global Ionosphere Radio Observatory (GIRO) network consisting of 65 sites and 13,141,060 total soundings. The GPS-RO observations were taken aboard the Constellation Observing System for Meteorology, Ionosphere, and Climate (COSMIC) satellites and processed using two binary Es detection algorithms, totaling 9,072,922 occultations. The first algorithm is an S_4 amplitude threshold calibrated to the occurrence of any blanketing Es (fbEs) with no lower limit on frequency, and the second is a threefold phase perturbation criteria calibrated to the occurrence of fbEs $\geq$ 3 MHz. It was found that Es primarily occurs in mid-latitude regions (10^o-60^o geomagnetic latitude) in the late afternoon and early evening (1500-2000SL). Auroral Es occurs later, with a peak occurrence rate (OR) between 1900-2300SL. Es has a strong seasonal dependence, where Es ORs are much higher during local summer. The effects of geomagnetic storming and solar cycle on Es ORs are also studied. Using the geomagnetic indices Kp, AE, DST, and IMF Bz, a strong positive correlation between auroral Es and geomagnetic storming was found. Equatorial and mid-latitude Es is not strongly correlated with geomagnetic activity. The solar cycle, as a function of the relative sunspot number (R), has a strong negative correlation with Es ORs. Due to a shift in the prevailing wind patterns during solar active periods, Es ORs actually decrease even though total ionosphere ionization rates increase.

Acknowledgements

First, and foremost, I would like to thank my wife and three boys. I could have easily lost myself in my work, but you never failed to show me what is most important in my life.

I would also like to thank my advisor and mentor, Maj Dan Emmons. Your feedback was always second to none, and I never walked out of your office without a solid plan on where to go next. Additionally, I would also like to extend my gratitude to my other committee members, Lt Col Omar Nava and Dr. Eugene Dao. You were both very kind and generous, and had important insight on my thesis.

Lastly, I want to thank God for giving me the strength to thrive in this opportunity. *"I sought the LORD and He answered me, And rescued me from all my fears."* (Psalm 34:4)

Travis J. Hodos

Table of Contents

Page

List of Figures

List of Tables

I. Introduction

The ionosphere is a complicated domain for military operations. The combination of our standard atmospheric dynamics and the addition of electromagnetic Maxwellian mechanics creates a sizeable burden for scientists and operators alike. Therefore, any ability to generate some situational awareness in the ionosphere can greatly enhance all operations. In particular, the Department of the Air Force and Department of Defense have been trying to utilize the ionosphere for advanced operations. In many ways, sporadic E (Es) is to HF radio waves what clouds are to satellite based imagery. Es can cause signal degradation or complete blackouts for HF, Ultra High Frequency (UHF), and Very High Frequency (VHF) bands (Davies and Hartmann, 1997; Zeng and Sokolovskiy, 2010). Over-the-horizon radar (OTHR) uses an HF radio signal reflecting off the ionosphere to image locations beyond line of sight (Fabrizio, 2013). The presence of sporadic E (Es) layers decreases the effective range and accuracy of OTHR, and can give false readings from ground clutter echoes in extreme cases (Coleman, 1998; Headrick et al., 2008). In high latitude regions, such as the Northwest Passage, Es is the dominant disturbance to OTHR performance since the region is usually dominated by calm seas and is free of man-made ground clutter (Thayaparan and MacDougall, 2005). Radio communications within the HF band have been used for military and civilian operators for many years, especially in the high latitude and aviation sectors, due to their ability to transmit long distances using relatively light, portable devices (Jain et al., 2018). Es for communication purposes can be both a positive and negative. Radio operators can use Es layers to transmit signals over great distances which would normally be restricted to line of sight (Neubeck, 1996). Negatively, Es layers can cause distortion and interference, potentially creating intermittent HF blackouts (Rice et al., 2011). HF geolocation is a technique to pinpoint radio transmitters using a passive receiver. Using an in-

coming signal, highly calibrated instruments and well tuned algorithms at a single sight location (SSL), a direction of arrival (DoA) and elevation angle are calculated. Coupled with knowledge of the ionospheric propagation path, an estimated source is located with a range of 2000 km, and an accuracy of approximately 10% (Jain et al., 2018). Es is a large deviation from the standard ionosphere behavior, so the presence of it significantly reduces the accuracy of HF geolocation (Ritchie and Honary, 2009). Lastly, Es can cause Global Positioning Satellite (GPS) signal scintillation leading to navigation errors and data loss (Buchert et al., 2015; Kintner et al., 2007; Zeng and Sokolovskiy, 2010). Ultimately, Es layers drastically alter the behavior of HF signals, and other frequency bands. Yet, the formation mechanisms are not completely understood and the ability to forecast Es effectively.

There are typically two ingredients to Es formation, and both are required to form strong, long lasting layers. The first is meteoric ablation to deposit heavy metals in the atmosphere. Next is wind-shear driven convergence of the ions into a strong, thin layer. These two ingredients also contribute to a slow recombination process which accounts for the long-lived nature of Es (Haldoupis, 2011). Due to formation altitudes and chemical composition, Es has been very difficult to predict. Early studies capitalized on ground based ionosondes to build a global climatology (Smith, 1957). However, ground based observations can not be corrected over water, and the ground stations are large and expensive. Therefore, there are large spatial gaps in the data sets which require significant interpolation between points.

The advent of GPS Radio Occultation (GPS-RO) provides a valid alternative to ground ionosondes. GPS-RO works by measuring the GPS phase and amplitude signals from another Low Earth Orbit (LEO) satellite. Many studies have used GPS-RO to monitor Es layers in the ionosphere (Arras and Wickert, 2018; Chu et al., 2014; Wu et al., 2005; Yu et al., 2019). After early efforts proved successful, such as

the Challenging Minisatellite Payload (CHAMP), the National Oceanographic and Atmospheric Administration (NOAA) launched the Constellation Observing Satellite for Meteorology, Ionosphere, and Climate (COSMIC) constellation of satellites in 2006. The COSMIC constellation provides a perfect data set to map the atmosphere in near real time using signals between the six COSMIC satellites and the GPS constellation.

Carmona (2021) compared five leading GPS-RO processing techniques for determining Es with ground based Digisonde observations. Using all GPS-RO observations within a 100 km radius of each Digisonde site, Carmona (2021) concluded the Yu et al. (2019) S_4, signal amplitude technique aligned best with blanketing Es, fbEs, without a lower limit on intensity. The Chu et al. (2014) phase perturbation technique was best at determining when a fbEs $\geq$ 3 MHz occurred. This study is a continuation of the Carmona (2021) analysis by applying the two techniques to a global climatology using the entirety of the 13 year COSMIC data set. While previous studies have completed global climatologies, each of them have used a small subset COSMIC data, or a limited geographical subset. Here, we provide global occurrence rates from 2006-2019 for two Es intensity thresholds: 3 MHz, and no lower limit. Additionally, ionosonde data is incorporated into the climatology to provide confidence in the GPS-RO estimates.

Chapter II will provide a background on Es and GPS-RO, as well as relevant factors that may contribute to perturbations in Es rates. In Chapter III we will apply the best fit techniques to develop a baseline global climatology for quiet geomagnetic conditions. For each technique, an annual, seasonal, monthly, and diurnal analysis will be completed. In Chapter IV, we will analyze the relationship between solar and geomagnetic activity and global Es rates. In particular, the Kp, AE, DST, Bz, and Relative Sunspot Numbers will be compared with Es activity.

II. Background

The purpose of this chapter is to introduce key concepts pertaining to Es. After giving a brief review of the ionosphere and ionosonde soundings, the underlying principles behind Es composition and formation will be covered. Next, GPS-RO will be introduced and the underlying mechanisms that make satellite based observations possible will be covered, as well as best practices. Lastly, this chapter will outline various geomagnetic and solar activity indices that will be used in the climatology analysis from Chapter III, and heavily in Chapter IV.

2.1 Ionosphere & Ionosondes

The ionosphere is the portion of the atmosphere which contains a significant, semi-permanent, collection of free electrons and ions. It is primarily formed through ionization from solar UV radiation, while some ionization comes from energetic particle collisions (Schunk and Nagy, 2009). Recombination between free electrons and ions is not instantaneous. The ionosphere is present even at night when there is no solar ionization, though electron concentrations are considerably lower (Figure 1).

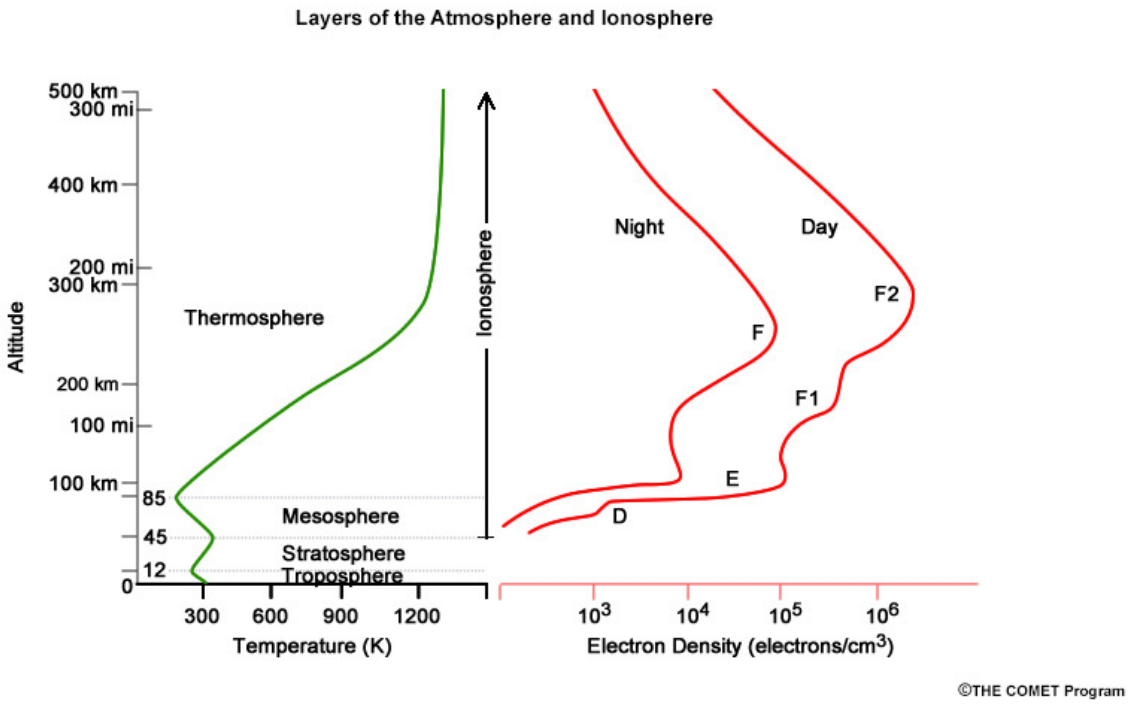

Figure 1. The green line depicts the temperature profile of the idealized atmosphere. The red lines indicate the electron density of the ionosphere. The left red line is the electron density profile at night, and the right red line is the daytime profile (UCAR, 2018).

Earth's ionosphere begins around 60 km in altitude, and can reach over 1000 km. There are four layers within the ionosphere; D, E, F1, F2 (Figure 1). The layers are characterized by their electron density and chemical compositions. The first layer to be discovered was the 'Electric' region, later shortened to E. The E layer is dominated by molecular NO^+ and O_2^+, and typically spans from 90-140 km (Figure 2). It is characterized by a local maxima in the electron density (Solomon, 2006). The lowest region is the D region, which has the most complex chemistry. The D region contains the lowest concentration of ions and electrons, but it is important after solar flares when it can become significantly amplified (Schunk and Nagy, 2009). Above the E region is the F region, which is further separated into the F1 and F2 regions. The F1 region is dominated by O^+ ions, and is more heavily impacted by solar ionization so it has a sharp diurnal reliance to the electron concentration. In

the F2 region, transport processes such as ambipolar diffusion and magnetic drifts are faster than the chemical processes. Additionally, recombination of O^+ is relatively slow compared to NO^+ and O_2^+. Therefore, the F2 region typically has the highest ion and electron concentration and tends to have minimal loss at night (Schunk and Nagy, 2009).

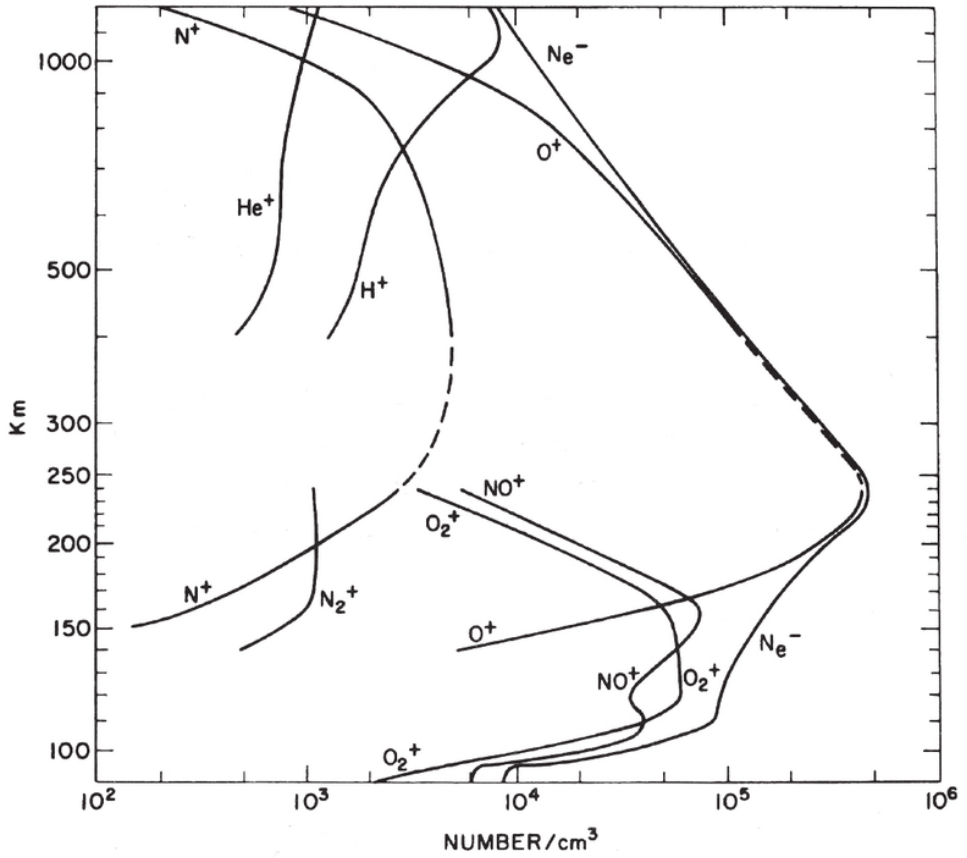

Figure 2. The ideal chemical composition of the ionosphere. As a quasi-neutral plasma, the electron density (N_e^-) equals the number of ions, so the electron density line is the sum of ion densities at a given altitude. In the E-layer altitudes (90-115 km), NO^+ and O_2^+ dominate (Johnson, 1966).

Collectively, the ionosphere behaves like a plasma due to the abundance of ions and electrons. A plasma is defined as a quasineutral gas of charged and neutral particles which exhibits collective behavior (Chen, 2012). As such, bodies within the ionosphere are subject to the standard laws of physics that govern the neutral atmosphere, as

well as the laws of electromagnetism (Maxwell's equations). Of utmost importance to radio wave propagation in the ionosphere is the critical frequency which depends on the plasma frequency and the signal frequency. Within a plasma, the plasma frequency is the frequency with which a perturbed electron will oscillate about it's equilibrium, given by

$$\omega_p[rad/s] = \sqrt{\frac{n_e e^2}{m_e \epsilon_o}}, \tag{1}$$

where n_e is the number density of electrons (m^{-3}), e is the elementary charge (C), m_e is the mass of an electron (kg) and ϵ_o is the permeability of free space ($F * m^{-1}$). Dividing the plasma frequency by 2π and evaluating the constants in the equation, the electron density can be approximated by the equation

$$f_p[Hz] = 9\sqrt{n_e}. \tag{2}$$

Within a cold, unmagnetized plasma the dispersion relation for an electromagnetic wave is given by

$$\frac{c^2 k^2}{\omega^2} = 1 - \frac{\omega_p^2}{\omega^2}, \tag{3}$$

where $ck/w = n$, the index of refraction. Thus, we can see that

$$n \ = \sqrt{1 - \frac{\omega_p^2}{\omega^2}}, \tag{4}$$

where ω_p is the plasma frequency and ω is the signal frequency of the electromagnetic wave. As ω approaches ω_p, we see that n approaches zero, which is a cutoff, and we call this signal frequency the critical frequency. At the critical frequency, the signal is no longer transmitted through the plasma, and is instead reflected back to the transmitter (Chen, 2012). For a cold, magnetized plasma, the dispersion relation is

alternatively given by

$$\frac{c^2k^2}{\omega^2} = 1 - \frac{\omega_p^2}{\omega^2}\frac{\omega^2 - \omega_p^2}{\omega^2 - \omega_H^2}, \tag{5}$$

where w_H is the upper hybrid frequency. It is the combination of these two dispersion relations that provides the basis for ionosonde soundings.

Ionosondes use a ground based pulse transmitter to send a signal vertically into the atmosphere. When the signal reaches the critical frequency, it is reflected back to the ground station where the receiver collects the signal. Based on the time between transmission and reception, the data processor calculates a virtual height, which simply assumes the signal moves at the speed of light. To get the real height, an inversion program is run to account for slower transmission through a the plasma below the reflection point. Per Equation 2, the plasma frequency is directly proportional to the electron density, so the ionosondes provides a measurement of the ionosphere electron density. To generate a full raw ionogram, the ionosonde is run for a full range of transmission frequencies. The last step is to scale the ionogram with a scaling routine, which determines real heights, layer heights, peak frequencies, and other important indices.

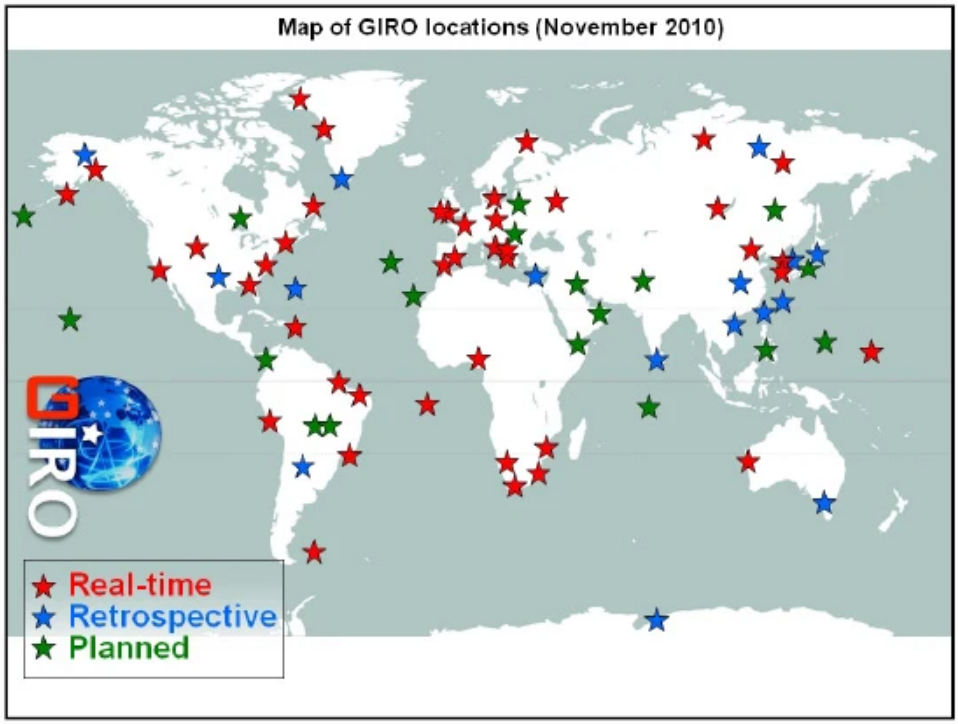

Figure 3. Global coverage of the GIRO Digisonde network as of November 2011 (Reinisch and Galkin, 2011).

The ionosondes used for this study are from the Global Ionospheric Radio Observatory (GIRO) DIDBase network of Digisonde observations as shown in Figure 3 (Reinisch and Galkin, 2011). Ionosondes can be analyzed by hand or with an automated software. Digisondes use the Automatic Real-Time Ionogram Scaler with True height (ARTIST) software for auto-scaling ionograms (Reinisch and Galkin, 2011). Following Merriman et al. (2021), ARTIST-4.5 and all earlier versions of the software were unreliable in accurately depicting foEs and fbEs values, whereas ARTIST-5 was found to be reliable compared to hand scaled ionograms. Thus, this study will only utilize ARTIST 5 auto-scaled soundings from the 65 Digisonde sites analyzed by Merriman et al. (2021). For the year range 2006-2019, this results in a total of 13,141,060 Digisonde soundings.

2.2 Sporadic-E

Es are unusually strong concentrations of ions that form in the E-layer of the ionosphere. It is characterized by having higher ion content than the surrounding E-layer of the ionosphere (Schunk and Nagy, 2009). This thin layer of enhanced ion concentrations can alter the density structure of the ionosphere, significantly impacting the behavior of high frequency (HF) wave behavior. In extreme cases, sporadic-E is accountable for ion concentrations higher than the F2 peak, completely blanketing the rest of the ionosphere from the ground perspective, acting as a barrier to HF propagation.

Spatially, Es forms as cloud like structures (Hysell et al., 2009). The layers are typically not uniform and are turbulent in nature (Hysell et al., 2009). Es normally form between 90-120 km in altitude, with a peak occurrence around 105 km. The vertical thickness distribution has a maximum at approximately 1.5 km, but the distribution varies between 0.6-4.0 km (Zeng and Sokolovskiy, 2010), so Es layers are thin relative to typical ionospheric scale sizes in the tens and hundreds of kilometers. There are large variations in the lengths of Es; the average is 100 km, but lengths can reach over 500 km (Cathey, 1969; Maeda and Heki, 2015). Es measured by ionosondes are typically reported with an foEs and fbEs. foEs is the ordinary critical frequency of Es, and refers to the peak O-wave frequency returned by the Es. fbEs is the blanketing critical frequency of Es, and refers to the highest frequency in which the Es is opaque. At the fbEs, and all signal frequencies below, the Es layer completely inhibits signals from penetrating. The fbEs is always less than or equal to the foEs. Furthermore, in-between the foEs and fbEs, the signal can still penetrate the Es, but is partially blocked or perturbed (Reddy and Matsushita, 1968).

Es chemistry is driven by meteoric ablations. When meteors enter our atmosphere, they deposit iron (Fe), magnesium (Mg), and other metallic ions. Recombination rates

for Mg^+ and Fe^+ are much slower than the surrounding O_2^+ and NO^+ ions. Fe^+ and Mg^+ recombination coefficients are on the order of 10^{-12} (cm^3s^{-1}), whereas O_2^+ and NO^+ are around 10^{-7} (cm^3s^{-1}), five orders of magnitude faster (Bates and Dalgarno, 1962). Meteoric ablations account for the long-lived ion enhancement, but it is the wind shear theory that accounts for Es formation.

Natural diurnal and semi-diurnal thermospheric wind patterns create a wind shear mechanism within the E-layer. The motion of electrons and ions within the E-layer creates a $\vec{v_n} \times \vec{B}$ Lorentz force with the Earth's magnetic field. As shown in Figure 4, when a vertically oriented wind shear forms, opposing Lorentz forces converge the ions into a shallow, thin Es layer. Through standard tidal motion, the Es layer will slowly descend in altitude, and ultimately the Es persists until the layer sinks low enough that the collisional recombination rates dissipate the metallic ions (Haldoupis, 2011). The wind shear model in Figure 4 breaks down for two regions on the Earth. At the geomagnetic equator, where the inclination angle is 0^o, the meridional wind shear has no Lorentz force since the magnetic field and flow velocity (neutral wind) are parallel. The zonal wind shear also fails since the tendency would be to move the electrons vertically, but the electrons are highly magnetized and are constrained to their respective magnetic lines. Vertical ion motion creates a charge separation and an electric field that opposes ion convergence. In contrast, at the poles where the inclination is nearly 90^o, the zonal wind shear component does not create vertical convergence between the layers. The meridional wind shear mechanism breaks down because the neutral winds in the north/south direction at the poles are typically small (Haldoupis, 2011).

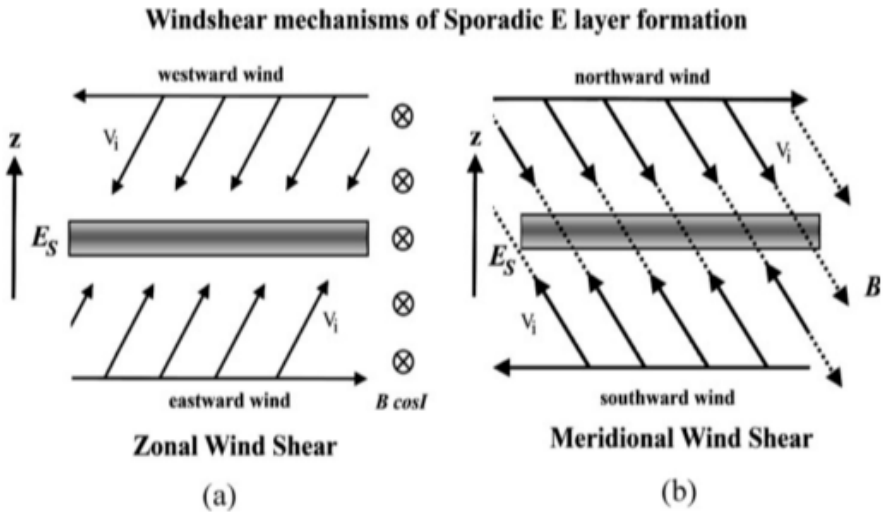

Figure 4. Vertical ion convergence mechanisms for meridional (a) and zonal (b) wind shear (Haldoupis, 2011)

Sporadic-E occurrence rates depend on many factors. As previously mentioned, there are two main ingredients for the formation of Es: meteor ablations and wind shear. Therefore, Es hot spots will occur during times and in regions where these two ingredients are most abundant. As a first guess, one may assume meteor deposits are randomly distributed over the globe. However, Haldoupis et al. (2007); Singer et al. (2004) showed there is a strong seasonal dependence on meteoric deposit rates. In particular, the summer hemisphere will meteor showers up to a full order of magnitude in excess of the winter hemisphere.

Per the wind shear model, areas with an inclination greater than about 5^o and less than 85^o should satisfy the necessary conditions per Mathews (1998):

$$w = \frac{U\cos(I)\sin(I) + rV\cos(I)}{1 + r^2}, \tag{6}$$

where I is the magnetic field inclination, r is the ratio of ion-neutral collision frequency and ion-cyclotron frequency. V and U denote zonal and meridional wind shears, respectively. While high latitude auroral Es is rare, it is not impossible. Additionally, it

is not as well understood as mid latitude or equatorial Es, and the driving mechanisms are likely caused by electric fields rather than neutral winds. Auroral Es typically has an fbEs that is 96% foEs, has maximum occurrence rates ranging from 1700-0100 solar local time, does not see a significant seasonal variation, and is strongly correlated with visible aurora. Additionally, since the magnetic field lines are nearly vertical, Es layers tend to be slanted (Whitehead, 1970).

Previous global Es climatological studies have shown seasonal, latitudinal, and magnetic field dependence. One of the earliest comprehensive sporadic-E climatological studies was completed by Smith (1957) using solely ionosonde data. The Smith (1957) study showed Es was primarily in the mid latitudes, and there was little to no occurrences of Es along the geomagnetic equator, where the inclination is near zero, and at high latitudes. Furthermore, Es rates are lower around the South Atlantic Anomaly (SAA), where the Earth's magnetic field is weaker. GPS-RO has been utilized more frequently in since COSMIC was launched in 2006, and has been used to gain further insight into Es. Arras and Wickert (2018), Wu et al. (2005), Yu et al. (2019), Chu et al. (2014) utilized the COSMIC (see Section 3.1) constellation to measure global Es. Each study only focused on a limited subset of the available COSMIC constellation data and used varying techniques to extract Es parameters from the GPS-RO measurements, resulting in large differences in Es occurrence rates between studies.

2.3 Global Positioning Satellite Radio Occultation (GPS-RO)

Global positioning satellite radio occultation (GPS-RO) is a technique in which the transmitted GPS L1 (1.575 GHz) and L2 (1.227 GHz) signals are measured by a low earth orbit (LEO) satellite. When the orbit geometries align such that the signal path intersects the atmosphere, one can deduce various atmospheric and ionospheric

characteristics by analyzing the signal's amplitude and phase. Non-ionospheric phase contributions (path delay, system clock delay, etc.) can be eliminated by using both the L1 and L2 signals (Mannucci et al., 1999). Figure 5 shows an example signal path for the GPS-RO geometry. The tangent point is the estimated observation point and is calculated as the closest point to Earth's surface along the signal path (impact parameter). The signal path is estimated to be a straight line between the GPS and COSMIC satellite at ionospheric altitudes. In reality, the signal is refracted by the atmospheric plasma with an index of refraction approximated by

$$N_s = 1 - \frac{40.2 n_e}{f_s^2}, \tag{7}$$

where n_e is the electron density (m^{-3}) and f_s is the signal frequency (Hz). However, the refraction is small enough to make the straight line approximation accurate within 3-5 kilometers (Schreiner et al., 2007).

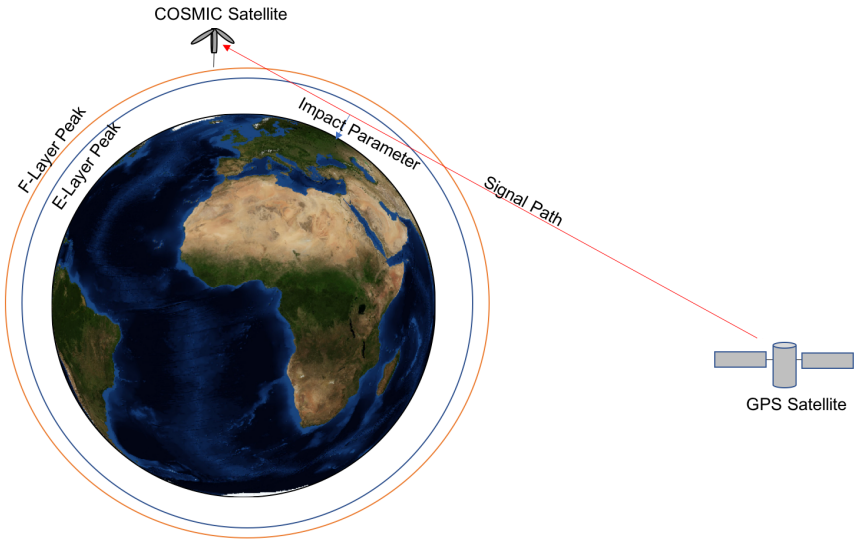

Figure 5. A graphical representation of the GPS-RO geometry around Earth. The signal path is assumed to be a straight line through the ionosphere. The tangent point is the closest point to Earth's surface along the signal path corresponding to the impact parameter (Gooch et al., 2020).

For this study, we used the COSMIC I constellation occultation sounding data

(Schreiner et al., 2014). COSMIC consists of six satellites in circular orbits, with inclinations of 72 degrees and altitudes of 800 km (Fong et al., 2008), and was operational from 2006 to 2019. COSMIC transmitted approximately 2500 occultations per day from 2006 thru 2013. Due to normal satellite degradation, the occultation rate steadily decreased after 2013 until COSMIC was taken offline in early 2019. Standard coverage for one day is shown in Figure 6, where each red dot represents one occultation.

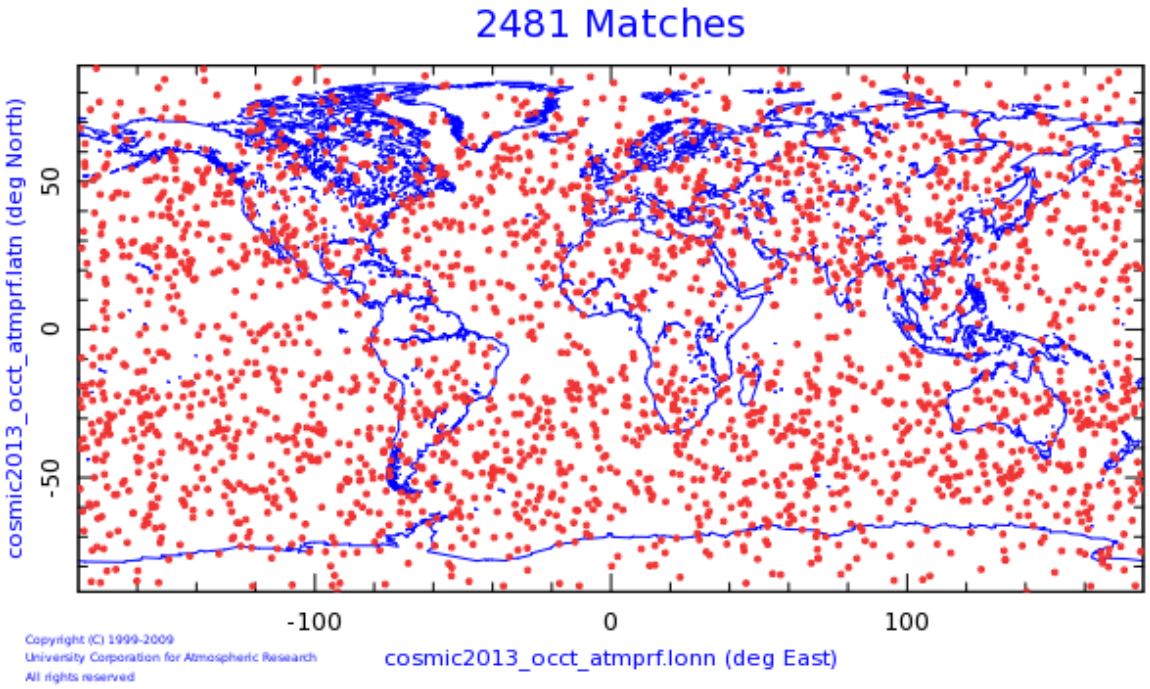

Figure 6. A sample of the global coverage available from GPS-RO over a single day. This map is from 29 June 2020, and each red dot represents a single occultation (CDAAC, 2020).

The COSMIC data only provides satellite positions, signal phase, and amplitude data, so accurately deciphering the data set is difficult. Many previous studies have utilized various techniques to analyze the GPS-RO data generated by COSMIC for Es analysis. Carmona (2021) analyzed numerous Es GPS-RO techniques, outlined in Table 1, and compared them against Digisonde data analyzed with ARTIST-5 from the Merriman et al. (2021) data set. By the Carmona (2021) analysis for the rate of

Table 1. A summary of the binary sporadic-E criteria for each of the five GPS-RO techniques (Carmona, 2021).

Technique	Criteria
Arras	L_1 SNR standard deviation > 0.2
Niu	Maximum total electron content (TEC) perturbation gradient (S_{max}) > 0.12 TECU/km
Chu	1) L_1 and L_2 phase perturbation > 5 cm 2) Ratio of L_1 and L_2 within $[1.2, 1.9]$ 3) Amplitude of normalized L_1 SNR perturbation > 0.01
Yu	Maximum L_1 $S_4 > 0.66$
Gooch	fbEs calculated from total electron content perturbation and 170 km effective sporadic-E length > 3 MHz

any measurable fbEs, it was found that the Yu et al. (2019) L1 $S_{4,max}$ technique was most accurate, with bootstrapping averages shown in Figure 7. With a 3 MHz fbEs cutoff, the Chu et al. (2014) phase perturbation technique was most accurate, with a comparable bootstrapping analysis shown in Figure 8.

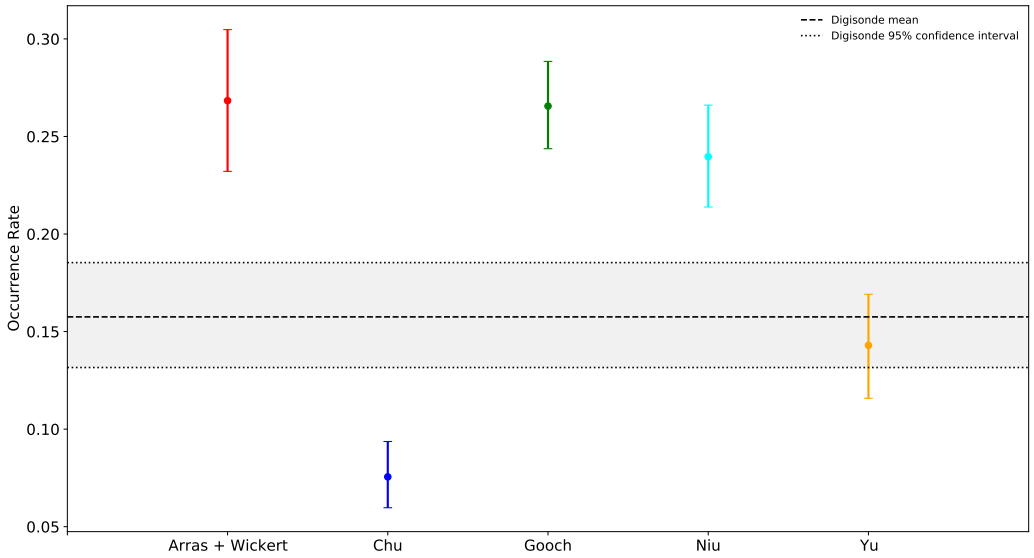

Figure 7. Bootstrap calculated means and 95% confidence intervals for each GPS-RO technique compared to the ionosonde rates for all occurrences of fbEs (Carmona, 2021).

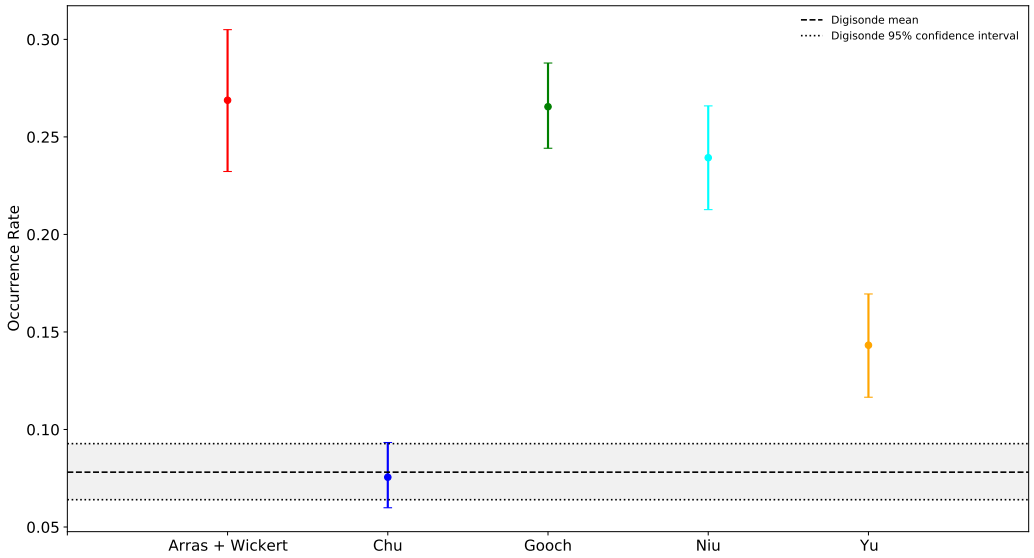

Figure 8. Bootstrap calculated means and 95% confidence intervals for each GPS-RO technique compared to the ionosonde rates for fbEs $\geq$ 3 MHz (Carmona, 2021).

2.3.1 Chu Phase Perturbation Technique.

Chu et al. (2014) introduced threefold criteria as a binary check for Es. The technique takes ingests COSMIC 1-Hz ionospheric phase (ionPhs) data. After running the 1-Hz data through a high pass filter, the detrended L1 (1.575 GHz) and L2 (1.227 GHz) GPS channels had to meet the following three criteria: (1) the amplitude of the L1 and L2 phase perturbations had to be $\geq$ 5 cm, (2) the ratio of L1 excess phase (ΔL1) to L2 excess phase (ΔL2) must be between 1.5 and 1.8, and (3) the L1 amplitude perturbation must be $>$ 0.01. Carmona (2021) used a slightly looser ΔL1/ΔL2 of 1.2 to 1.9, so we have used the same range. The excess phase is given by

$$\Delta L = \frac{40.323}{f^2} TEC, \tag{8}$$

where TEC is the total electron content. The amplitude perturbation in the first step was an initial check to make sure the layer met a minimum size threshold. Since

the excess phase is related to the inverse square of the carrier frequency, the ratio of ΔL1/ΔL2 would ideally equal 1.65, so the 1.2 to 1.9 buffer allows for slight variation. The third step checks for a significant deviation from the background noise to ensure a clearly defined Es layer. Figure 9 shows a sample GPS-RO measurement and the calculated criteria required for the three step check.

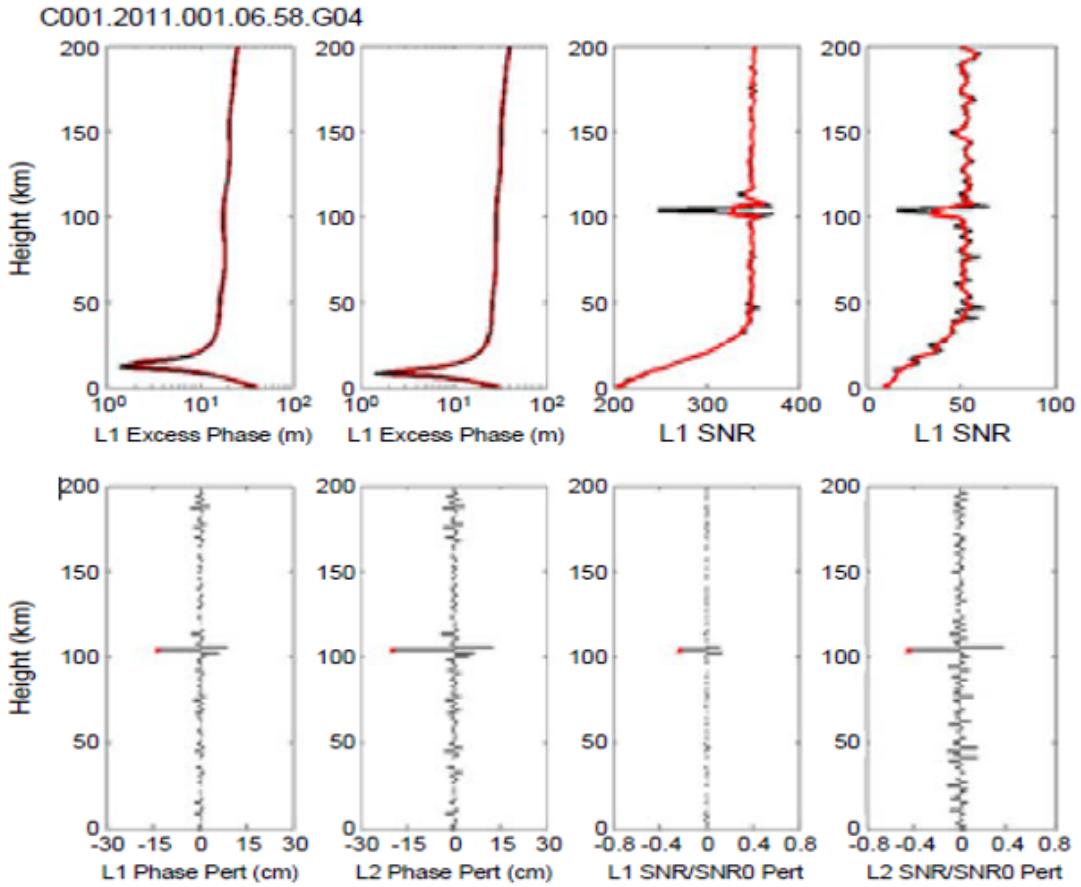

Figure 9. Processed data from a sample COSMIC occultation. Black profiles are raw data, and the red profiles are smoothed Chu et al. (2014).

2.3.2 Yu S_4 Technique.

Yu et al. (2019) analyzed foEs occurrence rates from ground based ionosondes vs $S_{4,max}$ calculated from COSMIC GPS-RO. The technique takes in the COSMIC 50 Hz atmospheric phase (atmPhs) data set, and runs a 50 point rolling average to

calculate a representative S4 max. Yu et al. (2019) then applied a best fit formula to the data set, which was calculated as

$$(foEs - 1.2)^2 = 13.62 \times S_{4,max} \tag{9}$$

shown as the violet line in Figure 10. Carmona (2021) used the same formula to calculate fbEs by applying a binary foEs cutoff at 4.2 MHz using the formula $(foEs - 1.2) = 3$ since foEs is greater than fbEs. As long as $S_{4,max}$ can be calculated, the technique is simple, which is the advantage in the Yu S_4 technique over the Chu phase perturbation technique. However, the lack of multiple criteria does open the door for more potential error.

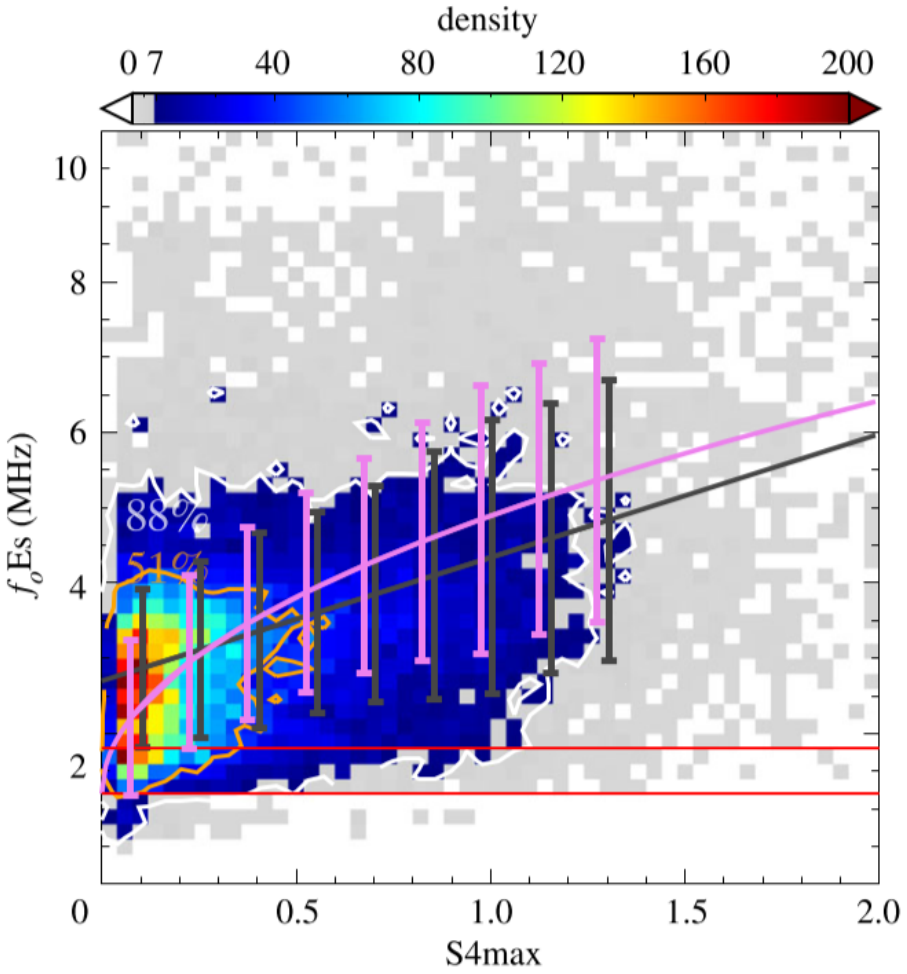

Figure 10. Density scatter plot from Yu et al. (2019) with best fit equation (Equation 9) depicted by the purple line. foEs values generated from COSMIC data from 2006-2014.

2.4 Summary of Geomagnetic Storming and Solar Activity Indices

Of the many indices available to measure geomagnetic storming and solar activity, this study will focus on five in particular. Four of the indices focus on geomagnetic activity: Kp, AE, DST, and Bz. The last indice, R, is the relative sunspot number and focuses on solar activity. A summary of each index is given below.

2.4.1 Kp Index.

The Kp index was introduced by Bartels et al. (1939) and is the primary index reported by NOAA's Space Weather Prediction Center (SWPC) for classifying geomagnetic storms. It is a 3 hour average of the K index, which is a quasi-logarithmic planetary average of H, D, and Z component ranges from Earth's magnetic field (Rostoker, 1972). The K index is measured at 13 stations around the globe between 44^o-60^o geomagnetic latitude (SWPC, 2021). Table 2 shows the specific NOAA geomagnetic storm conditions for the range of Kp values. NOAA classifies all Kp values below 5 as quiet. The strength of the Kp is in giving a general overview of the global geomagnetic conditions. However, the generality of the Kp index and low time resolution mean the Kp index is poor at picking up smaller resolution spatial and temporal perturbations. Kp has been loosely linked to Es formation in previous studies. Batista and Abdu (1977); Saksena (1974); Voiculescu et al. (2000); Zaalov and Moskaleva (2019); Zuo and Wan (2008) found no correlation or a slightly negative correlation between Kp and Es rates, especially in the low and mid latitudes.

NOAA Space Weather Scales

Category		Effect	Physical measure	Average Frequency (1 cycle = 11 years)
Scale	Descriptor	Duration of event will influence severity of effects		
Geomagnetic Storms			Kp values* determined every 3 hours	Number of storm events when Kp level was met; (number of storm days)
G 5	Extreme	Power systems: widespread voltage control problems and protective system problems can occur, some grid systems may experience complete collapse or blackouts. Transformers may experience damage. Spacecraft operations: may experience extensive surface charging, problems with orientation, uplink/downlink and tracking satellites. Other systems: pipeline currents can reach hundreds of amps, HF (high frequency) radio propagation may be impossible in many areas for one to two days, satellite navigation may be degraded for days, low-frequency radio navigation can be out for hours, and aurora has been seen as low as Florida and southern Texas (typically 40° geomagnetic lat.).**	Kp=9	4 per cycle (4 days per cycle)
G 4	Severe	Power systems: possible widespread voltage control problems and some protective systems will mistakenly trip out key assets from the grid. Spacecraft operations: may experience surface charging and tracking problems, corrections may be needed for orientation problems. Other systems: induced pipeline currents affect preventive measures, HF radio propagation sporadic, satellite navigation degraded for hours, low-frequency radio navigation disrupted, and aurora has been seen as low as Alabama and northern California (typically 45° geomagnetic lat.).**	Kp=8	100 per cycle (60 days per cycle)
G 3	Strong	Power systems: voltage corrections may be required, false alarms triggered on some protection devices. Spacecraft operations: surface charging may occur on satellite components, drag may increase on low-Earth-orbit satellites, and corrections may be needed for orientation problems. Other systems: intermittent satellite navigation and low-frequency radio navigation problems may occur, HF radio may be intermittent, and aurora has been seen as low as Illinois and Oregon (typically 50° geomagnetic lat.).**	Kp=7	200 per cycle (130 days per cycle)
G 2	Moderate	Power systems: high-latitude power systems may experience voltage alarms, long-duration storms may cause transformer damage. Spacecraft operations: corrective actions to orientation may be required by ground control; possible changes in drag affect orbit predictions. Other systems: HF radio propagation can fade at higher latitudes, and aurora has been seen as low as New York and Idaho (typically 55° geomagnetic lat.).**	Kp=6	600 per cycle (360 days per cycle)
G 1	Minor	Power systems: weak power grid fluctuations can occur. Spacecraft operations: minor impact on satellite operations possible. Other systems: migratory animals are affected at this and higher levels; aurora is commonly visible at high latitudes (northern Michigan and Maine).**	Kp=5	1700 per cycle (900 days per cycle)

* Based on this measure, but other physical measures are also considered.
** For specific locations around the globe, use geomagnetic latitude to determine likely sightings (see www.swpc.noaa.gov/Aurora)

Table 2. Geomagnetic storm categories for given values of Kp from minor to extreme. It is implied that anything below Kp=5 is quiet geomagnetic storming conditions (SWPC, 2021).

2.4.2 AE Index.

The Auroral Electrojet (AE) index was introduced by Davis and Sugiura (1966) as an auroral alternative to the Kp, and a quantitative measure of the auroral electrojet activity. While the K index has a few stations located in the subauroral region, the AE is measured by 12 stations exclusively stationed in the northern hemisphere between 60^o-72^o geomagnetic latitude (Kyoto, 2022). Each station measures the upper (AU) and lower (AL) magnitudes of the H geomagnetic field component. The AE index is simply (AU-AL). The AE index is measured every 2.5 mins, but is reported hourly as

an 1-hour average in nano-Teslas (nT). Since the AE index is a direct measurement of a physical phenomena, it is easier to physically interpret and derive other physical quantities (Kamide and Akasofu, 1983). The biggest weakness of the AE index is the positioning of the observing stations during very strong storms that push the auroral oval equatorward, or weak conditions that contract the oval poleward. The stations are strategically placed in the average location of the auroral oval, but the dynamic nature of the geomagnetic conditions can compress or contract magnetic field, making it difficult for the stations to report accurate data (Kamide and Akasofu, 1983). Abdu et al. (2014, 2013); Moro et al. (2017) have shown a strong correlation between the AE index, as well as the IMF Bz (Section 2.4.4), and Es occurrence rates. Electric fields heavily contribute to auroral and equatorial Es formation, so when the electric fields are enhanced, it is presumed that Es rates would increase. When AE is high and Bz is strongly negative, the equatorial and auororal electric fields are enhanced.

2.4.3 DST Index.

The DST index (Disturbance Storm Time) is measured at 8 near-equatorial stations that are sufficiently above the equatorial electrojet. The Kp and AE indices directly measure the sub-auroral and auroral regions. Conversely, the DST is a measurement of the low latitude and equatorial conditions, giving a proxy for the ring current. Introduced by Sugiura (1963), the DST also measures the H component to the magnetic field and is reported hourly in nT. Large changes in the DST represent sharp perturbations of the solar wind, and is a good indicator of the onset of a geomagnetic storm (Jawad et al., 2019). A typical storm signature is characterized by an initial phase with values that are positive. Following the initiation phase is the main phase where the DST drop rapidly in value until the storm peak value is reached. The last phase is the recovery phase, when the DST value slowly returns to a baseline

value (Echer et al., 2011). The advantage of the DST is the high temporal resolution and the ability to track phases of the storm. However, outside of tracking the peak intensity, it is difficult to quantify the magnitude of storms during the main phase. DST is best when used as a relative index compared to track onset and recovery (Rostoker, 1972). DST has been used in previous studies to show a lower equatorial Es rate and strength during active days (Rastogi, 1972).

2.4.4 IMF Bz.

Bz is the north-south component of the Interplanetary Magnetic Field (IMF). A strong southward oriented IMF (negative Bz) has been shown to interact with the northward oriented geomagnetic field and cause magnetic reconnection, potentially resulting in the amplification of Earth's electric fields at all latitudes (Wei et al., 2008). The electric field amplification has been linked to increased rates of auroral Es by Nygrén et al. (2006), even with large positive Bz values. Therefore, the strength and orientation of Bz plays an important role in auroral Es, and Resende et al. (2016) showed the vertical component of the electric field was more important to Es development at the equator than the neutral winds and wind shear. Therefore, it is important to take into account the Bz for Es development.

2.4.5 Relative Sunspot Number (R).

The relative sunspot number, R, was introduced in 1851 by Rudolf Wolf, and has been the standard for reporting sunspot numbers since (Clette et al., 2014). The R sunspot number is calculated by

$$R = k \cdot (10 \cdot N_G + N_S) \tag{10}$$

where N_G is the number of sunspot groups, N_G is the total number of individual sunspots, and k is scaling coefficient to take into account differences between observers and observatories. When Wolf introduced the number, his observer k was 1, so he set the scale baseline. Therefore, it is important to note that the R number is a relative number (no units), not an absolute number (Clette et al., 2014). Figure 11 shows the R numbers over the previous five solar cycles, and a predicted R number for the upcoming solar cycle, predicted by NOAA and International Space Environmental Services (ISES). A few studies have looked at the effects of sunspot number and solar cycle on the effect of Es rates, and the results have not been very conclusive. Reddy and Matsushita (1968) and Baggaley (1985) found a positive correlation between solar cycle and Es rate. Baggaley (1984) found no relationship between solar cycle and Es. Zhang et al. (2015) and Maksyutin and Sherstyukov (2005) found a mostly negative but somewhat complex relationship, in that it depends on the strength of Es layers being evaluated.

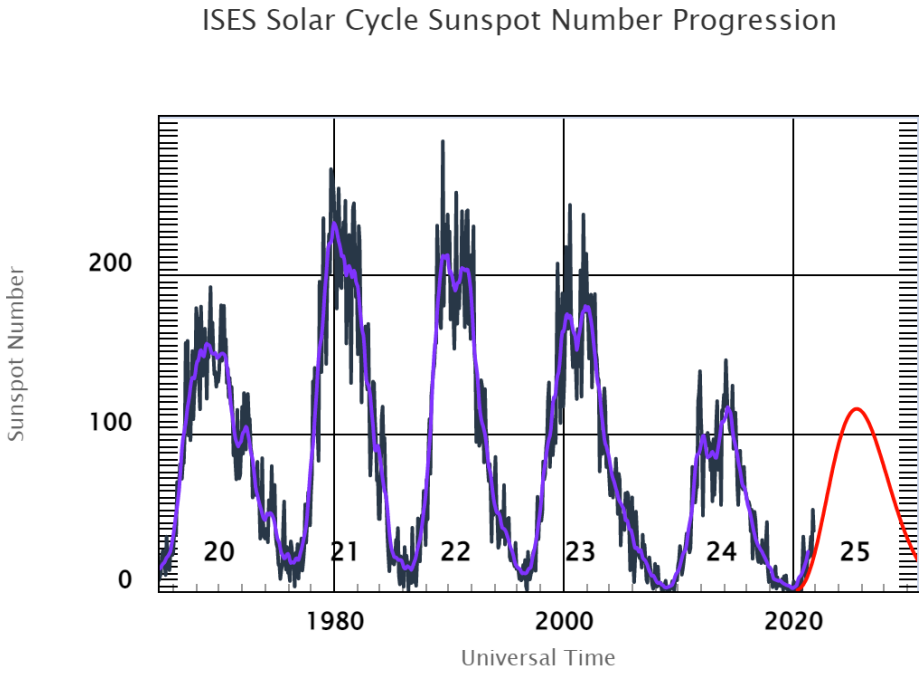

Figure 11. R sunspot values over the previous five solar cycles (ISES, 2021).

III. Methodology and Results

The purpose of this chapter is to provide the methodology, results, and analysis for the globally derived fbEs rates from GPS-RO and Digisonde data for the 13 year period from 2006-2019. The data will be separated annually, seasonally, and monthly to examine geographic latitude and longitude dependence, magnetic dip angle positional dependence, and diurnal morphology. The results are presented for sporadic-E with an fbEs cutoff of 3 MHz, and Es with no fbEs cutoff (any measurable fbEs).

3.1 Data Set Processing

3.1.1 COSMIC Data Set.

As mentioned in Section 2.3, the COSMIC constellation offers a great opportunity to study phenomena on a global scale, without the spatial restrictions associated with ionosondes (Schreiner et al., 2014). In line with the Carmona (2021) analysis, the Chu et al. (2014) phase-perturbation and Yu et al. (2019) S4 techniques are used. The Chu technique predicts fbEs with a 3 MHz cutoff, and requires the 1-Hz COSMIC ionospheric phase (ionPhs) files. From 2006-2019, there are 3,991,696 ionPhs observations, which have a vertical resolution of approximately 2km, and ranges from around 60km altitude up to orbit altitude (Kepkar et al., 2020). The Yu technique predicts the presence of any fbEs, and requires the 50-Hz COSMIC atmospheric phase (atmPhs) files. From 2006-2019, there are 5,081,226 atmPhs observations, and these files have up to a 40m resolution over the same altitude range. Figure 12 shows the observation density binned in 5^o latitude x 5^o longitude intervals, with 50 Hz atmPhs observations on top, and 1 Hz ionPhs observations on the bottom. At finer grid resolution (i.e. 1^ox1^o or 2^ox2^o), the data set is too sparse to complete compelling analysis.

Both observation density plots share the same patterns. The highest concentration of observations are between 15^o and 60^o latitude, and there are considerably less in the equatorial and polar regions. Due to the COSMIC orbit inclination of 72^o, the orbit path traverses a smaller fraction of the equatorial region. In the polar regions the convergence of latitude lines results in smaller land areas per 5^o bin. Figure 13 shows the Es observation density, with each positive occurrence of fbEs recorded as 1 observation. The all-fbEs set is on top, the bottom is fbEs $\geq$ 3 MHz, and the overlay lines are the geomagnetic latitude. The fuchsia line in the middle follows the geomagnetic equator, and the subsequent white contours are the geomagnetic latitude every 20^o up to 80^o N and S.

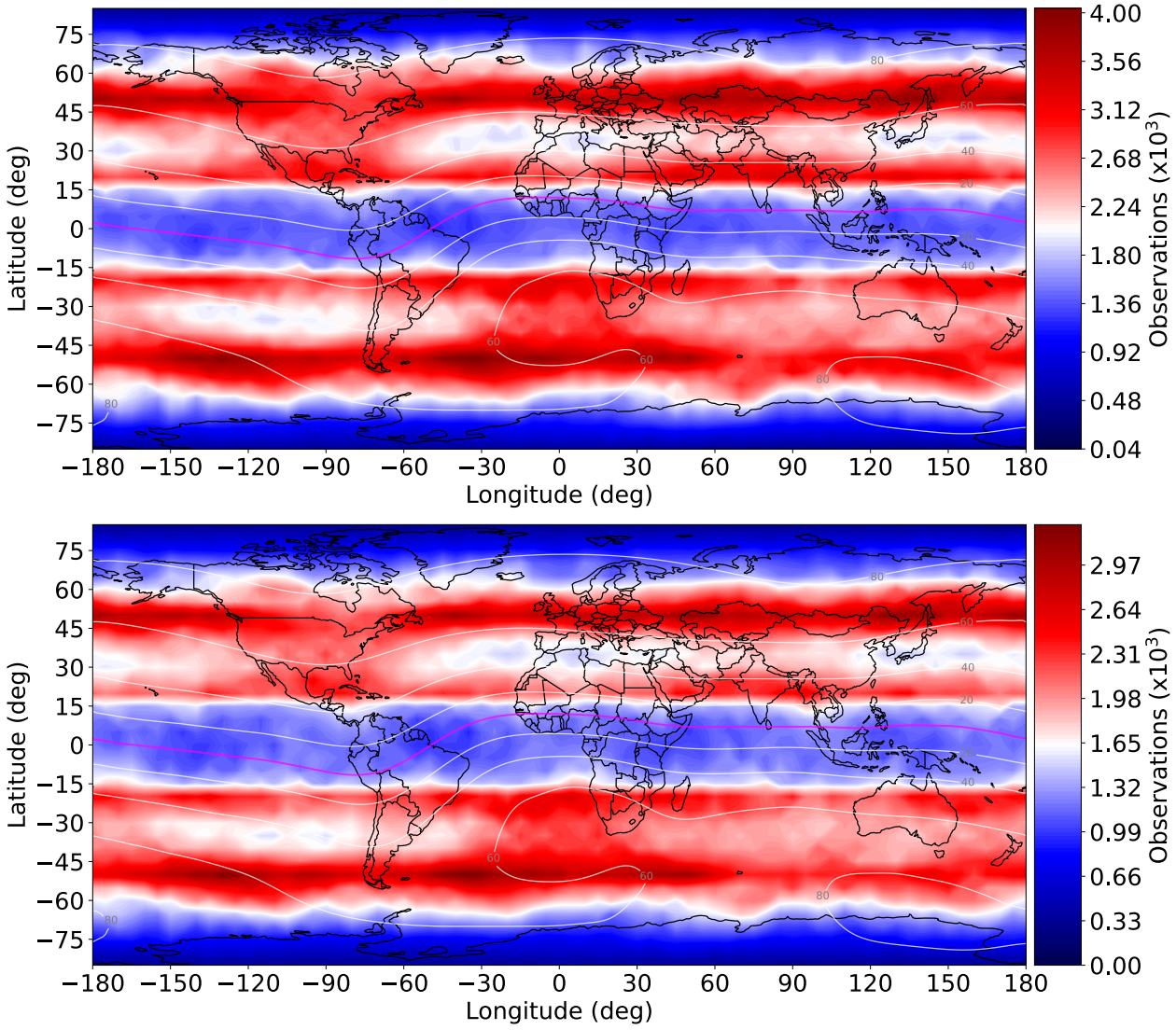

Figure 12. Global GPS-RO observation density in 5^o latitude by 5^o longitude bins, from 2006 to 2019. The top map is comprised of the 50 Hz atmPhs data set that will be used in the all-fbEs analysis. The bottom map is comprised of the 1 Hz ionPhs data set that will be used in the fbEs $\geq$ 3 MHz analysis. There is natural banding in the density due to the nature of the COSMIC constellation orbit geometry. Noticeably, the observation density along the equatorial region and high latitudes are the lowest sampled regions, and will offer the most uncertainty.

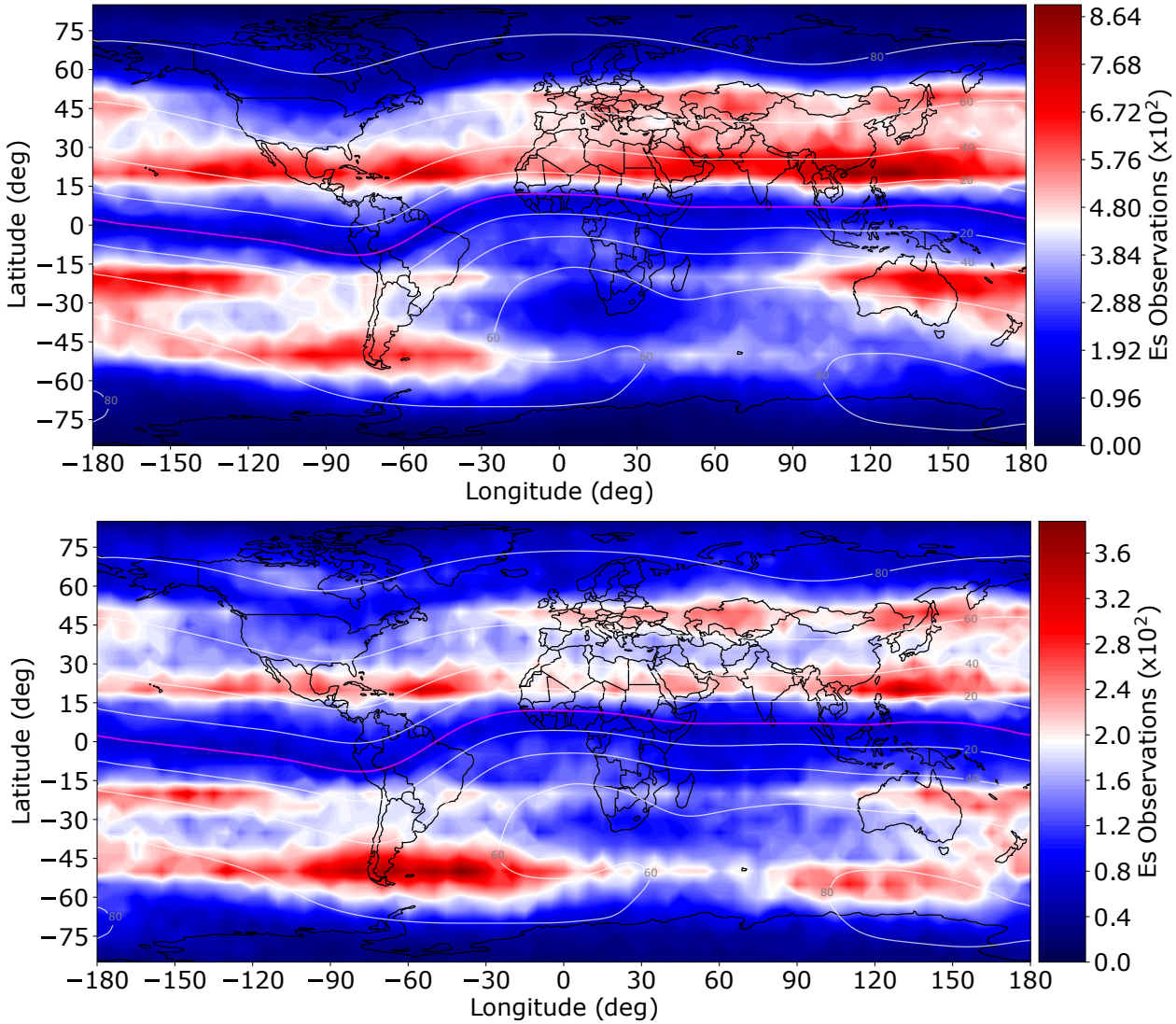

Figure 13. Global GPS-RO Es observation density. The top map is all-fbEs, and the bottom map is fbEs $\geq$ 3 MHz. Similar to the standard observation density map (Figure 12), the mid-latitudes offer the highest density of observations. It is difficult to decipher Es hot spots without considering the total observations as well.

For reference, the Digisonde's total observation density is shown in Figure 14. In some places, like Europe, there are many Digisonde reporting sites to create a reliable analysis. Over Europe, the sites are so tightly spaced that there are multiple sites within the same 5^ox5^o grid boxes. However, outside of places like Europe, the spatial limitations inherent in ionosonde measurements is quite apparent in Figure 14. Since Digisondes are landlocked, we are unable to use them to observe the oceans.

Furthermore, they require considerable maintenance and a dedicated facility/plot of land. For this reason, there are large regions over land (Africa, Central Asia, etc.) where we get little to no ionosonde soundings. Therefore, it would be difficult to use only Digisonde observations to complete a global climatology. Utilizing GPS-RO, we can obtain a much better understanding of the spatial distribution of Es without gaps.

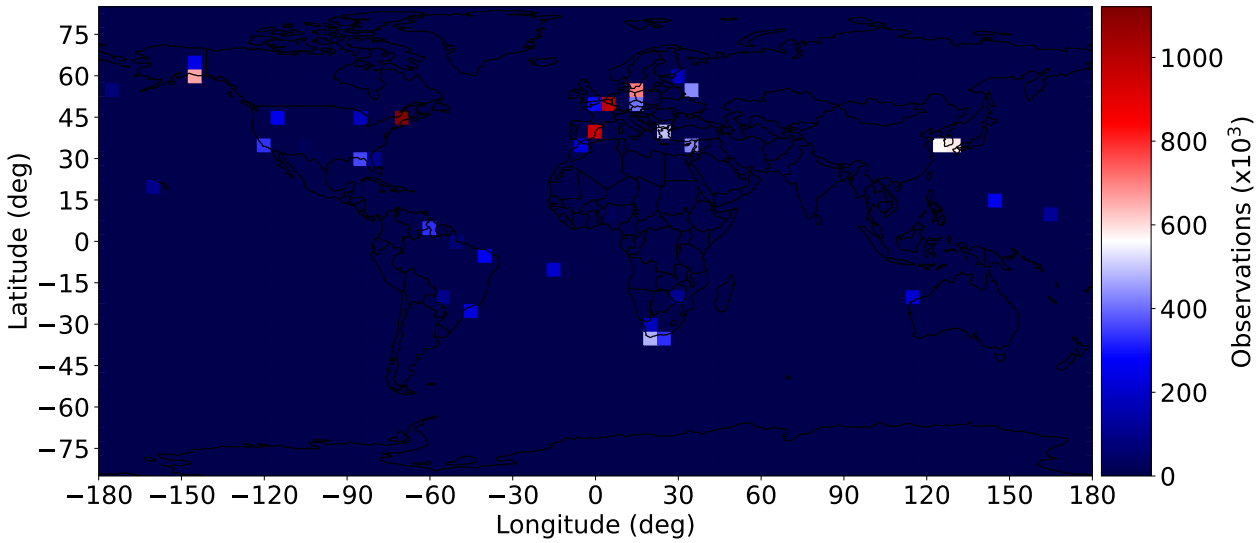

Figure 14. The global distribution of Digisonde observations within 5^o longitude by 5^o latitude bins. Some Digisonde sites fall within the same bin as other Digisonde sites, but this is the same binning technique and location of bins as will be used throughout this document.

Figure 15 shows the global annual fbEs occurrence rates for all-fbEs (top) and 3 MHz fbEs cutoff (bottom) observations, with no regard to geomagnetic conditions. For all subsequent figures, the all-fbEs maps will be the top or left map, and the 3 MHz fbEs cutoff will be the lower or right chart. In Figure 15 each chart includes both the GPS-RO data and Digisonde data, still in a 5^{o}x5^o resolution. The number of Digisonde observations within each 5^{o}x5^o bin, where Digisondes are present, far outnumbers the GPS-RO observations. Therefore, the data is heavily skewed to the Digisonde. If the occurrence rates in each data set do not match, it should show up

in Figure 15 as a discontinuity from the surrounding points. Comparing the locations of the Digisonde sites in Figure 14 to Figure 15, the fbEs rates line up very well, presenting no sharp discontinuities or obvious gaps in data. For the top all-fbEs plot, there is one location over South Korea which has a rate approximately 5-7% below the surrounding regions. However, this is only one site between both figures, and the difference is not too large. Thus, this is a good proof of concept to supplement the data presented by Carmona (2021). For this reason, there is high confidence in solely using the respective GPS-RO analysis techniques, and omitting the Digisonde data in later sections due to lack of time fidelity in the Digisonde data set used. This allows us to sort observations based on various geomagnetic conditions.

3.1.2 Quiet Geomagnetic Conditions.

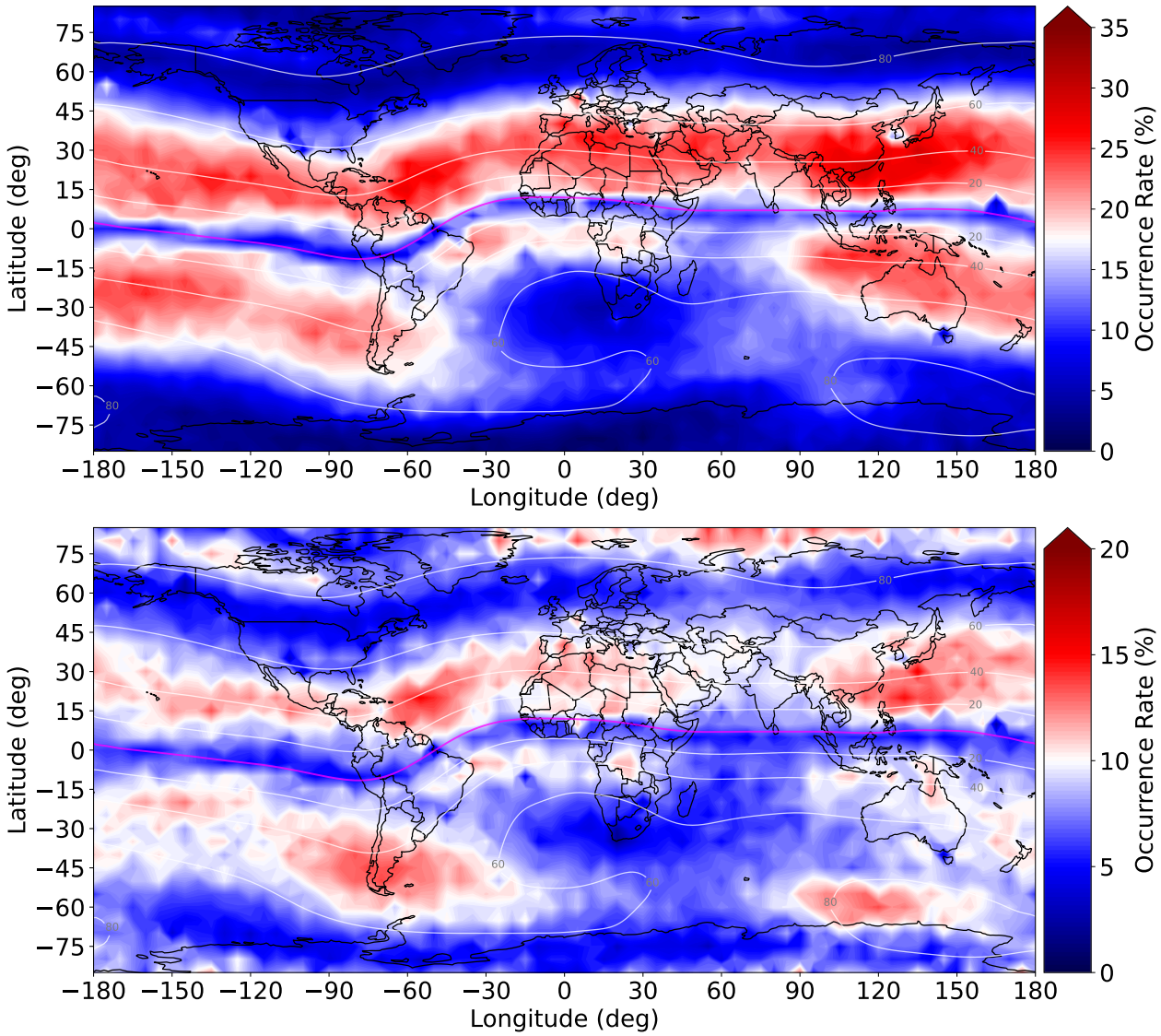

Figure 15. Annual global GPS-RO and Digisonde derived Es occurrence rates, with all-fbEs on top, and fbEs $\geq$ 3 MHz on bottom. GPS-RO and Digisonde observations are combined without any weighting to either data set. Even though the Digisonde sites do not span the entire globe (Figure 14), there are no discontinuities around Digisonde bins because the occurrence rates in the two data sets match.

In order to establish a baseline for a global climatology, it is important that the analysis have consistent background conditions. Therefore, all remaining figures in this chapter will present observations taken during geomagnetic quiet conditions with

respect to the Kp and AE indices, unless otherwise noted. For the Kp index, in line with SWPC (2021), quiet was defined as any Kp ≤ 4. Likewise, AE < 200 nT was considered quiet in agreement with Kamide and Akasofu (1983). Any observations taken at a time considered active by either the Kp or AE index, as recorded in the OMNIWeb database(Mathews and Towheed, 1995), were not used.

3.1.3 Error Analysis.

Error analysis was computed for each figure in this chapter and Chapter IV results. The respective error charts are shown in the appendix if not included on the chart itself. However, for all of the analysis, a minimum observation threshold was used to cap the error at 10%. Since Es occurrence rates are calculated by dividing the number of Es observations by total observations, each observation is a single binary event. The accumulation of single population binary events create a Bernoulli distribution (Binary distribution with a trial size of 1) with a standard deviation, σ of

$$\sigma = \sqrt{R_{Es}(1 - R_{Es})}, \tag{11}$$

where R_{Es} is the Es occurrence rate. The standard error for the distribution is

$$\sigma_s = \frac{\sigma}{\sqrt{n}}, \tag{12}$$

where n is the population size. For this research, n is the number of observations in a particular bin. The error is capped at 10% in the study by requiring n ≥ 25 for the entire study.

3.1.4 Geomagnetic Latitude.

Ionospheric phenomenon like Es are inherently intertwined with the Earth's magnetic field. Therefore, much of the study analyzes global climatology using both geographic latitude and geomagnetic latitude vs geographic longitude. For this study, the World Magnetic Model (WMM) magnetic field inclination is used as the magnetic latitude. The WMM is developed by NOAA, NGDC and CIRES and is updated every 5 years, or as needed (Maus et al., 2010). The inclination, otherwise known as dip angle, is the angle between the plane of the magnetic field and the surface of the Earth. Positive is pointing to the ground, and zero is parallel to the surface (Maus et al., 2010). Figure 16 shows the WMM 2010 Epoch map, with contours every 2^o. Since our data spans 2006 to 2019, we chose the averaged 2010 Epoch WMM main field inclination to make geomagnetic latitude contours for the maps. Inclination has some variation year to year, but the change is minor, and 2010 is a good in-between for our data set.

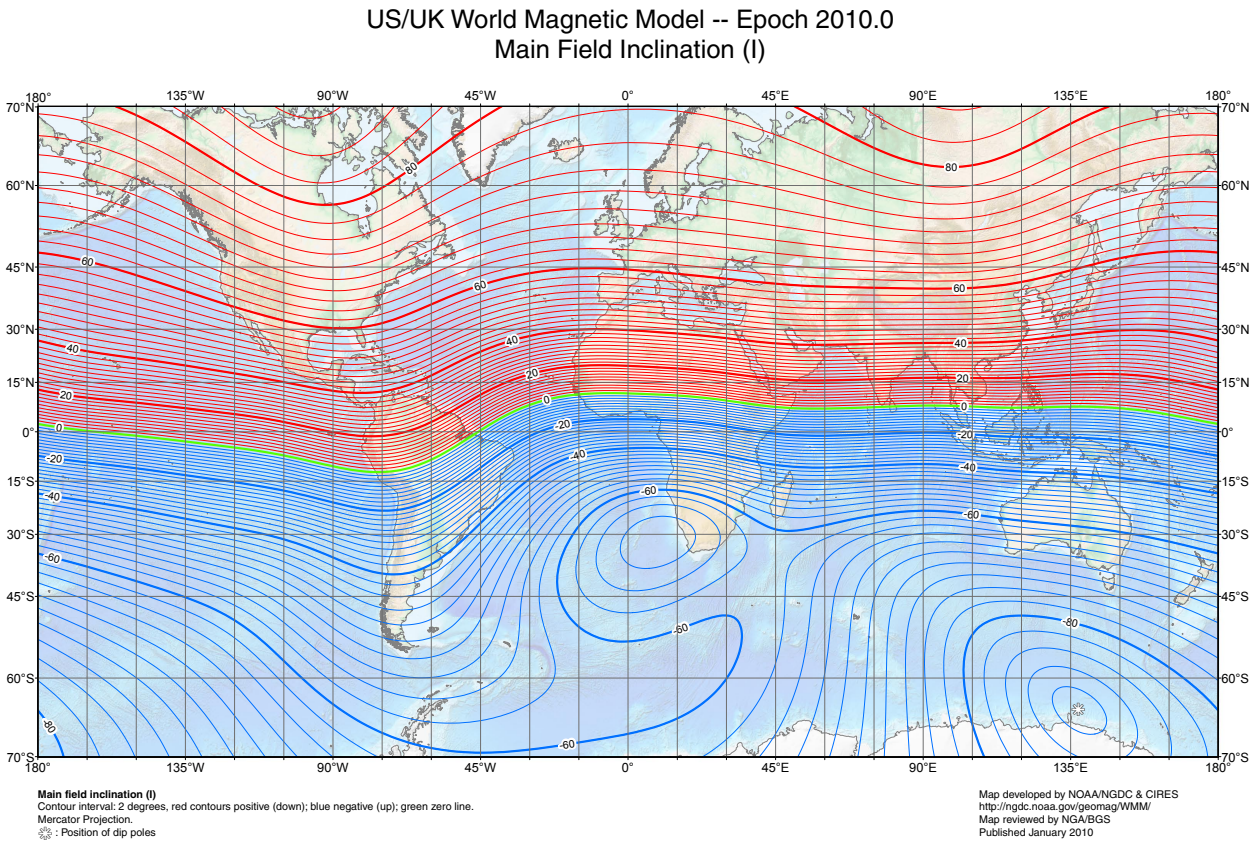

Figure 16. A map of the World Magnetic Model (WMM) main field inclination from the 2010 epoch, developed by NOAA, NGDC, and CIRES (Maus et al., 2010)

3.1.5 Solar Local Time and Boreal Seasons.

Solar local time is defined as the time when the sun is directly overhead at noon. This varies in many places from the local time since local time zones can be too broad/narrow and have non-uniform edges. Therefore, we adjusted all times in the study to solar local time, not local time, to remove oddities in various local time zone borders. Boreal seasons are simply defined as the northern hemisphere seasons. Thus, boreal summer is June, July, and August; boreal fall is September, October, and November; boreal winter is December, January, and February; and boreal spring is March, April, and May.

3.2 Global Annual Occurrence Rates

Figure 17 shows the geomagnetic quiet, annual occurrence rate for any measurable fbEs (top), and fbEs $\geq$ 3 MHz. The occurrence rates for the all-fbEs plot are roughly double the 3 MHz cutoff rates, on average. The highest occurrence rates are in the mid-latitudes, particularly between 10^o and 60^o inclination. Common among both maps is the lack of fbEs along the geomagnetic equator (fuchsia contour), and areas greater than 60^o inclination. The geomagnetic equator is defined by the 0^o inclination angle. At 0^o and inclinations above 60^o, the wind shear theory for creating Es breaks down, as described in Section 2.2. The South Atlantic Anomaly (SAA) is the area off the southwest coast of Africa with very low fbEs rates. By analysis of the contours, the SAA is positioned below the -60^o inclination contour, which is likely the driver behind the low rates due to the weak geomagnetic field strengths in the SAA. The one major deviation in the two maps is in the regions greater than 80^o geomagnetic latitude. In the northern hemisphere, this region is above the top most contour. Due to the abnormal geometry in the southern hemisphere, the 80^o contour is the small oval in the southeast corner centered at (-60^oS, 135^oE), and slightly crosses the 180^{th} meridian. Here, the all-fbEs technique does not pick up on any significant increases in occurrence rates. However, there is a significant amount of activity in the bottom 3 MHz map. This phenomena will be explored in detail in Chapter IV.

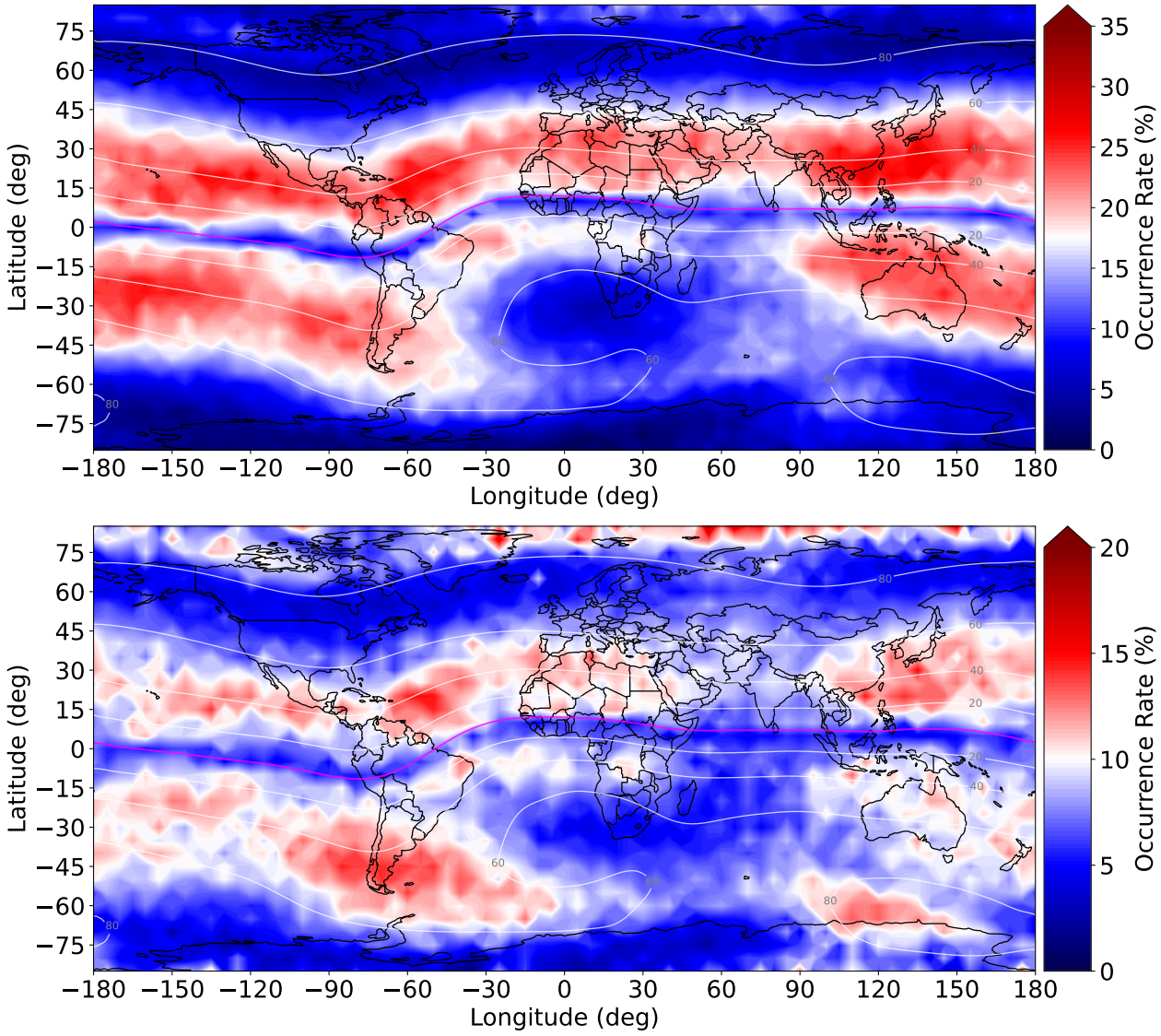

Figure 17. Annual Es occurrence rates derived from GPS-RO only, with all-fbEs on top, and fbEs $\geq$ 3 MHz on bottom. The Es is mostly contained to the mid latitudes, with low occurrence rates along the geomagnetic equator and in between 60^o-80^o inclination. In the fbEs $\geq$ 3 MHz map, the auroral region above 80^o inclination has increased ORs.

Figure 18 shows the global annual fbEs rates versus geomagnetic latitude instead of geographic latitude. Again, the all-fbEs rates (top) are roughly double the rates seen in the 3 MHz (bottom) map. In this presentation of the occurrence rates, one can clearly see the low occurrence rates along the magnetic equator. In addition, both techniques pick up on the strong mid-latitude (10^o-60^o) dependence of fbEs. This is

where the highest occurrence rates are found, and regions outside of the mid-latitudes rarely see any fbEs. For the all-fbEs map, rates outside of the mid-latitudes are nearly zero. While the rates are not completely zero in the 3 MHz cutoff map, the occurrence rates in the high latitude regions are at least half that of the mid-latitudes.

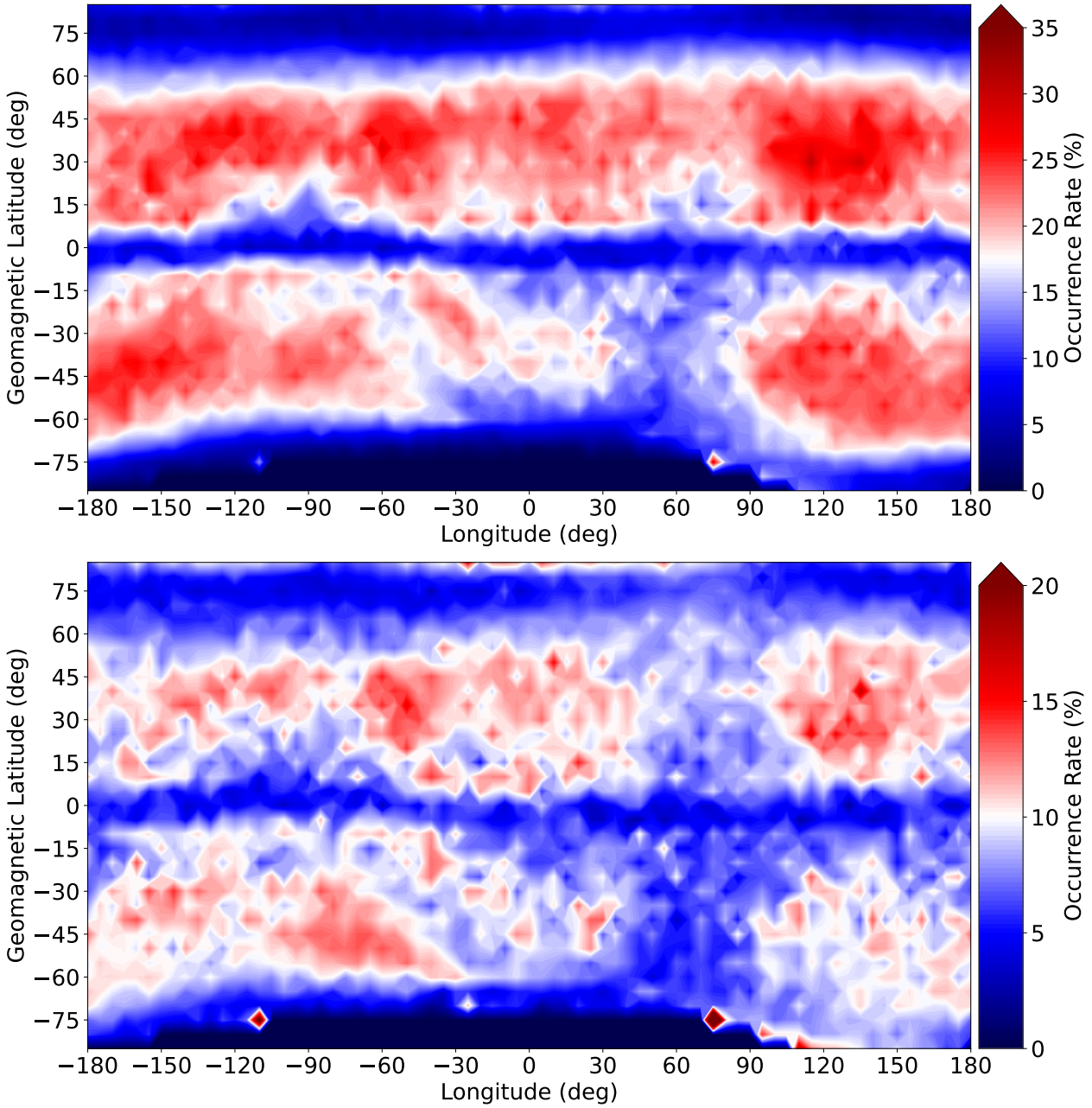

Figure 18. Annual Es occurrence rates derived from GPS-RO only for geomagnetic latitude vs geographic longitude, with all-fbEs on top, and fbEs $\geq$ 3 MHz on bottom. The low Es rate along the geomagnetic equator is still present, but after adjusting the coordinates to geomagnetic latitude, the void is straight along the equator instead of curving in Figure 15. The Es rate is still neatly contained between 10^o-60^o geomagnetic latitude except for some auroral activity in the fbEs $\geq$ 3 MHz map.

3.3 Seasonal and Monthly Occurrence Rates

Figure 19 shows the all-fbEs seasonal occurrence rates for each boreal season: winter (top left), spring (top right), summer (bottom left), and fall (bottom right). The annual occurrence rate (OR) figures (Figure 17, Figure 18) showed no general hemispheric preference, however, the seasonal analysis shows Es is much more prevalent in local summer. The wind patterns and wind shear mechanisms are largely unchanged from season to season. Instead it is likely the increased meteoric deposits during local summer lead to an increased Es rate, and a lower rate for areas in the opposite hemisphere (Haldoupis et al., 2007). Meteoric ablation is the long lived ion source, so without them, Es will be too short lived or too weak to be measured. In spring and fall, meteoric deposits occur mostly near the the geomagnetic equator. As was discussed in Section 2.2, the geomagnetic equator tends to inhibit the necessary wind shear conditions for the formation of Es. Lastly, during the summer period, there is a noticeable decrease in occurrence rates over North America. This is due to anomalous geographical dependence of vertical wind shear shown by Shinagawa et al. (2017) using data from the atmosphere-ionosphere coupled model GAIA (Ground-to-topside model of the Atmosphere and Ionosphere for Aeronomy). Shinagawa et al. (2017) showed that GAIA developed vertical ion convergence in the summer months was on the order of 1-2 cm^{-1} less over North American than other regions of similar latitude.

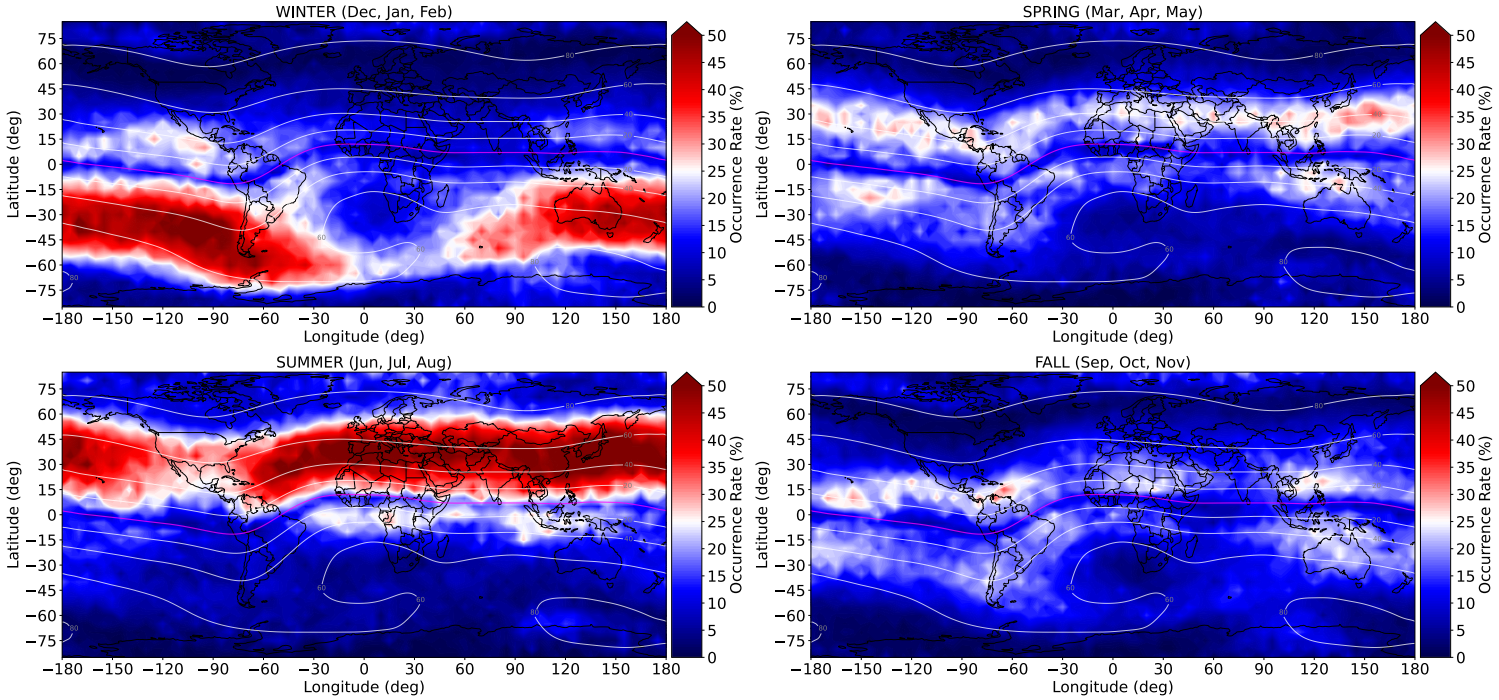

Figure 19. The all-fbEs occurrence rates for the four boreal seasons: winter(top left), spring (top right), summer (bottom left), and fall (bottom right). The winter and summer seasons have the highest Es occurrence rates, while the spring and fall are transitional seasons so they have much lower occurrence rates. Furthermore, the hemisphere in local summer has the highest Es occurrence rates.

The same seasonal breakout adjusted for geomagnetic latitude is shown in Figure 20. Again the spring and fall charts on the right are mostly quiet. The peak rates in the spring/fall are nearly half the peak rates in winter/summer. The spring and fall are during the equinox times so the large horizontal band of high Es occurrence rates that is present in the winter/summer maps would be over the equatorial region if not for the low inclination angle inhibiting Es development. When compared to the annual rates (Figure 18), there is more northern extent in the summer and southern extent in the winter, but the Es is still mostly contained to 10^o to 65^o geomagnetic latitude, with low ORs at the high latitudes.

During the boreal winter (Figure 20, top left), the SAA creates a large region void of Es from -50^o to 60^o longitude, even when adjusted for geomagnetic latitude because the SAA simply covers such a large land area. During the boreal summer

(Figure 20, bottom left), the low Es OR region over North America is still present. Again, this is due to the geographic distribution of the vertical wind shear found by Shinagawa et al. (2017).

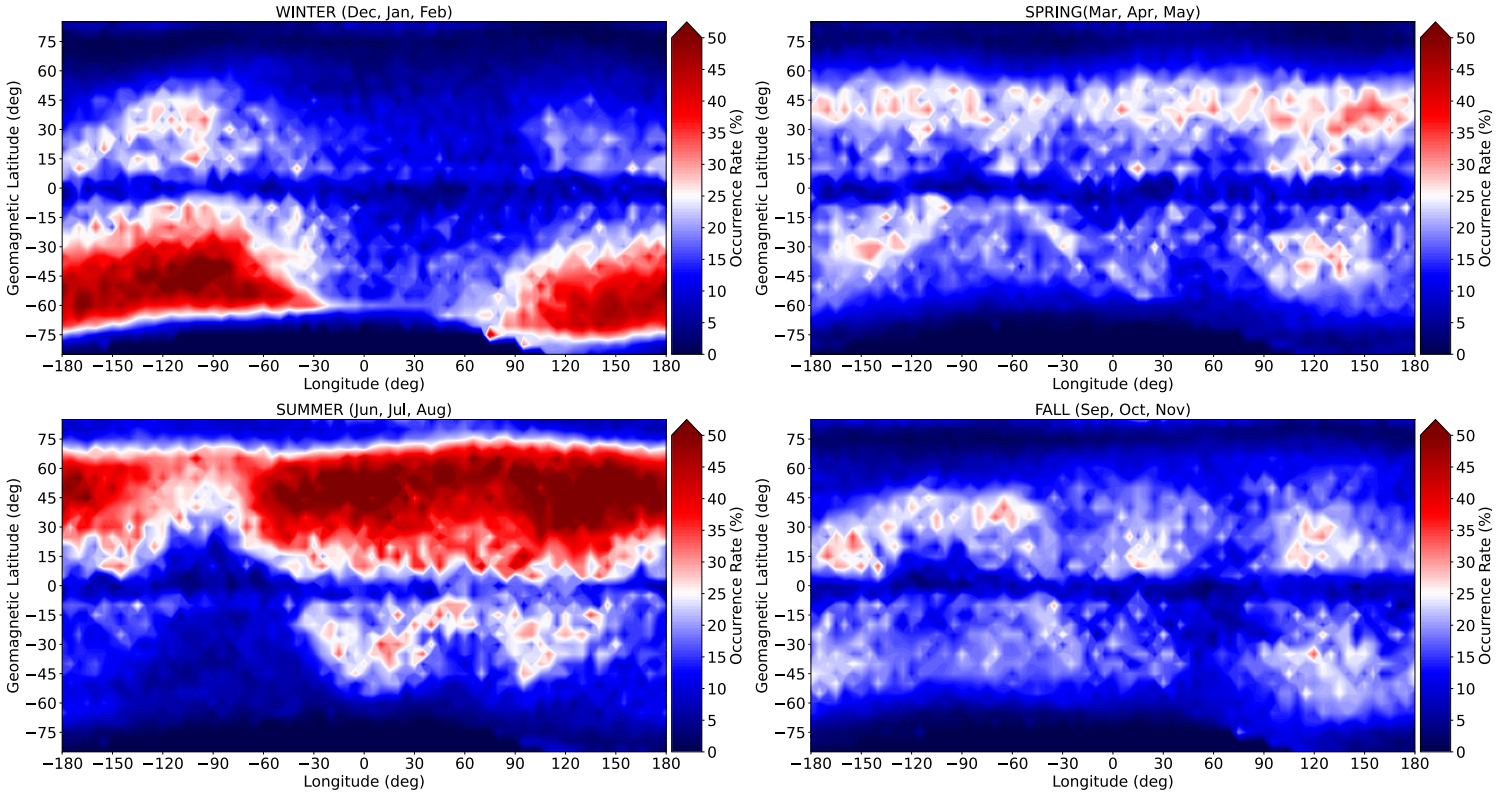

Figure 20. The all-fbEs occurrence rates with geomagnetic latitude for the four boreal seasons: winter(top left), spring (top right), summer (bottom left), and fall (bottom right). Even when adjusting for geomagnetic coordinates, the SAA creates a hole in the enhanced OR band in the southern hemisphere from -30^o to 60^o longitude during the boreal winter.

Figure 21 (geographic) and Figure 22 (geomagnetic) are the seasonal fbEs $\geq$ 3 MHz occurrence rates, in the same format as the all-fbEs charts (Figure 19 and Figure 20). The major trends from Figure 19 and Figure 20 are still present in Figure 21 and Figure 22: quiet geomagnetic equator and high latitudes, low ORs within the SAA and over North America, quiet globally during the spring/fall. Where the $\geq$3 MHz data differs from the all-fbEs is in the auroral regions. The all-fbEs data does not show activity above 80^o inclination, whereas the $\geq$3 MHz data consistently shows

activity. Theories on this activity will be discussed in Chapter IV, but it is most likely due to a limitation of the S_4 metric when traveling through thick Es layers.

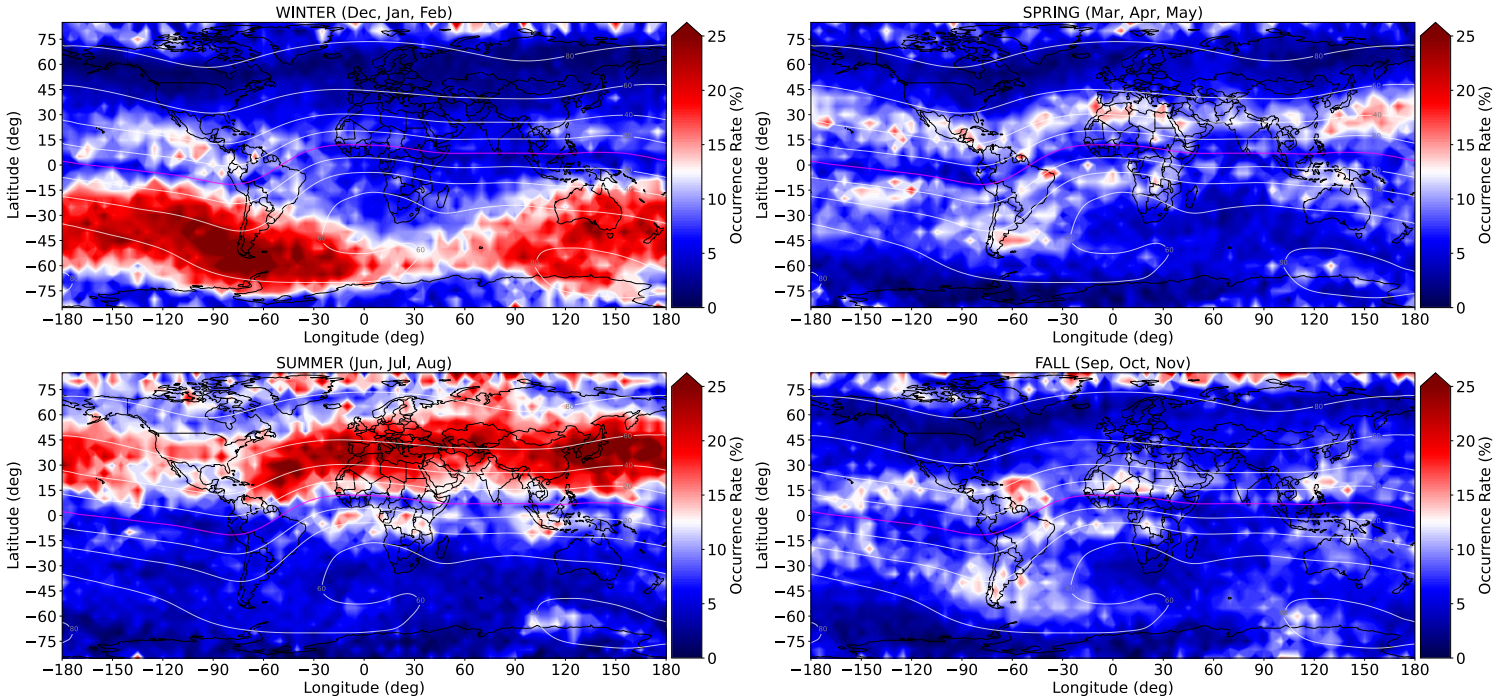

Figure 21. The all-fbEs occurrence rates for the four boreal seasons: winter(top left), spring (top right), summer (bottom left), and fall (bottom right). The winter/summer enhancement is still present, as well as the lack of Es over the SAA. In addition, the OR decrease over North America is easy to see in this data set.

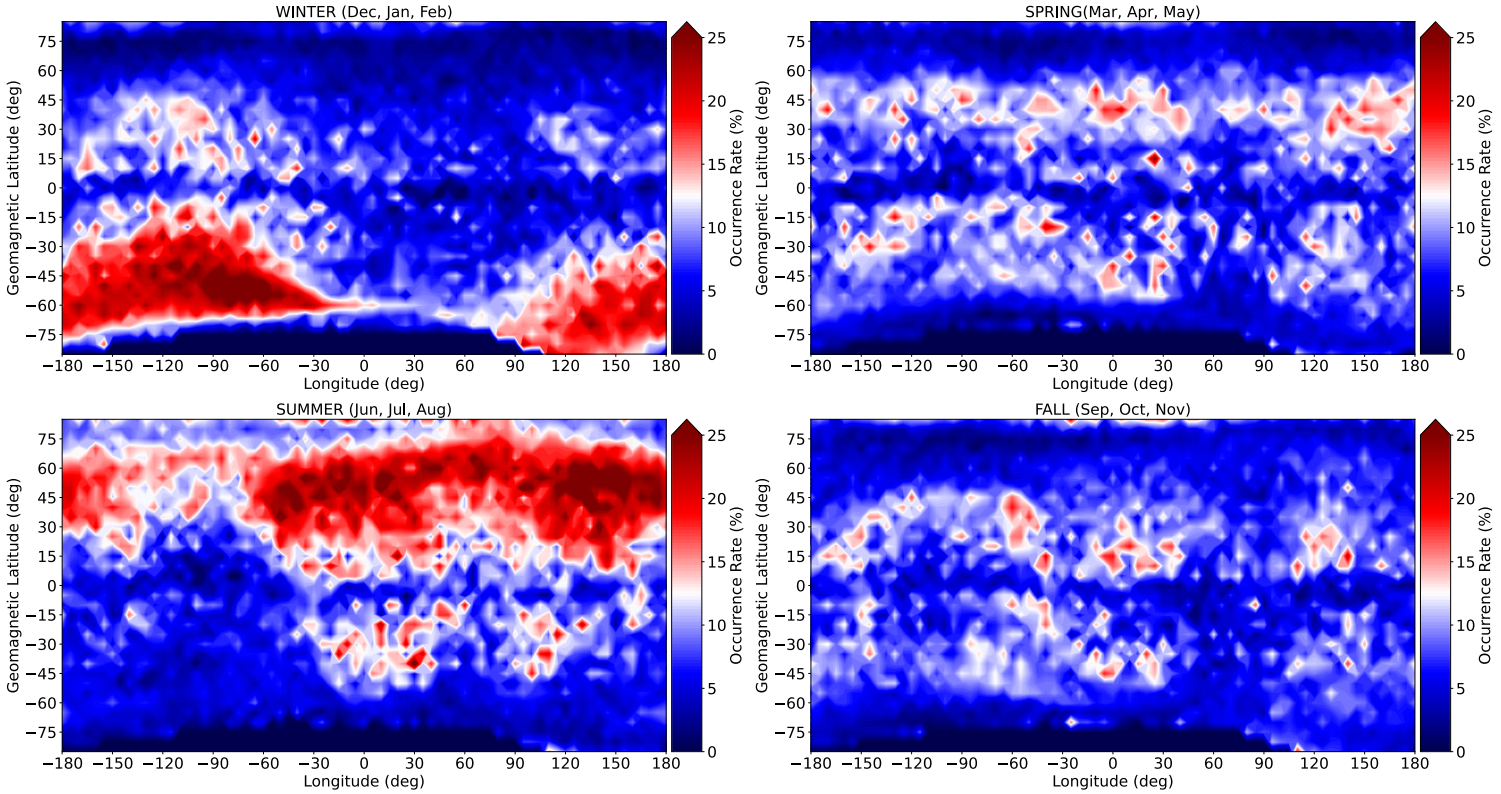

Figure 22. The fbEs $\geq$ 3 MHz occurrence rates for the four boreal seasons: winter(top left), spring (top right), summer (bottom left), and fall (bottom right). Similar to the three previous seasonal figures, there is an enhancement for the summer hemisphere, with the exception of the SAA and over North America.

Figure 23 and Figure 24 show the global monthly fbEs occurrence rates for geographic coordinates. Each row represents a boreal season, starting with winter in the top row (Dec, Jan, Feb), and progressing chronologically through the months/seasons in each successive row. Figure 23 shows the all-fbEs data, and Figure 24 shows the fbEs$\geq$ 3 MHz. The same trends in the seasonal analysis are present in the monthly breakdown. In the southern hemisphere, Es rates are much higher in the winter months from Dec-Feb, as well as in Nov. For the northern hemisphere, the summer months (Jun-Aug) again dominate, but rates are high in May as well. Mar, Apr, Sep, and Oct are transition months where the Es rates globally are much lower overall.

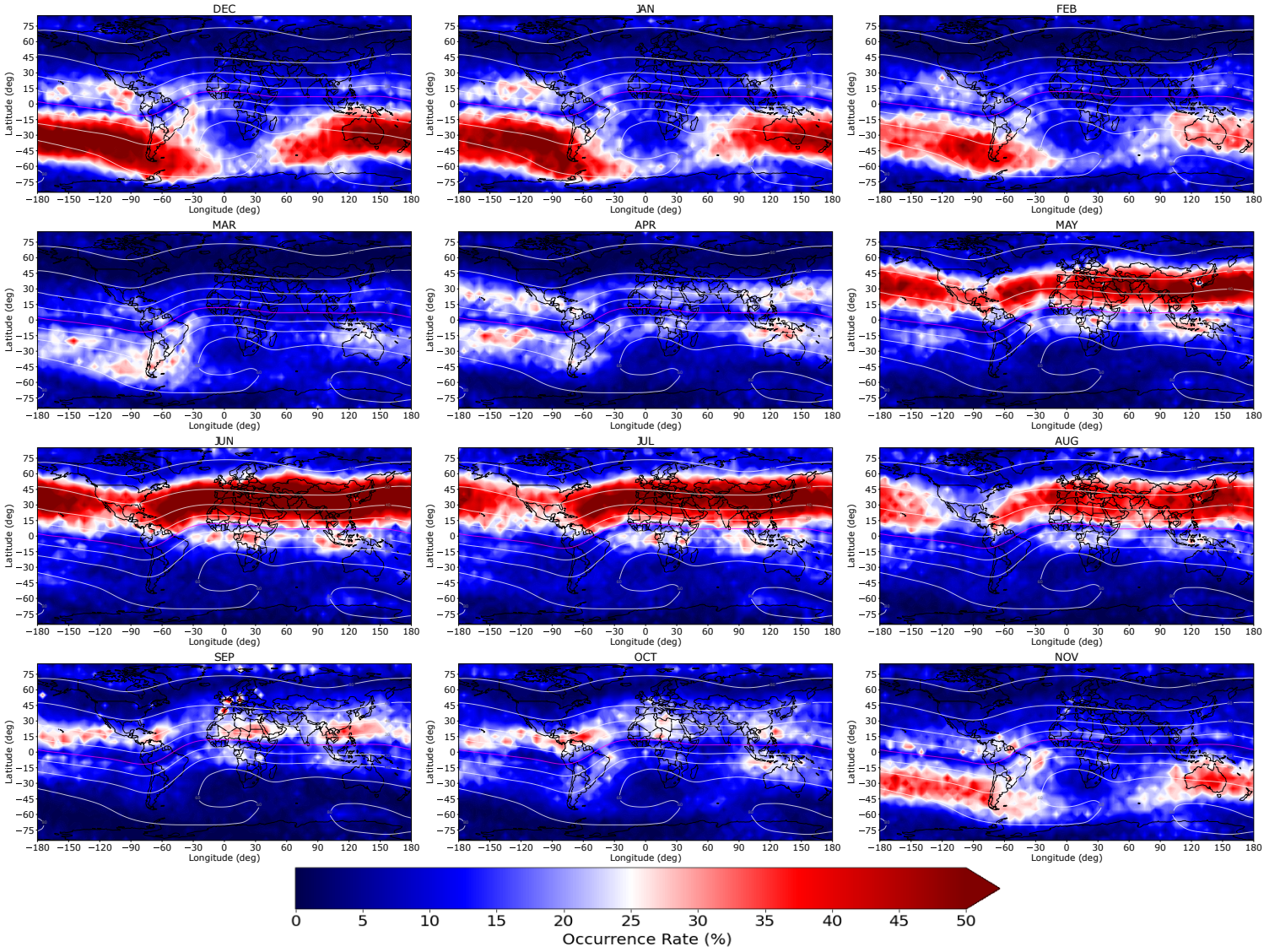

Figure 23. The all-fbEs occurrence rates for each month, organized in rows by season. May through August has the highest occurrence rates for the northern hemisphere, and November through February have the highest occurrence rates for the southern hemisphere. March, April, September, and October are transition months and thus have much lower occurrence rates on average.

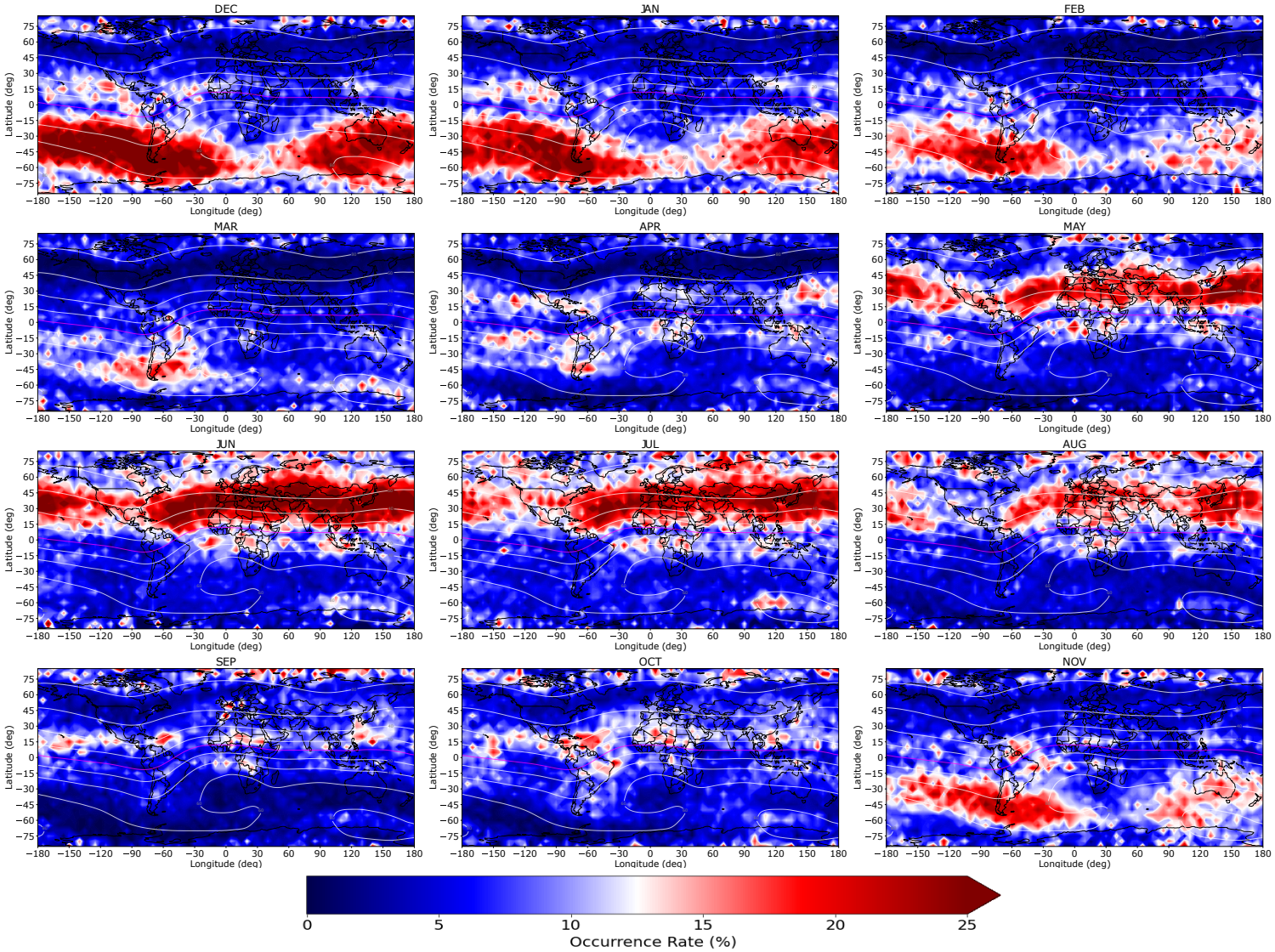

Figure 24. The fbEs $\geq$ 3 MHz occurrence rates for each month, organized in rows by season. Again the local summer months dominate in each region. The auroral regions in the local summer months are more active than the rest of the time.

Compared to previous GPS-RO climatological studies of Es ORs, this has some noticeable similarities and differences. This study has a clearly defined geomagnetic equator where there is rarely Es. Arras and Wickert (2018); Chu et al. (2014) showed a void around the geomagnetic equator, but to a much lesser degree than this study showed, for both all-fbEs and fbEs $\geq$ 3 MHz. Additionally, auroral Es is not reported by either previous study, or Yu et al. (2019), as is shown in the fbEs $\geq$ 3 MHz

data from this study. Previous studies were in good agreement with the diurnal and seasonal variations in Es ORs, as well as the mid latitude concentration of Es.

3.4 Diurnal Occurrence Rates

In addition to a geographic location dependence, Figure 25 shows the diurnal variation in fbEs occurrence rates. The geomagnetic latitude is plotted along the y-axis vs solar local time of day in an 24 hour (hhmm) format along the x-axis. The all-fbEs data is on the left, and the $\geq$ 3 MHz data is on the right. The obvious trend is high occurrence rates in the afternoon between 1500-2100 solar local (SL), with a peak around 1700SL. The early morning hours from 0100-0800 solar local are characterized by very low occurrence rates of less than 10% for all latitudes. Since Es is a strongly ionized layer within the E-region of the ionosphere, there needs to be sufficient solar radiation to ionize the neutral metallic meteor molecules. Peak solar radiation occurs in the early to late afternoon, which lines up with the start of the high ORs. Wind shear and slow ion recombination rates contribute to the long-lived nature of Es, so we don't see the Es ORs get depleted until the late evening hours, even though the sun has gone over the horizon is no longer ionizing the metallic molecules.

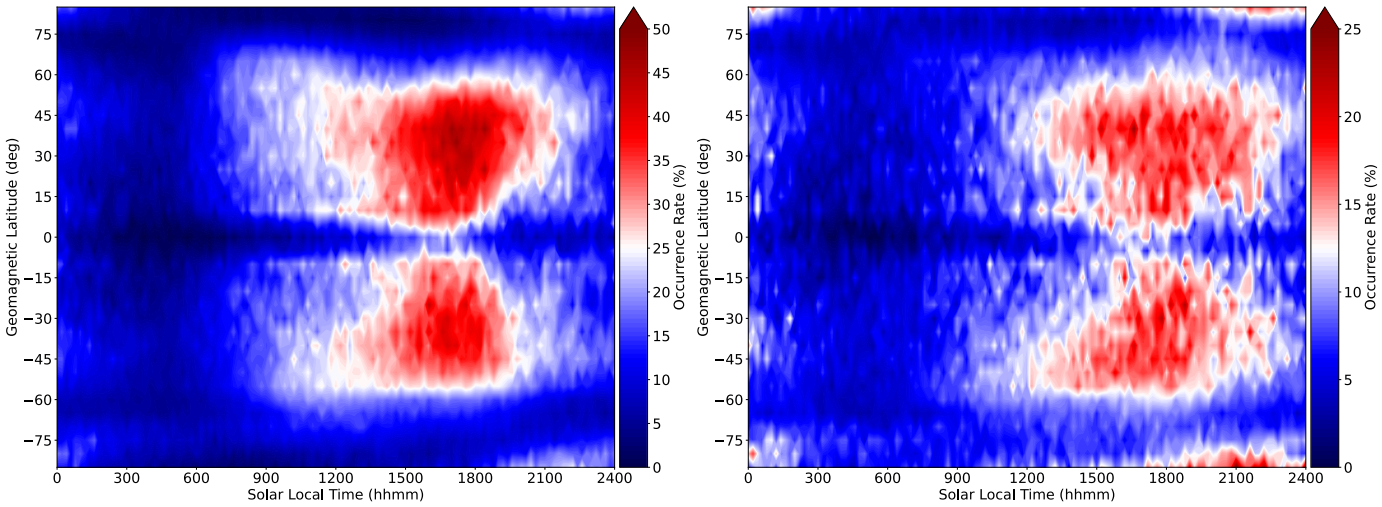

Figure 25. The annual occurrence rates for solar local time of day and geomagnetic latitude, with all-fbEs on the left and fbEs $\geq$ 3 MHz on the right. The pattern in both charts are very similar. The occurrence rates peak around 1700SL, but have a general spread from approximately 0900-2400SL. Of note, the $\geq$ 3 MHz rates continue slightly later than the all-fbEs rates, so stronger Es layers tend to last longer.

When looking at the four hour span from 1900-0100L in Figure 25, the all-fbEs (left) ORs fall off at a much quicker rate than the $\geq$ 3 MHz rates (right). It is likely that stronger Es layers persist for longer. The primary mechanism for Es dissipation is collisional recombination, which is a slow process for metallic ion chemistry (MacDougall et al., 2000). Since a strong layer has more ions, the recombination process for the entire layer will take longer. Another interesting trend on both charts is a "V" pattern in each hemisphere with a narrow Es window near the equator and a broadening in the OR in the pole-ward direction. This counter intuitive trend is likely due to seasonal spread in the mid latitudes during the summer (Figure 26, Figure 27).

Figure 26 and Figure 27 show the diurnal occurrence rates for each season. Figure 26 shows the seasonal trends for the all-fbEs data set, and Figure 27 is the fbEs $\geq$ 3 MHz set. In Figure 26, Es occurs nearly all day in the mid latitude local summer, with a short downtime from 0100 to 0500SL. For the remainder of the year in the respective hemispheres, the Es only occurs from approximately 1300 to 2100SL. This trend is amplified in Figure 27. For the hemisphere in local summer, high Es ORs are

present for nearly the entire day in the mid latitudes, as well as the high latitudes. For the remainder of the year, the enhanced ORs are contained to 1200 to 2300SL. The trend indicates that stronger Es layers formed in the local summer likely do not dissipate over the night, and are just re-enhanced every day when the sun comes up. In the auroral regions, there is a peak in the late evening and early morning time frame, which is in agreement with Whitehead (1970).

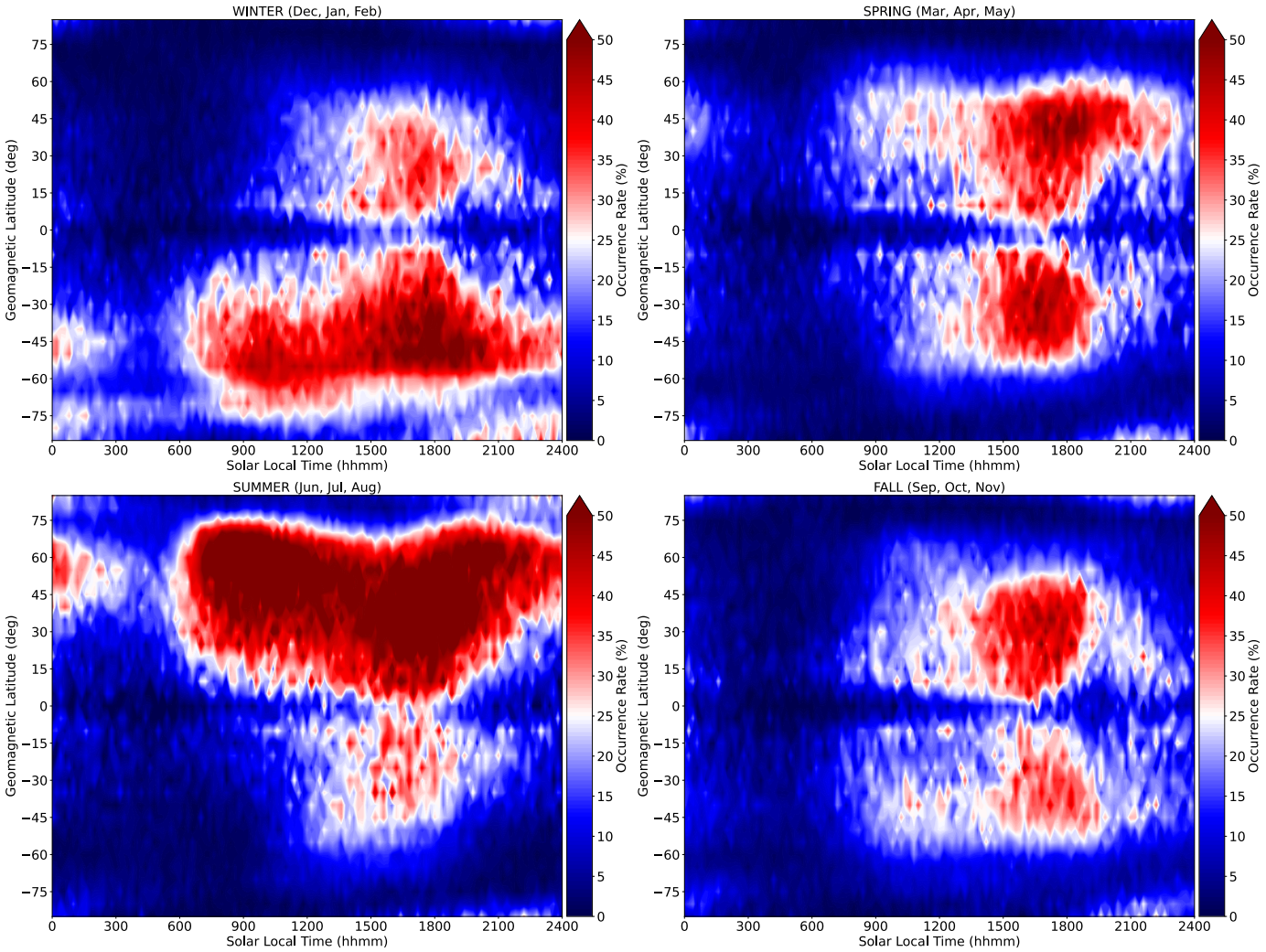

Figure 26. The all-fbEs seasonal occurrence rates for solar local time of day and geomagnetic latitude.

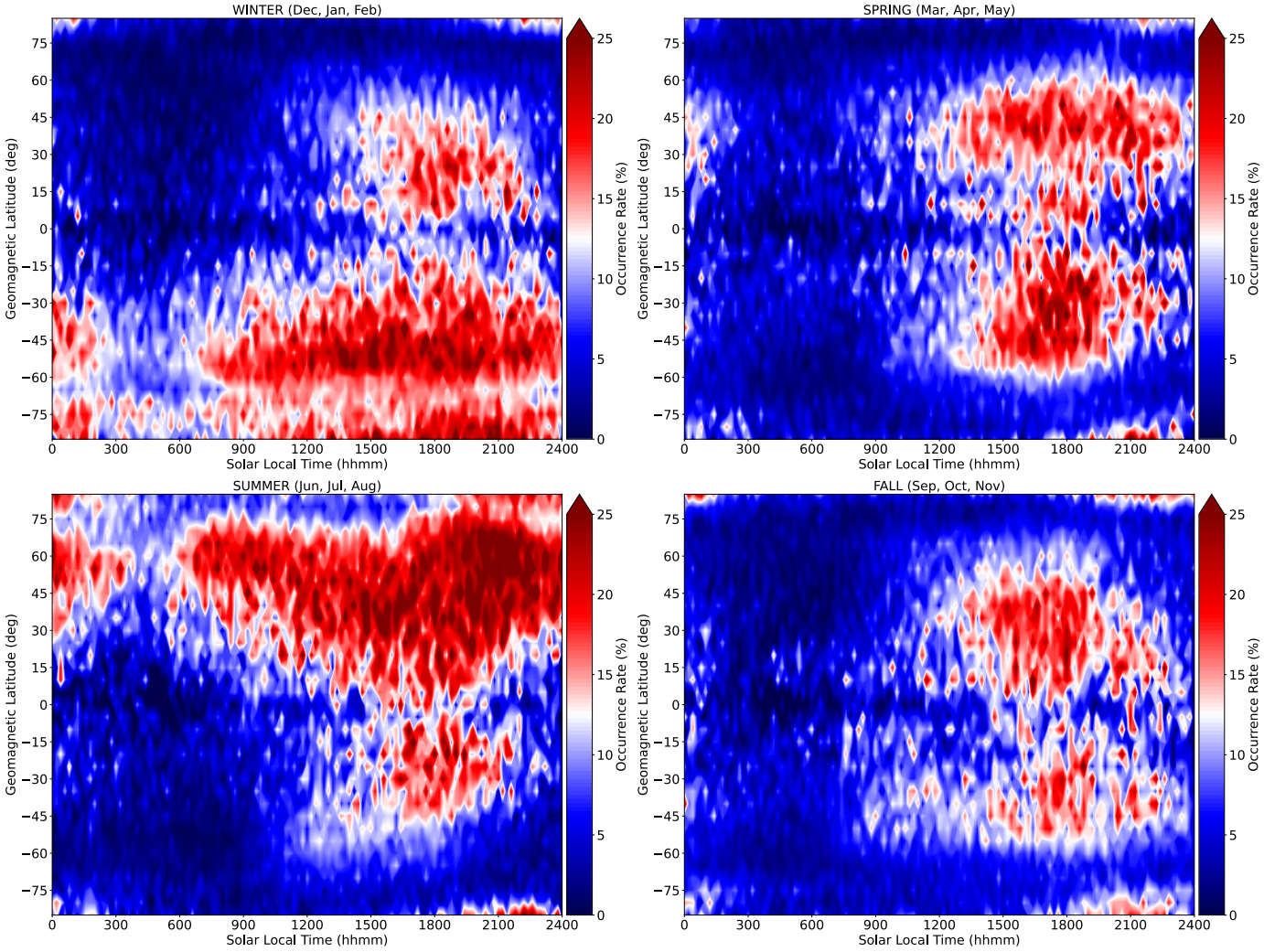

Figure 27. The fbEs $\geq$ 3 MHz seasonal occurrence rates for solar local time of day and geomagnetic latitude.

IV. Effects of Geomagnetic and Solar Irregularities on Sporadic-E Occurrence Rates

The purpose of this chapter is to analyze the effects of solar cycle and geomagnetic storming on derived Es rates from GPS-RO data for the 13 year period from 2006-2019. Chapter III set the baseline for expected rates over the globe during geomagnetic quiet conditions (Kp $\leq$ 4, AE $\leq$ 200 nT). Chapter IV will focus on temporal and spatial variations in Es occurrence rates from the quiet standard. Geomagnetic storming is measured in various ways, but for this study, we used four indices: AE Index, Kp Index, DST Index, and Bz. For a solar cycle analysis, we used the R sunspot number as an indicator of high or low solar activity. As in Chapter III, results are presented for both sporadic-E with any measurable fbEs (all-fbEs), and sporadic-E with an fbEs $\geq$ 3 MHz.

4.1 Kp: The Planetary K Index

It is only natural to start with the NOAA index of choice, Kp. Figure 28 shows two scatter plots of occurrence rates vs Kp index. The left chart is all-fbEs, and the right chart is any fbEs $\geq$ 3 MHz. The occurrence rate is plotted with a black dot, and standard error bars are in red. The dotted blue line is a linear regression, and the green dotted line is a polynomial average trend line. The linear fit correlation coefficient R_c^2 for the all-fbEs case is 0.37, and 0.16 for the $\geq$ 3 MHz case. Overall, the linear fit does well for Kp $\leq$ 5 in both cases, but there is far less data above Kp=5, so the fit is not quite as reliable.

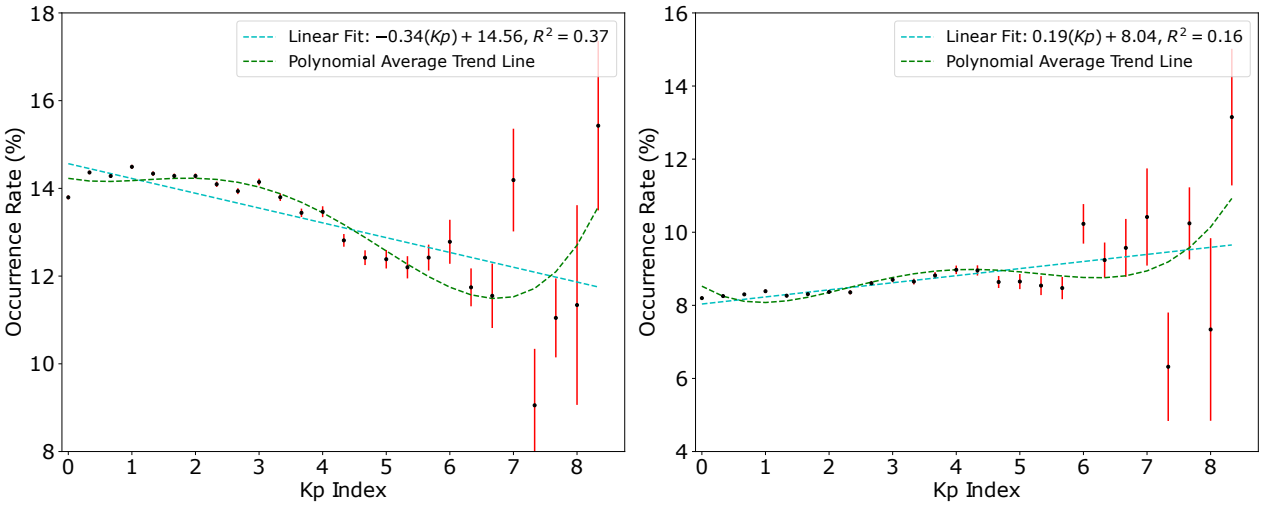

Figure 28. The Es occurrence rate as a function of Kp index, with all-fbEs on the left and fbEs $\geq$ 3 MHz on the right. Values are depicted with a black dot, and standard error is shown with red bars. A linear regression is displayed as a dashed blue line, with the slope, intercept and R_c^2 in the legend. A 4 degree polynomial fit of the average trend is shown in dashed green.

Interestingly, the slope for the all-fbEs is negative, whereas the fbEs $\geq$ 3 MHz plot has a positive slope. From this we can deduce that as the geomagnetic conditions become more active, the Es will be stronger but more infrequent. Geomagnetic storming leads to increased ionization rates at high latitudes (Matsushita, 1961), especially during a sudden commencement. That is justification enough for an increased rate of strong Es. However, it does not explain the dip in overall Es occurrence rates.

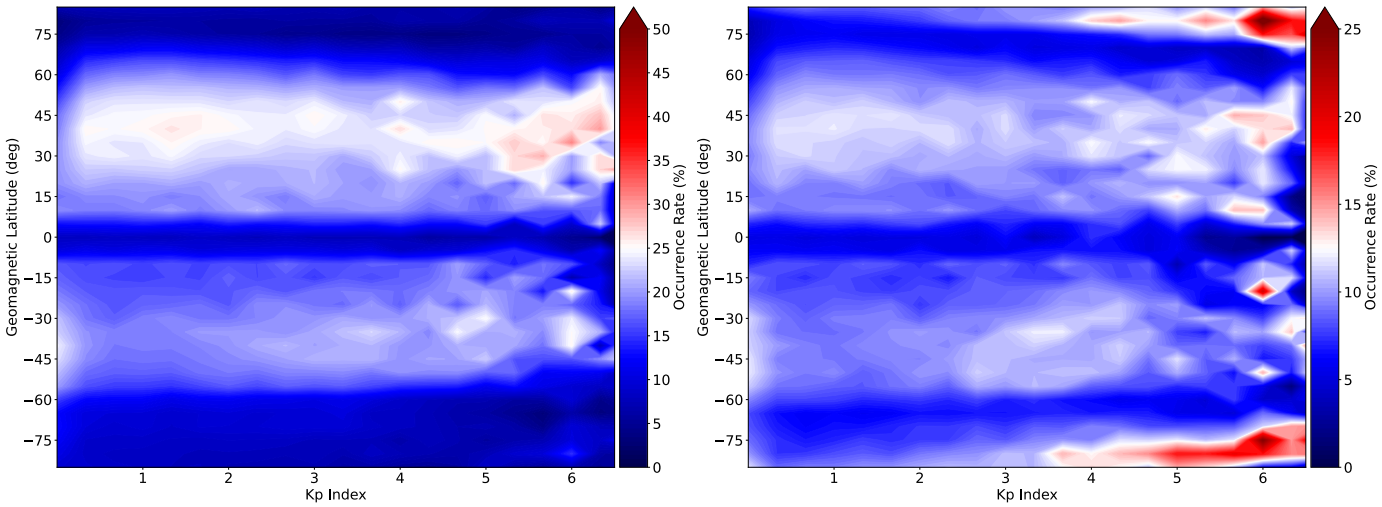

Figure 29. The Kp index is plotted against the geomagnetic latitude, with all-fbEs on the left and fbEs $\geq$ 3 MHz on the right. The mid-latitudes show higher ORs as Kp increases. For the fbEs $\geq$ 3 MHz in particular, the auroral regions are enhanced the most. In addition, the auroral zones move equatorward as Kp increases due to compression of Earth's magnetic fields during geomagnetic storming.

Figure 29 shows the occurrence rates for Kp index vs geomagnetic latitude, with all-fbEs on the left and $\geq$ 3 MHz on the right. Both charts are in good agreement between $\pm 60^o$ latitude. The mid-latitudes hold the highest ORs and the geomagnetic equator is quiet for all Kp. However, there is significant disagreement in the high latitude regions. In the chart to the right, the polar latitudes see more Es as the Kp index increases. This, again, is in good agreement with the increased ionization rates during geomagnetic storming (Matsushita, 1961). Likewise, there is evidence of the auroral oval moving further south during geomagnetic storming. If we assume that the polar Es in the fbEs $\geq$ 3 MHz (right) chart is within the auroral oval, we can use it as an indicator of the position of the auroral oval. Thus, as Kp values increase, the auroral oval moves further south. However, all of the auoral Es activity is absent from the all-fbEs chart on the left. There are a few potential reasons for this phenomena. The most likely is a shortcoming in the Yu S_4 technique when evaluating thick Es layers. If we assume that the Es layers are Gaussian lenses, a vertically thin, strong lens will provide ample perturbation to satisfy the required S_4 to satisfy the

technique. This suits the low and mid latitudes since the average Es layers is vertically thin per the spatial characteristics from Section 2.2. Auroral Es does not always form as thin layers parallel to the ground. Due to the geomagnetic field line geometry and nature of auroral activity, auroral Es can form slanted or be generally thicker than mid latitude Es (Whitehead, 1970). In either case, the signal path through auroral Es will be longer, so the S_4 perturbation will be smaller, whereas the phase perturbation will still be high. Therefore, the auroral Es would meet the Chu phase perturbation criteria, but not the S_4 criteria.

The other possibility is that the Yu S_4 technique is correctly not picking up on Es, and the Chu phase perturbation technique is errantly detecting auroral activity in the high latitude regions. Regardless, there is something disrupting the signal phase in the high latitudes regions, and it only appears during geomagnetic storming conditions. Maintaining the intent of this research to give a climatological study of Es (or Es-like ionospheric behavior) that affect HF signals (HF communication, over-the-horizon radar, HF geolocation, etc.), we assume the fbEs $\geq$ 3 MHz returns in the auroral regions during geomagneitc storming are in fact Es, and that the lack of returns for the all-fbEs method in the same region is a limitation of the S_4 signal due to layer thickness.

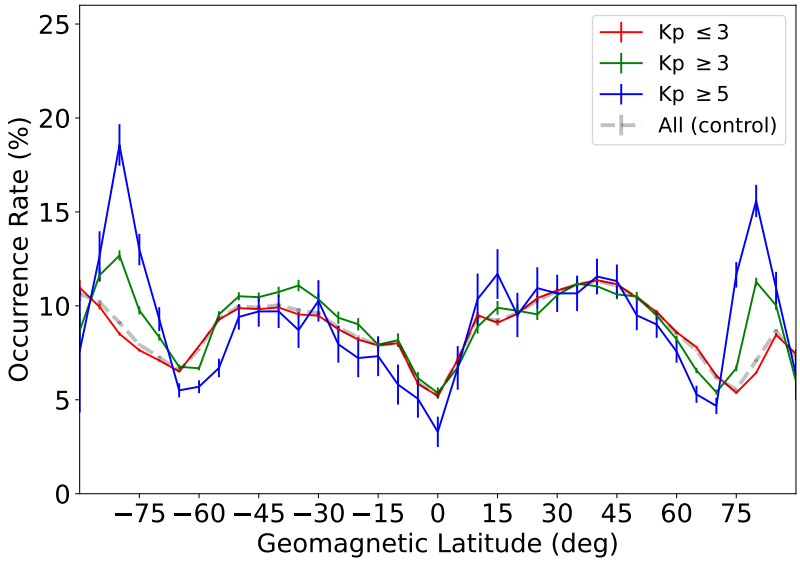

Figure 30. The occurrence rates for fbEs $\geq$ 3 MHz for various values of the Kp index. Standard error bars are shown with vertical bars.

Figure 30 shows various Kp ranges and the resulting occurrence rates vs geomagnetic latitude. Only the fbEs $\geq$ 3 MHz is used for this figure. The transparent grey line is the control, and includes all available observations. The red line, which is Kp $\leq$ 3, and represents quiet conditions, has little deviation from the control grey line. The quiet red line and control grey line are within 1% at all points throughout. The green line, which is Kp $\geq$ 3, represents any active geomagnetic conditions. The green line also remains within 2-3% of the grey control between +/-60^o inclination. However, at the high latitude regions in both hemispheres, the active green line begins to show large deviations from quiet. Active Es ORs are as high as 5% over the quiet red in the auroral zones. Lastly, the blue line is geomagnetic storming conditions, Kp $\geq$ 5. At high latitudes, the blue storming line shows nearly a 10% jump in Es ORs. For the low and mid latitudes, the control grey line is within the error bar for the storming blue line.

4.2 AE: The Auroral Electrojet Index

Figure 31 shows the occurrence rates of AE index, with linear regression and polynomial average trend line. Like Figure 28, the all-fbEs ORs are on the left, and $\geq$ 3 MHz is on the right. The slope and R_c^2 for the all-fbEs plot is not very enlightening, since both values are nearly zero. However, the trend below 1250 nT is negative, similar to the trend with Kp. The $\geq$ 3 MHz plot also has a low R_c^2 at 0.11, but the trend is a consistently positive below 1250 nT where the error bars are still relatively small. At an increase of 0.1% OR per 100 nT, the trend is not overwhelming.

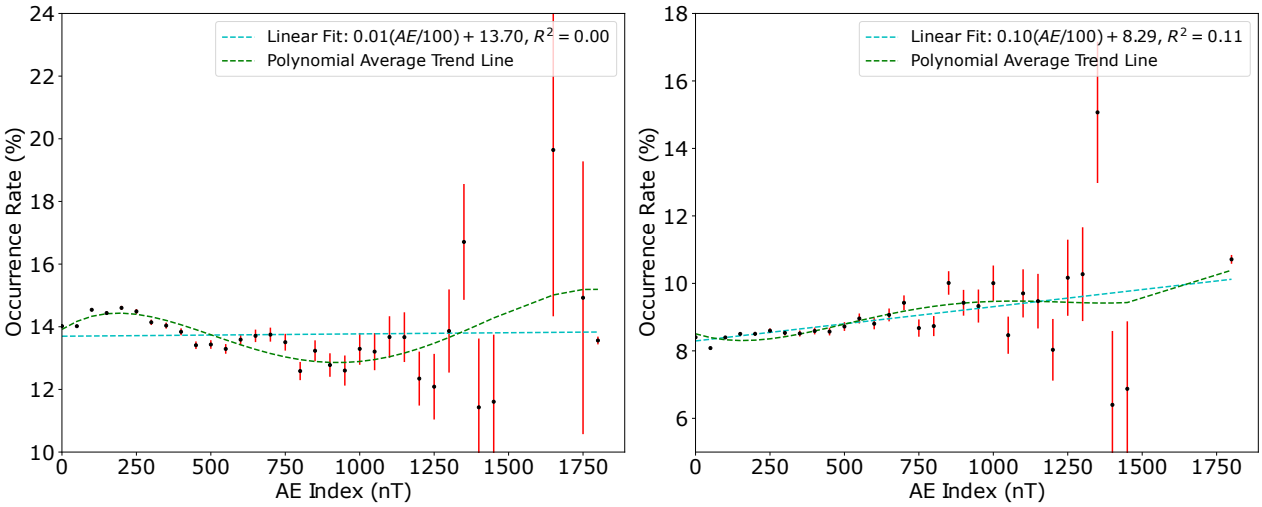

Figure 31. The Es occurrence rate as a function of AE index, with all-fbEs on the left and fbEs $\geq$ 3 MHz on the right. Values are depicted with a black dot, and standard error is shown with red bars. A linear regression is plotted as a dashed blue line, with the slope, intercept and R_c^2 in the legend. A 4^{th} degree polynomial fit of the average trend is plotted in dashed green.

Figure 32 shows the occurrence rates again for AE index vs geomagnetic latitude. For both cases, the mid-latitude region tells the same story. Rates are low when the AE index is low, especially under 500 nT. Below 250 nT, the $\geq$ 3 MHz plot rates are low for all latitudes. Above 500 nT, the occurrence rate significantly increases for the mid-latitudes regions. Focusing on the auroral region in the right plot, the AE

index seems to have a very strong correlation with Es activity for the high latitudes. As with the Kp index, the activity pushes further equatorward when the AE has higher values. This is to be expected as the auroral oval moves further south during geomagnetic storming, and reconfiguration of the magnetosphere. Since the AE index is a direct measurement of the auroral electrojet, it should be particularly suited for detection of auroral activity.

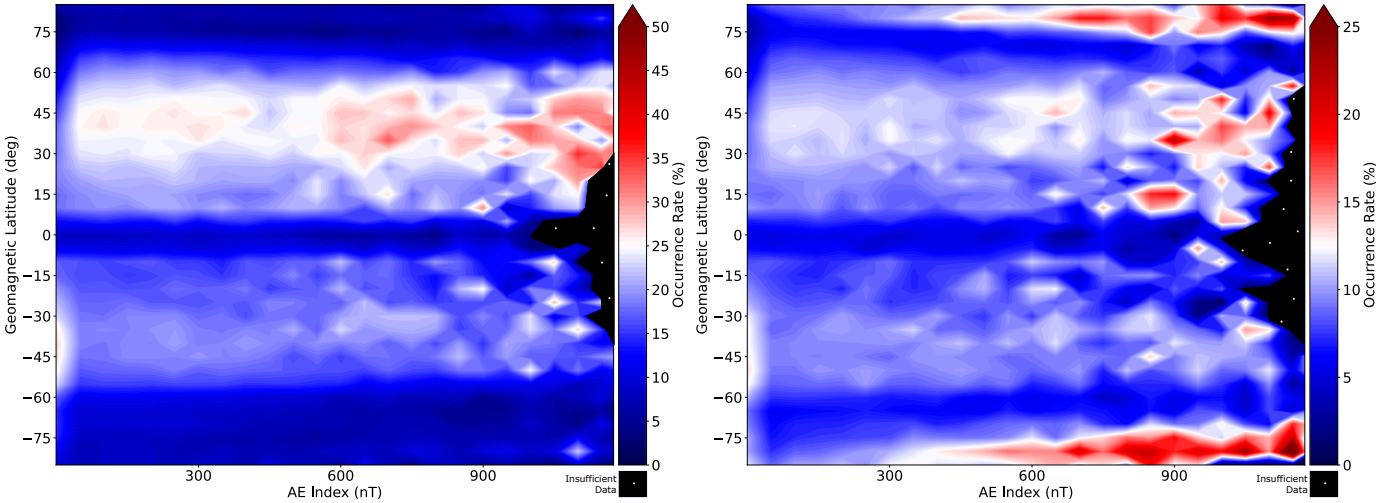

Figure 32. Es ORs as a function of the AE index and the geomagnetic latitude, with all-fbEs on the left and fbEs $\geq$ 3 MHz on the right. Similar to the Kp, the mid latitudes are enhanced at higher values of AE. Additionally, the auroral regions are most enhanced in the fbEs $\geq$ 3 MHz chart.

Focusing on the $\geq$ 3 MHz rates, Figure 33 shows Es occurrence rates along constant geomagnetic latitudes for various ranges of AE index values. Where Kp showed little indication of impacting fbEs rates within the +/-60^o range, AE shows a positive correlation. The quiet red (AE $<$ 100 nT) is again within 1% of the control, and typically less than the control. The active green (AE $>$ 150 nT) line is close but consistently higher than the control, especially in the high latitudes. The storming blue (AE $>$ 500 nT) line is much higher than the control. In the northern hemisphere, occurrence rates are up to 3-4% higher during storming observations. In the polar region, the increase is 5-8%.

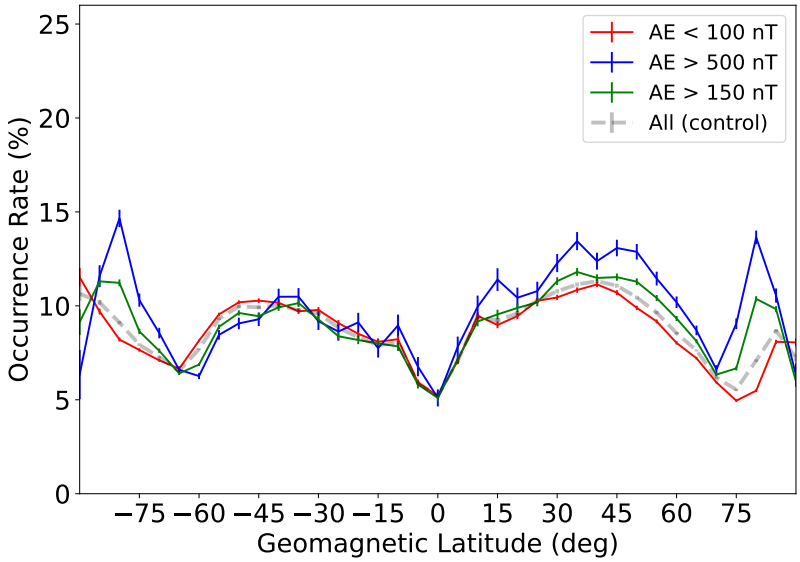

Figure 33. The occurrence rates for fbEs $\geq$ 3 MHz for various values of the AE index. Standard error bars are shown with vertical bars.

Surprisingly, these increased rates occur primarily in the winter hemisphere (i.e. the southern hemisphere in June, July, and August and vice versa). Figure 34 shows the Jun/Jul/Aug on the left and Dec/Jan/Feb on the right for the same AE index ranges. The summer hemisphere sees the characteristic peak in OR, and AE has little effect on overall ORs in the entire hemisphere. In the winter hemisphere for both time periods, the storming blue (AE $>$ 500 nT) shows a noticeable increase from the grey control.

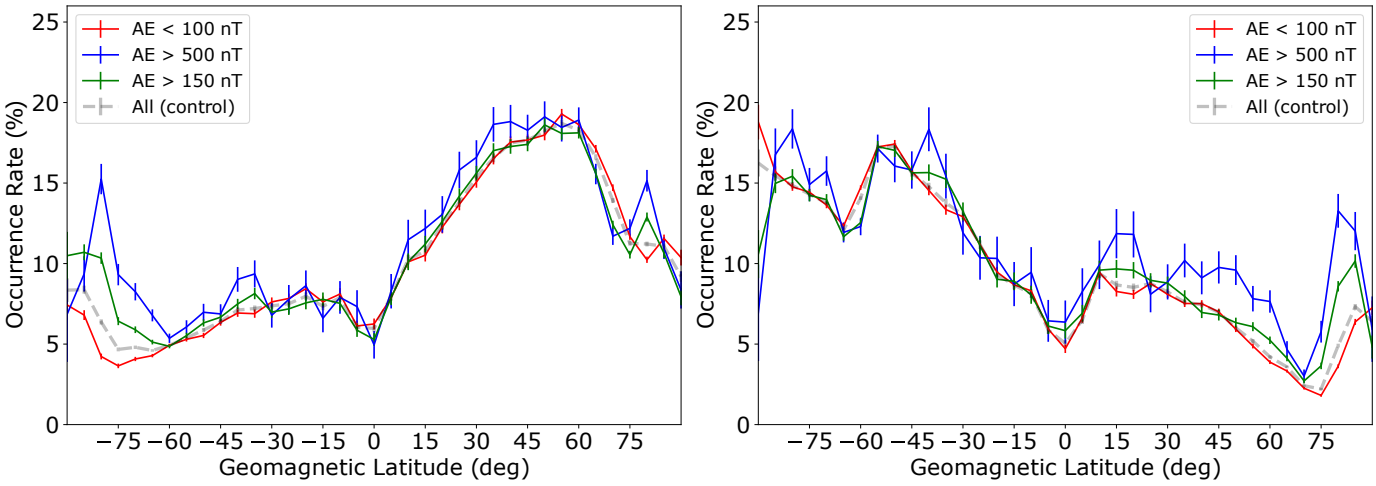

Figure 34. The occurrence rates for fbEs $\geq$ 3 MHz for various values of the Kp index for boreal summer (left) and boreal winter (right). Standard error bars are shown with vertical bars.

Figure 35 shows annual occurrence rates of fbEs $\geq$ 3 MHz for quiet conditions (AE $<$ 100 nT and Kp $<$ 3) on top, and active conditions (AE $>$ 200 or Kp $>$ 5) on bottom. Figure 36 is the geomagnetic latitude vs solar local time of day for the same conditions, with quiet on the left and active on the right. There is a noticeable increase in the mid-latitude regions during the active times for both figures, likely due to increased ionization rates and strong Es layers. Additionally, the sudden commencement increases ionization rates primarily in the high latitudes, and develops strong Es outside of the normal afternoon peak photoionization hours as seen in Figure 36. Common among both figures is the large amplification in auroral Es rates. Under quiet conditions, Es typically only forms during the six hour period from 1800-2400SL. When conditions are active, that timeline increases to an 18 hour period from 1400-0800SL. Figure 35 shows not only an amplification in ORs, but that the auroral zone seems to expand south in the northern hemisphere, and grows in all directions in the southern hemisphere. During quiet conditions, auroral Es was mostly contained to the 80^o contour in the southern hemisphere. Auroral Es rates span the entire Antarctic region during active geomagnetic conditions and the ORs are much higher.

There is precedent for enhanced auroral Es during geomagnetic storming, indicated by Abdu et al. (2014, 2013), due to an enhancement to the electric fields.

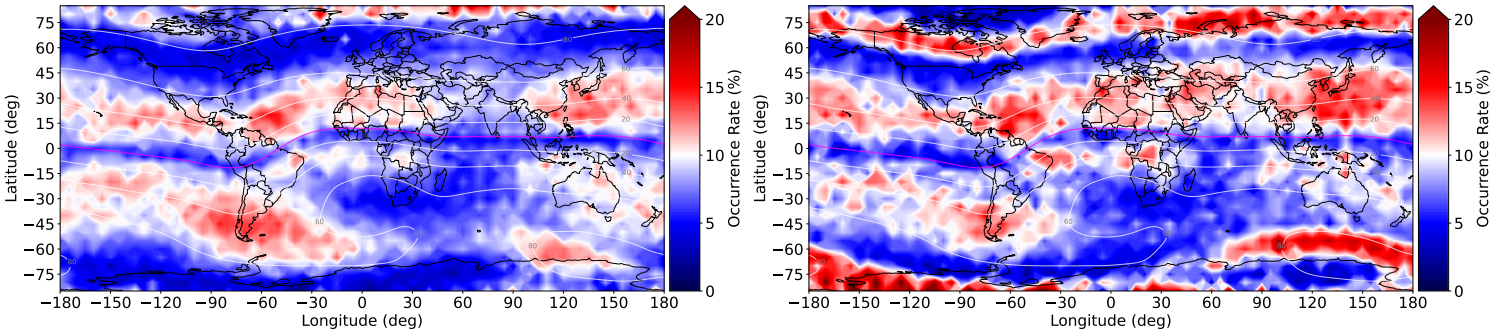

Figure 35. The fbEs ≥ 3 MHz global occurrence rates for quiet conditions (AE < 100 nT and Kp < 3) to the left, and active conditions (AE > 200 or Kp > 5) on the right.

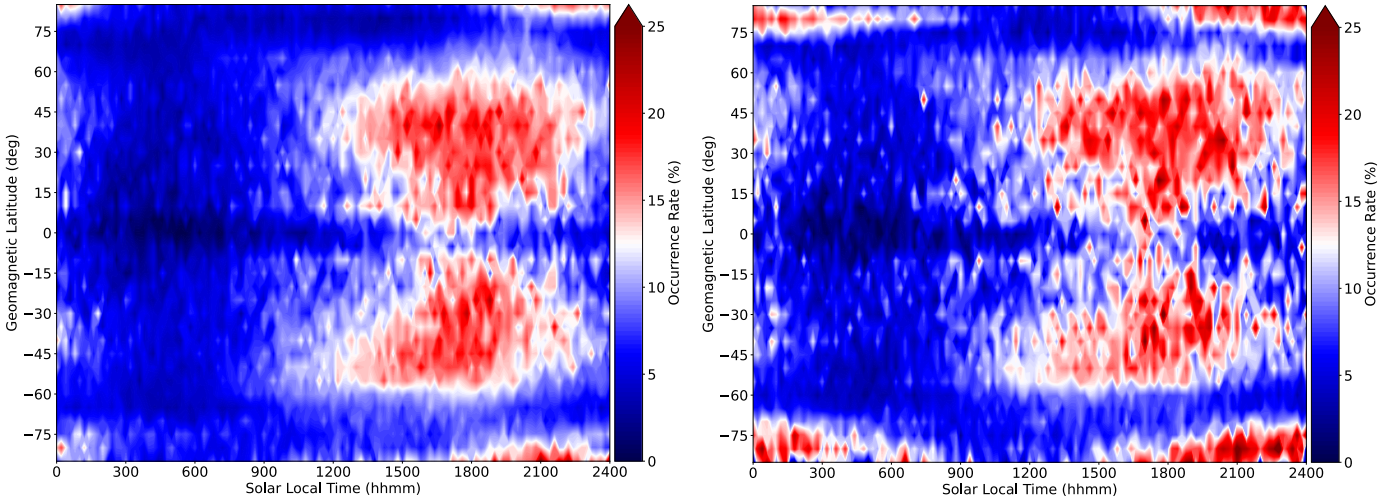

Figure 36. The fbEs ≥ 3 MHz diurnal occurrence rate for quiet conditions (AE < 100 nT and Kp < 3) to the left, and active conditions (AE > 200 or Kp > 5) on the right.

4.3 DST: The Disturbance Storm Time Index

Figure 37 shows two scatter plots of occurrence rates as a function of the DST index. The left chart is all-fbEs, and the right chart is any fbEs ≥ 3 MHz. The linear regression on both data sets are less than 0.1, and the slope for both are near zero. DST is difficult to quantify in this format since it is best viewed on a real-time basis to identify trends in the data. However, there are a couple trends that arise. First, a

large positive DST seems to indicate at least a positive trend in OR. A large positive DST signifies the sudden commencement period. In line with the AE and Kp, we expect to see increased ORs during the sudden commencement. Additionally, a large negative DST (<-100 nT) indicates a severe geomagnetic storm, and the OR trend points up as well.

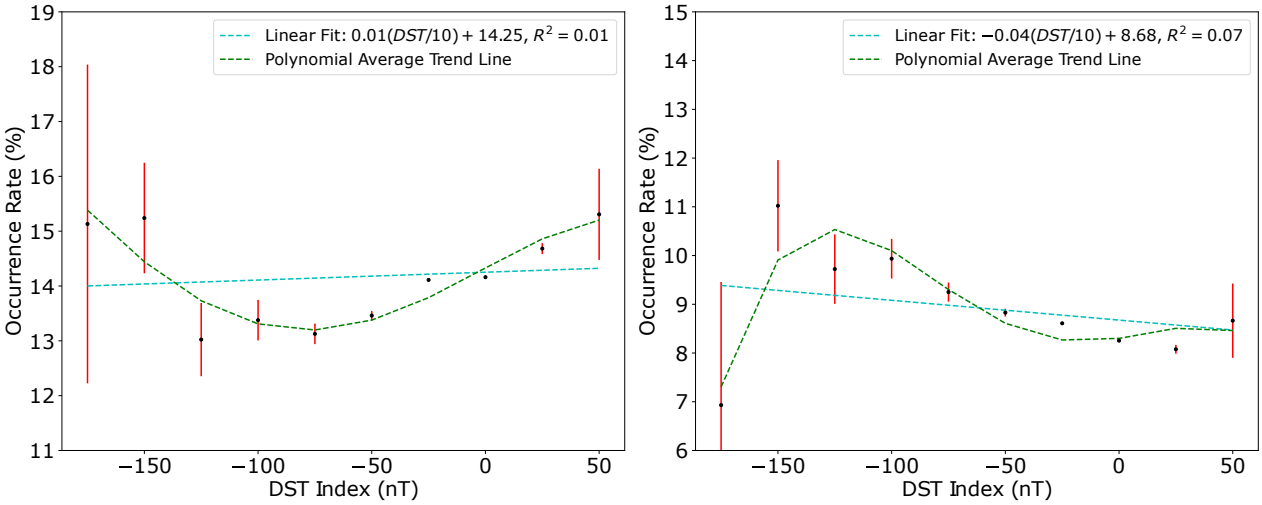

Figure 37. The Es occurrence rate as a function of DST index, with all-fbEs on the left and fbEs $\geq$ 3 MHz on the right. Values are depicted with a black dot, and standard error is shown with red bars. A linear regression is plotted as a dashed blue line, with the slope, intercept and R_c^2 in the legend. A 4 degree polynomial fit of the average trend is shown in dashed green.

Figure 38 shows the occurrence rates for DST index vs geomagnetic latitude, with all-fbEs on the left, and $\geq$ 3 MHz on the right. For strong negative DST, the mid latitudes see an OR enhancement, but the trend is mostly confined to the northern hemisphere. In line with Kp and AE, the $\geq$ 3 MHz shows a significant auroral enhancement in both hemispheres. The auroral enhancement only occurs for strong negative DST, not for weakly negative or strong positive DST. Due to the lack of any significant trends in the data, the DST is not as useful when determining Es ORs as the Kp and AE are.

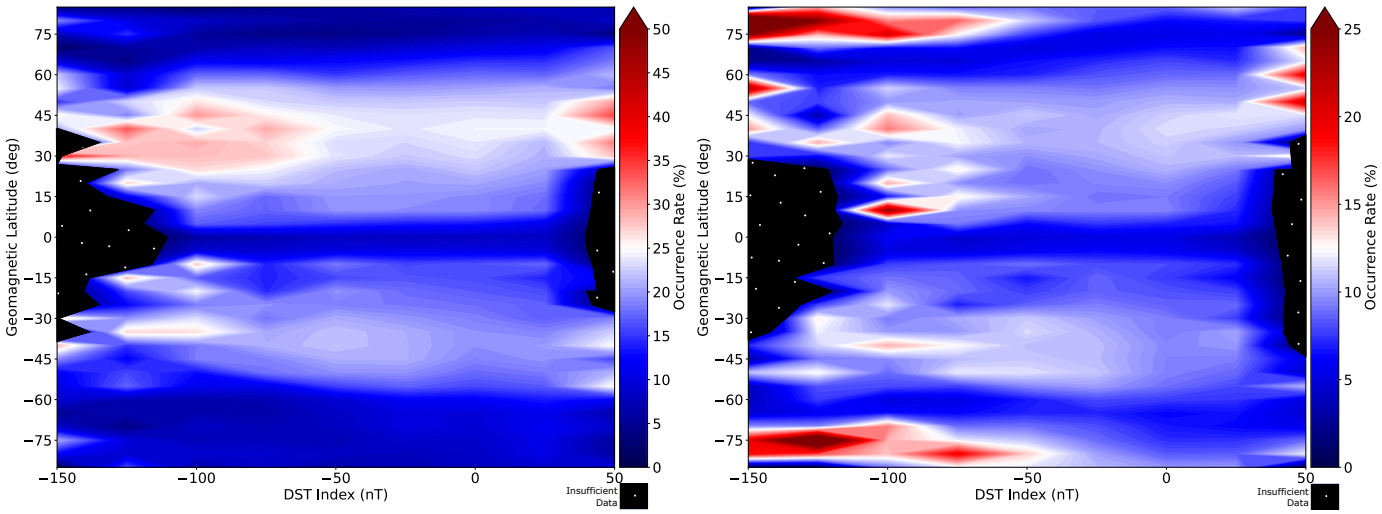

Figure 38. Es ORs as a function of the DST index and geomagnetic latitude, with all-fbEs on the left and fbEs $\geq$ 3 MHz on the right. Two common trends arise: the mid latitudes ORs are enhanced under strong DST, and the auroral region for the $\geq$ 3 MHz chart is most enhanced.

4.4 IMF Bz: The Vertical Component of the Interplanetary Magnetic Field

Figure 39 shows two scatter plots of occurrence rates vs the IMF Bz. The left chart is all-fbEs, and the right chart is any fbEs $\geq$ 3 MHz. The all-fbEs chart has a low R_c^2 and a near zero slope, so we will focus the analysis on the fbEs $\geq$ 3 MHz chart to the right. The R_c^2 is a high 0.59 with a slope of -0.09, and the strong Bz south ORs are much higher than the strong Bz north ORs. Per the discussion in Section 2.4.4, a high Bz in the positive or negative is indication of strong magnetic field impacts, but due to the magnetosphere geometry, a strong Bz south (negative) has a larger impact on Earth's magnetic field. A strong Bz south does not seem to correlate well with formation of any fbEs, but it does contribute to the formation of strong fbEs ($\geq$ 3 MHz), likely from elevated auroral activity.

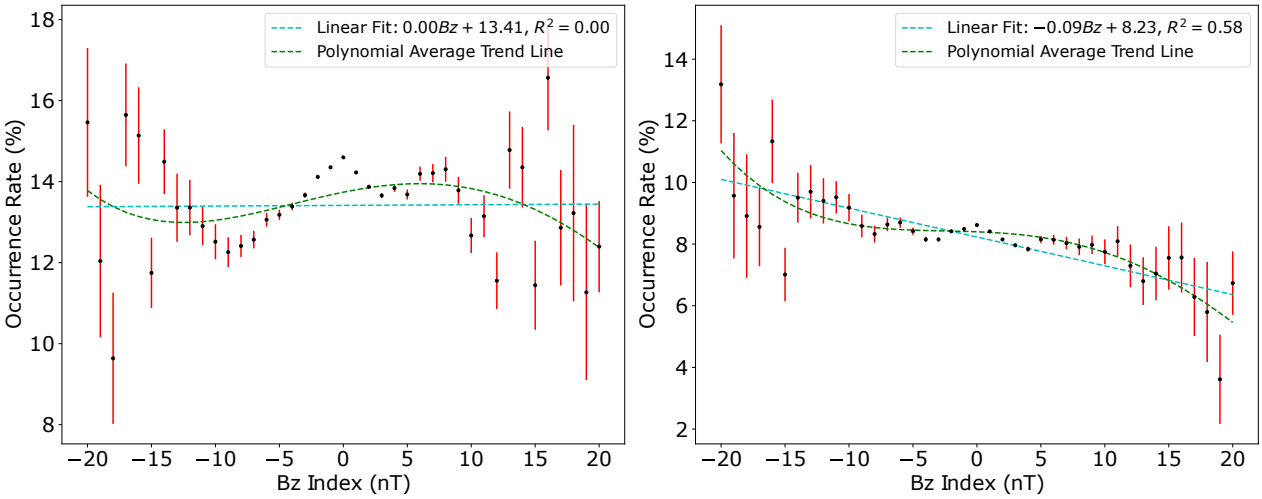

Figure 39. The Es occurrence rate as a function of Bz, with all-fbEs on the left and fbEs $\geq$ 3 MHz on the right. Values are depicted with a black dot, and standard error is shown with red bars. A linear regression is plotted as a dashed blue line, with the slope, intercept and R_c^2 in the legend. A 4^{th} degree polynomial fit of the average trend is shown in dashed green.

Figure 40 shows the occurrence rates for Bz vs geomagnetic latitude, with all-fbEs on the left, and $\geq$ 3 MHz on the right. The mid latitude regions for both charts show enhanced ORs at $|Bz| > 5$. The fbEs $\geq$ 3 MHz shows an enhanced auroral zone for only strong Bz south. The ORs steadily increase beginning at -5 Bz, and peak around -15 Bz. This could be due to an enhancement of the auroral electric field from reconnection when the Bz has a strong magnitude oriented southward (Nygrén et al., 2006). It could also simply be from enhanced auroral activty for Bz south.

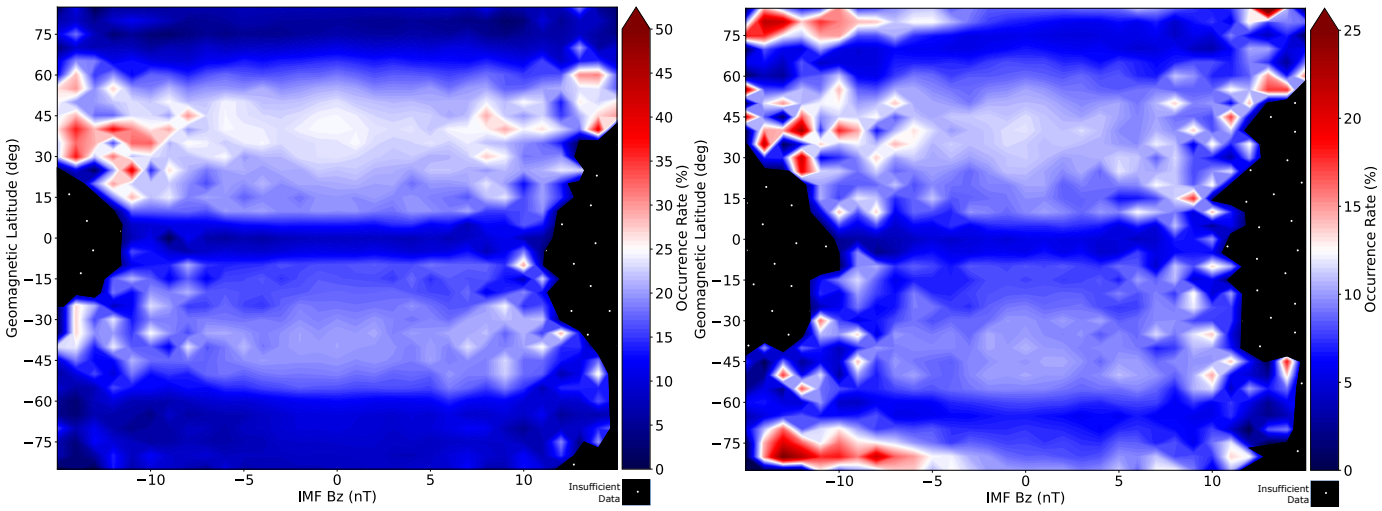

Figure 40. Es ORs as a function of the IMF Bz geomagnetic latitude, with all-fbEs on the left and fbEs $\geq$ 3 MHz on the right. While the mid latitude regions are enhanced, it's only under strong negative Bz. Additionally, the auroral region is enhanced under strong Bz south for the fbEs $\geq$ 3 MHz.

4.5 R: The Sunspot Number

Figure 41 shows two scatter plots of occurrence rates vs the R sunspot number. The left chart is all-fbEs, and the right chart is any fbEs $\geq$ 3 MHz. The R_c^2 for each chart is the highest of any index compared in this study, for their respective data sets. Solar cycle has a strong negative correlation with Es OR. The slope for both plots is a consistent -0.15 %/10R.

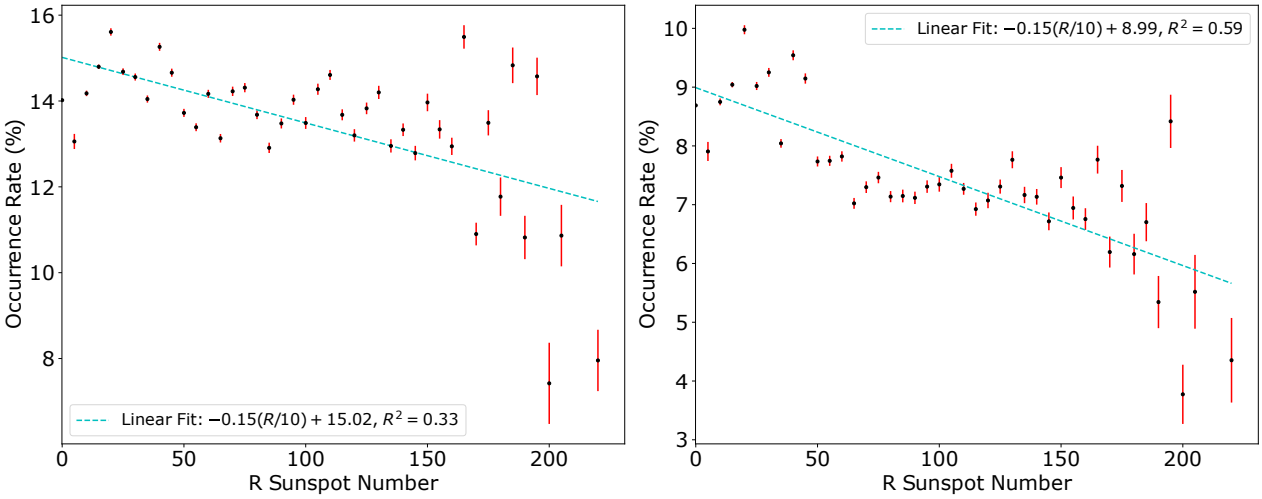

Figure 41. The Es occurrence rate as a function of the R sunspot number, with all-fbEs on the left and fbEs $\geq$ 3 MHz on the right. Values are depicted with a black dot, and standard error is shown with red bars. A linear regression is plotted as a dashed blue line, with the slope, intercept and R_c^2 in the legend. A 4^{th} degree polynomial fit of the average trend is plotted in dashed green.

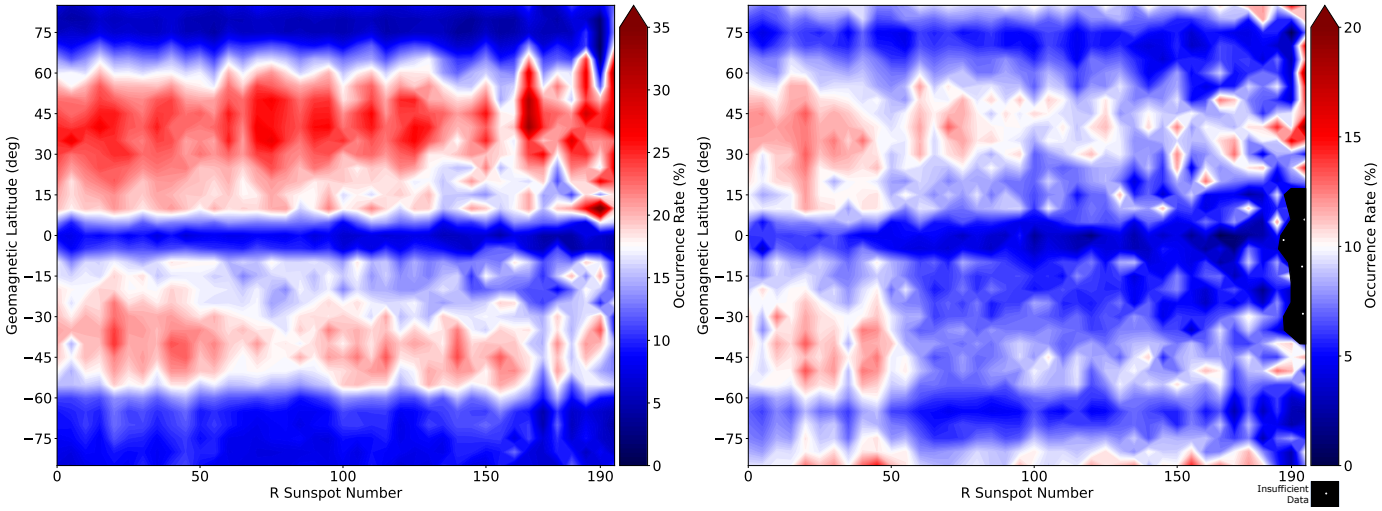

Figure 42. The R sunspot number is plotted against the geomagnetic latitude, with all-fbEs on the left and fbEs $\geq$ 3 MHz on the right. Contrary to the geomagnetic indices, there is not a major enhancement to the mid latitudes or auroral regions. The highest ROs are actually when the sun is quiet (R $<$ 50).

Figure 42 shows the occurrence rates as a function of the R sunspot number vs geomagnetic latitude, with all-fbEs on the left, and $\geq$ 3 MHz on the right. While the all-fbEs plot shows a negative correlation, the fbEs $\geq$ 3 MHz shows a large

drop in Es ORs after 50 R. Figure 43 shows the fbEs $\geq$ 3 MHz occurrence rate for various sunspot number ranges, plotted against geomagnetic latitude. Instead of a large auroral enhancement, the solar cycle only has an impact on the low and mid latitudes between $\pm 60^o$ inclination. For the red solar minimum line (R Sunspot # $<$ 50), Es ORs are higher than the grey control everywhere but the high latitudes where they are about equal. On the contrary, the blue solar maximum line (R Sunspot # $>$ 125) is well below the control and quiet red lines, except in the auroral zones where the rates are equal again. The trend is the same for all seasons as shown in Figure 44, which separates by boreal summer (left) and boreal winter (right). The AE seasonal comparison (Figure 34) showed that the AE impacted the hemisphere in local winter more than the local summer. However, the solar cycle impacts the entire global ORs equally.

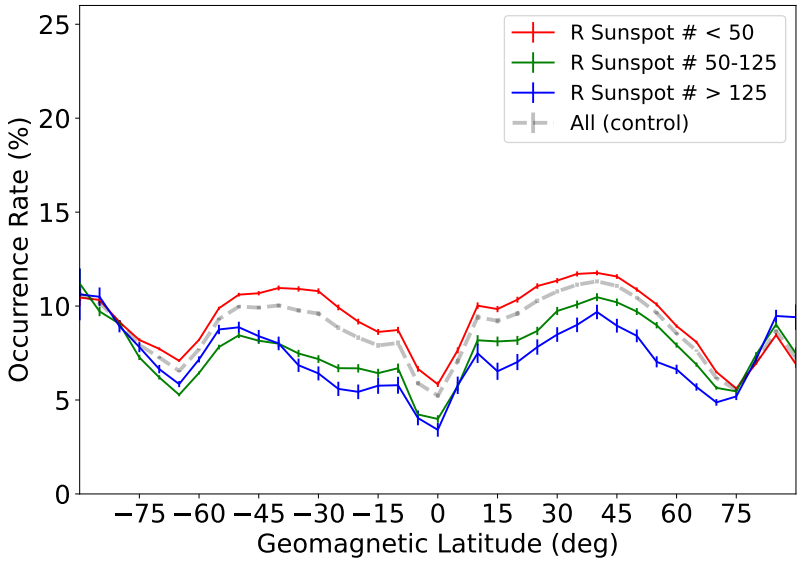

Figure 43. The occurrence rates for fbEs $\geq$ 3 MHz for various values of the R Sunspot Number. Standard error bars are shown with vertical bars.

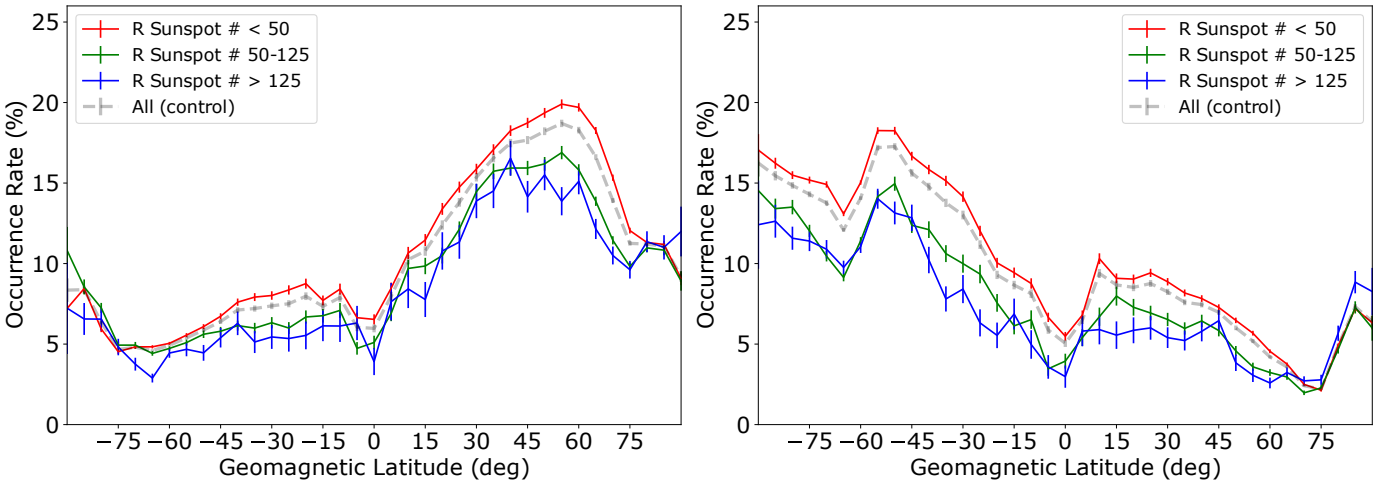

Figure 44. The occurrence rates for fbEs $\geq$ 3 MHz for various values of the R sunspot number for boreal summer (left) and boreal winter (right). Standard error bars are shown with vertical bars.

Figure 45 and Figure 46 are comparisons of annual Es ORs for solar quiet (R Sunspot # $<$ 50) vs solar active (R Sunspot # $\geq$ 50). Figure 45 shows the geographic profile of Es OR, and Figure 46 shows the diurnal morphology, with quiet on the left and active on the right for both figures. The reason the solar active Es ORs are lower than the solar quiet is likely due to one of two reasons. The first reason may be due to the nature of GPS-RO signals and the fluctuation of background ionospheric densities over a solar cycle. GPS-RO is not directly measuring electron density like a Digisonde. Instead, GPS-RO is measuring signal amplitude and phase through a GPS wave that traverses a path between the two satellites. As shown by Haldoupis et al. (2020), the fbEs measured by GPS-RO is just a perturbation from the background environment. If the environment were amplified by the solar cycle, the perturbation would be less intense when compared to the enhanced background signal. Thus, the post-processing techniques would be less likely to trigger a positive response from an Es layer. While this may explain the low and mid latitude decrease in Es OR while the sun is active, it doesn't explain the neutrality around the poles (Figure 43). Analysis from Akchurin et al. (1995), Maksyutin and Sherstyukov (2005),

and Zhang et al. (2015) shows a similar negative trend to the solar cycle Es rate. Maksyutin and Sherstyukov (2005) noted that the chemistry in Es layers changes as the magnitude increases. For weaker Es layers, neutral atmosphere ionization is just as likely to contribute to the Es layer as the ionized metals. However, as the magnitude increases, metallic ions dominate. While atmospheric ionization rates increase during solar maximum, metallic ionization rates remain unchanged. Solar cycle thus is more likely to increase the density of daytime Es layers than to increase the occurrence frequency. Furthermore, Akchurin et al. (1995) found that active solar conditions affected the ideal global wind patterns for mid latitude formation of Es layers. Through a case study for a single site in central Russia, Akchurin et al. (1995) showed in the E-layer altitudes, a prevailing southeast wind in the mid latitudes is best for Es formation because it will maintain the ideal wind shear to force vertical ion drifts and prevent Es dissipation. During solar active conditions, it was found that this southeast wind was degraded, thus preventing vertical ion drift and washing away strong metallic ions. This trend is better correlated with stronger Es layers where metallic ions dominate the chemical composition (Akchurin et al., 1995; Zhang et al., 2015). Weaker layers tended to have a positive daytime correlation and neutral overall correlation (negative at nighttime) (Zhang et al., 2015). Figure 42 mirrors the trend for a global scale. For the all-fbEs plot on the left, the Es rate remains relatively constant throughout the time period. For the stronger Es cutoff on the right, ORs are higher for solar quiet ($R<50$) than for solar active ($R\geq50$).

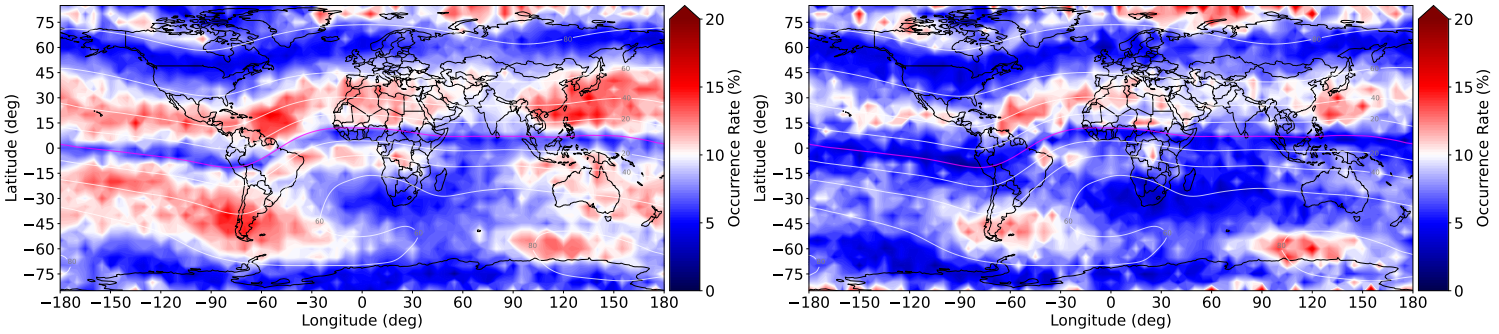

Figure 45. The fbEs $\geq$ 3 MHz global occurrence rate for solar minimum (R sunspot number $<$ 50) on left, and solar maximum (R sunspot number $\geq$ 50) on the right.

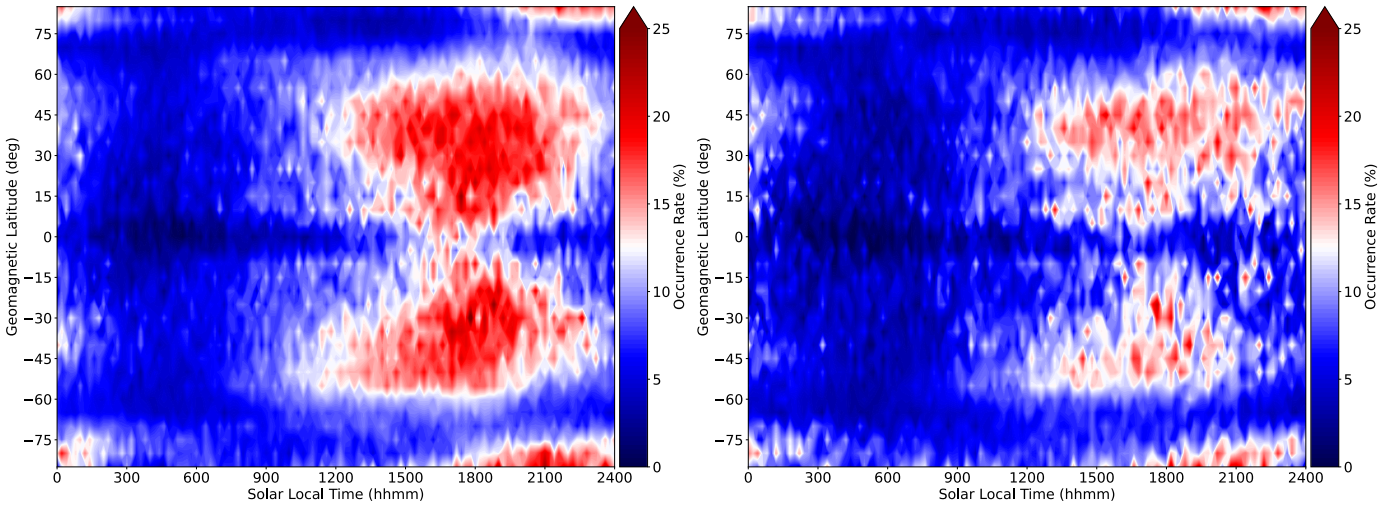

Figure 46. The fbEs $\geq$ 3 MHz diurnal occurrence rate for solar minimum (R sunspot number $<$ 50) on top, and solar maximum (R sunspot number $\geq$ 50).

V. Conclusions

This study analyzed GPS-RO soundings and Digisonde ionograms to provide a global Es climatology for two intensity thresholds: all-fbEs and fbEs $\geq$ 3 MHz. The climatological analysis was compared to various geomagnetic and solar activity indices to determine the Es formation response to different conditions. The goal of this research is to aid in Air Force HF radio wave application, such as HF geolocation and over-the-horizon radar. Both applications require knowledge of the ionosphere behavior because they are relying on signals reflected off the ionosphere. As an anomalously strong, low layer of the ionosphere, Es can significantly reduce the effectiveness of HF radio wave applications.

To build the global climatology, observations from 65 Digisonde sites and the COSMIC GPS-RO constellation were used from September 2006 - February 2019. ARTIST 5 auto scaling software was used to process the Digisonde site observations, totaling 13,141,060 observations. Two techniques developed by Chu et al. (2014) and Yu et al. (2019), and fine tuned by Carmona (2021), were used to process occultation from the COSMIC CDAAC database. This provided two data sets to analyze: fbEs $\geq$ 3 MHz, and fbEs with no lower limit. The two data sets had 5,081,226 and 3,991,696 observations respectively (Figure 12).

The fbEs $\geq$ 3 MHz has rates approximately equal to half of the all-fbEs rates. Annually, Es ORs are most prevalent in the low and mid latitudes between 10^o-60^o geomagnetic latitude. Within the SAA, the geomagnetic inclination angle is high enough to inhibit Es formation in line with the wind shear theory. Likewise, along the geomagnetic equator, there is a clear lack of Es formation as the inclination angle is at or near 0^o. When mapping on a geomagnetic latitude adjusted map, the SAA is still present between 30^o-90^o longitude due to reduced geomagnetic field magnitudes.

Seasonally, Es ORs are elevated during the summer months for each hemisphere

due to a seasonal dependence in meteoric deposits shown by Haldoupis et al. (2007); Singer et al. (2004). The boreal spring and fall seasons are characterized by very low Es ORs world wide for both data sets since meteoric deposits peak over the equatorial region which inhibits Es due to low magnetic inclination angle. During boreal winter, the southern hemisphere is dominated by Es, except within the SAA, where high inclination angle and weak magnetic field still inhibits development. Otherwise, the Es mostly forms between 10^o-60^o geomagnetic latitude. During the boreal summer, the northern hemisphere is dominated by Es. However, there is an anomalous region over North America which has 10-15% lower ORs than the rest of the northern hemisphere mid latitude region. The low ORs are likely a result of an anomalous geographical dependence of vertical wind shear over North America shown by Shinagawa et al. (2017) using data from the GAIA model.

Monthly, Es ORs are highest in the southern hemisphere from November through February, and in the northern hemisphere from May through August. March, April, September, and October are the true transition seasons when the large band of high Es occurrence rates would be over the equatorial region, but the geomagnetic equator is inhibiting the formation of Es. Again, the fbEs $\geq$ 3 MHz ORs are about half of the all-fbEs rates on average.

Diurnally, Es is sharply peaked in the afternoon. The all-fbEs ORs have a maximum from 1600 to 1700SL, and the highest ORs last from 1200SL through 2100SL. The fbEs $\geq$ 3 MHz has a maximum from 1700 to 1900SL, and the highest ORs begin around 1200SL and continue until midnight, and are roughly half the magnitude of the all-fbEs rates. Therefore, the stronger Es layers form slightly later and last longer on average. For both data sets, there is evidence of auroral Es from 1800 to 0300SL, with a maximum around 2200 to 2300SL. For the hemisphere in the summer season, Es ORs are enhanced nearly the entire day, and for the stronger fbEs

$\geq$ 3 MHz set, the enhanced region stretches 23 hours. Therefore, it is thought that the stronger layers rarely fully dissipate overnight, but may weaken slightly and then become re-enhanced after sunrise.

The Kp index has a somewhat complicated relationship with global Es ORs. In the low and mid latitude regions, Kp value had little impact on Es ORs. It was in the auroral regions that Kp had a strong positive correlation with Es OR, especially in the fbEs $\geq$ 3 MHz data set. The all-fbEs data set did not reflect the same auroral enhancement, likely due to a shortcoming of the S_4 measurement in thicker Es layers. In auroral Es, the Es layers are thicker than standard Es, and the GPS signal traveling through the thick layer registers a smaller S_4 signature, so the Yu S_4 technique used in the all-fbEs technique failed to detect auroral Es.

The AE index was positively correlated with Es ORs for mid latitudes and the auroral region. The Kp index is calculated from measuring stations in both the mid latitudes and sub-auroral region, whereas the AE index is calculated from stations positioned solely in the auoral oval. Therefore, it is surprising that the AE is so well correlated with Es OR while the Kp is not. Since the AE index is a measure of the auroral electrojet, it is surprising it gives such a good indication of global Es ORs. In the mid latitudes, Es ORs strongly increase for AE values $>$ 600 nT. For the auroral zones, the AE values as low as 300 nT show a sharp increase in Es ORs, and it is independent of season.

The DST and IMF Bz are both correlated with Es OR, but they have a much weaker relationship than Kp and AE. The DST is a difficult index to quantify in a statistical study like this since it is best used as a relative number to determine timing of onset and commencement, as well as peak intensity. Large negative DST values are strongly correlated auroral enhancements, and to a lesser extent in the mid latitudes. The DST impact on Es ORs is a prime area for further research. As for Bz, only a

strong negative value (Bz south) was shown to significantly increase the Es ORs. For a strong Bz south geometry, the auroral and mid latitude Es had larger ORs. A Bz south IMF will cause magnetic reconnection with the geomagnetic field, which can increase the field line electric fields (Nygrén et al., 2006). This primarily enhances the auroral electric fields, but can reach as far equatorward as the mid latitudes for strong Bz south.

Sunspots are negatively correlated with Es rates. Figure 41 shows a relatively high R^2 for an overall negatively correlated trend for both data sets. The trend continues for all low and mid latitude regions, but the high latitude auroral regions are unaffected. The negative overall trend in Es ORs as a function of R is likely due to a degradation in the prevailing neutral winds that is unfavorable to strong Es formation. Akchurin et al. (1995) showed that enhanced solar activity prevents the ideal southeast prevailing winds that would ordinarily create the conditions for vertical ion drifts in line with the wind shear theory (Haldoupis, 2011). Without the vertical ion drift, the metallic ions are free to dissipate and recombine, inhibiting Es formation.

Future work should primarily focus on Es response to geomagnetic activity. Auroral Es has been the most critical ingredient in the geomagnetic analysis, so an evaluation of GPS-RO performace at high latitudes for each technique is critical. This analysis would add another element of reliability to the Es geomagnetic response analysis. In addition to the auroral response of geomagnetic storms, the decrease in Es rate for enhanced solar conditions should be further evaluated. Specifically, comparing Es rates for Digisonde locations in solar max and solar min would be useful. Other future work should include more detailed analysis of DST. Specifically, evaluating Es rates during each of the three phases outlined by DST would be beneficial.

Bibliography

Abdu, M. A., de Souza, J. R., Batista, I. S., Santos, A. M., Sobral, J. H., Rastogi, R. G., and Chandra, H. (2014). The role of electric fields in sporadic E layer formation over low latitudes under quiet and magnetic storm conditions. *Journal of Atmospheric and Solar-Terrestrial Physics*, 115-116:95–105.

Abdu, M. A., Souza, J. R., Batista, I. S., Fejer, B. G., and Sobral, J. H. (2013). Sporadic E layer development and disruption at low latitudes by prompt penetration electric fields during magnetic storms. *Journal of Geophysical Research: Space Physics*, 118:2639–2647.

Akchurin, A. D., Zykov, E. Y., Makarov, N. A., Minullin, R. G., Portnyagin, Y. I., and Sherstyukov, O. N. (1995). The effect of lower thermosphere dynamics on the occurrence of a sporadic E layer. *GEOMAGNETISM AND AERONOMY C/C OF GEOMAGNETIZM I AERONOMIIA*, 35:250–254.

Arras, C. and Wickert, J. (2018). Estimation of ionospheric sporadic E intensities from GPS radio occultation measurements. *Journal of Atmospheric and Solar-Terrestrial Physics*, 171:60–63.

Baggaley, W. J. (1984). Three solar cycles of day-time southern hemisphere Es activity. *Journal of atmospheric and terrestrial physics*, 46:207–210.

Baggaley, W. J. (1985). Changes in the frequency distribution of f0Es and fbEs over two solar cycles. *Planetary and space science*, 33:457–459.

Bartels, J., Heck, N. H., and Johnston, H. F. (1939). The three-hour-range index measuring geomagnetic activity.

Bates, D. and Dalgarno, A. (1962). Electronic recombination. *Pure and Applied Physics*, 13:245–271.

Batista, I. S. and Abdu, M. A. (1977). Magnetic storm associated delayed sporadic E enhancements in the Brazilian Geomagnetic Anomaly. *Journal of Geophysical Research*, 82:4777–4783.

Buchert, S., Zangerl, F., Sust, M., André, M., Eriksson, A., Wahlund, J., and Opgenoorth, H. (2015). SWARM observations of equatorial electron densities and topside GPS track losses. *Geophysical Research Letters*, 42:2088–2092.

Carmona, R. A. (2021). A Comparison of Sporadic-E Occurrence Rates Using Ionosonde and GPS Radio Occultation Measurements.

Cathey, E. H. (1969). Some midlatitude sporadic-E results from the Explorer 20 satellite. *Journal of Geophysical Research*, 74:2240–2247.

CDAAC (2020). CDAAC: COSMIC Data Analysis and Archive Center.

Chen, F. F. (2012). *Introduction to plasma physics*. Springer Science & Business Media.

Chu, Y. H., Wang, C. Y., Wu, K. H., Chen, K. T., Tzeng, K. J., Su, C. L., Feng, W., and Plane, J. M. (2014). Morphology of sporadic E layer retrieved from COSMIC GPS radio occultation measurements: Wind shear theory examination. *Journal of Geophysical Research: Space Physics*, 119:2117–2136.

Clette, F., Svalgaard, L., Vaquero, J. M., and Cliver, E. W. (2014). Revisiting the sunspot number: A 400-year perspective on the solar cycle.

Coleman, C. J. (1998). A ray tracing formulation and its application to some problems in over-the-horizon radar. *Radio Science*, 33:1187–1197.

Davies, K. and Hartmann, G. K. (1997). Studying the ionosphere with the Global Positioning System. *Radio Science*, 32:1695–1703.

Davis, T. N. and Sugiura, M. (1966). Auroral electrojet activity index AE and its universal time variations. *Journal of Geophysical Research*, 71:785–801.

Echer, E., Gonzalez, W. D., and Tsurutani, B. T. (2011). Statistical studies of geomagnetic storms with peak Dst $\leq$ -50 nT from 1957 to 2008. *Journal of Atmospheric and Solar-Terrestrial Physics*, 73:1454–1459.

Fabrizio, G. A. (2013). *High frequency over-the-horizon radar: fundamental principles, signal processing, and practical applications*. McGraw-Hill Education.

Fong, C., Yang, S., Chu, C., Huang, C., Yeh, J., Lin, C., Kuo, T., Liu, T., Yen, N. L., Chen, S., et al. (2008). FORMOSAT-3/COSMIC constellation spacecraft system performance: After one year in orbit. *IEEE Transactions on Geoscience and Remote Sensing*, 46:3380–3394.

Gooch, J. Y., Colman, J. J., Nava, O. A., and Emmons, D. J. (2020). Global ionosonde and GPS radio occultation sporadic-E intensity and height comparison. *Journal of Atmospheric and Solar-Terrestrial Physics*, 199:105200.

Haldoupis, C. (2011). A Tutorial Review on Sporadic E Layers. *Aeronomy of the Earth's Atmosphere and Ionosphere*, pages 381–394.

Haldoupis, C., Haralambous, H., and Meek, C. (2020). On the necessity of using foμEs instead of foEs in estimating the intensity and variability of sporadic E layers. *Journal of Atmospheric and Solar-Terrestrial Physics*, 206:105327.

Haldoupis, C., Pancheva, D., Singer, W., Meek, C., and MacDougall, J. (2007). An explanation for the seasonal dependence of midlatitude sporadic E layers. *Journal of Geophysical Research: Space Physics*, 112.

Headrick, J. M., Anderson, S. J., and Skolnik, M. (2008). HF over-the-horizon radar. *Radar handbook*, 20.

Hysell, D. L., Nossa, E., Larsen, M. F., Munro, J., Sulzer, M. P., and González, S. A. (2009). Sporadic E layer observations over Arecibo using coherent and incoherent scatter radar: Assessing dynamic stability in the lower thermosphere. *Journal of Geophysical Research: Space Physics*, 114.

ISES (2021). International Space Environmental Services (ISES) Solar Cycle Progression.

Jain, A., Pagani, P., Fleury, R., Ney, M. M., and Pajusco, P. (2018). HF source geolocation using an operational TDoA receiver network: Experimental results. *IEEE Antennas and Wireless Propagation Letters*, 17:1643–1647.

Jawad, M., Rafique, A., Khosa, I., Ghous, I., Akhtar, J., and Ali, S. M. (2019). Improving disturbance storm time index prediction using linear and nonlinear parametric models: A comprehensive analysis. *IEEE Transactions on Plasma Science*, 47:1429–1444.

Johnson, C. Y. (1966). Ionospheric composition and density from 90 to 1200 kilometers at solar minimum. *Journal of Geophysical Research*, 71:330–332.

Kamide, Y. and Akasofu, S.-I. (1983). Notes on the auroral electrojet indices. *Reviews of Geophysics*, 21:1647–1656.

Kepkar, A., Arras, C., Wickert, J., Schuh, H., Alizadeh, M., and Tsai, L.-C. (2020). Occurrence climatology of equatorial plasma bubbles derived using formosat-3/ cosmic gps radio occultation data. In *Annales Geophysicae*, volume 38, pages 611–623. Copernicus GmbH.

Kintner, P. M., Ledvina, B. M., and Paula, E. R. D. (2007). GPS and ionospheric scintillations. *Space weather*, 5.

Kyoto, W. (2022). Geomagnetic Auroral Electrojet (AE) Index Home Page.

MacDougall, J. W., Plane, J. M. C., and Jayachandran, P. T. (2000). Polar cap sporadic-E: part 2, modeling. *Journal of Atmospheric and Solar-Terrestrial Physics*, 62:1169–1176.

Maeda, J. and Heki, K. (2015). Morphology and dynamics of daytime mid-latitude sporadic-E patches revealed by GPS total electron content observations in Japan Aeronomy. *Earth, Planets and Space*, 67.

Maksyutin, S. V. and Sherstyukov, O. N. (2005). Dependence of E-sporadic layer response on solar and geomagnetic activity variations from its ion composition. *Advances in Space Research*, 35:1496–1499.

Mannucci, A., Iijima, B., Lindqwister, U., Pi, X., Sparks, L., and Wilson, B. (1999). GPS and ionosphere. *URSI Reviews of Radio Science*.

Mathews, G. and Towheed, S. S. (1995). NSSDC OMNIWeb: The first space physics WWW-based data browsing and retrieval system. *Computer Networks and ISDN Systems*, 27:801–808. Proceedings of the Third International World-Wide Web Conference.

Mathews, J. D. (1998). Sporadic E: current views and recent progress. *Journal of atmospheric and solar-terrestrial physics*, 60:413–435.

Matsushita, S. (1961). Increase of ionization associated with geomagnetic sudden commencements.

Maus, S., Macmillan, S., McLean, S., Hamilton, B., Thomson, A., Nair, M., and Rollins, C. (2010). The US/UK world magnetic model for 2010-2015.

Merriman, D. K., Nava, O. A., Dao, E. V., and Emmons, D. J. (2021). Comparison of Seasonal foEs and fbEs Occurrence Rates Derived from Global Digisonde Measurements. *Atmosphere*, 12:1558.

Moro, J., Resende, L. C., Denardini, C. M., Xu, J., Batista, I. S., Andrioli, V. F., Carrasco, A. J., Batista, P. P., and Schuch, N. J. (2017). Equatorial E region electric fields and Sporadic E layer responses to the recovery phase of the November 2004 geomagnetic storm. *Journal of Geophysical Research: Space Physics*, 122:12517–12533.

Neubeck, K. E. (1996). Using the combined resources of amateur radio observations and ionosonde data in the study of temperate zone sporadic-E. *Journal of Atmospheric and Terrestrial Physics*, 58:1355–1365.

Nygrén, T., Aikio, A. T., Voiculescu, M., and Ruohoniemi, J. M. (2006). IMF effect on sporadic-E layers at two northern polar cap sites: Part II–Electric field. *Annales Geophysicae*, 24:901–913.

Rastogi, R. G. (1972). Equatorial Sporadic E Layer during Geomagnetic Storms. *J. Geomag. Geoelectr*, 24:429–440.

Reddy, C. A. and Matsushita, S. (1968). Solar cycle variation of blanketing sporadic E. *Journal of Geophysical Research*, 73:1641–1660.

Reinisch, B. W. and Galkin, I. A. (2011). Global ionospheric radio observatory (GIRO). *Earth, planets and space*, 63:377–381.

Resende, L. C. A., Batista, I. S., Denardini, C. M., Carrasco, A. J., Andrioli, V. D. F., Moro, J., Batista, P. P., and Chen, S. S. (2016). Competition between winds and

electric fields in the formation of blanketing sporadic e layers at equatorial regions 2. Aeronomy. *Earth, Planets and Space*, 68.

Rice, D. D., Sojka, J. J., Eccles, J. V., Raitt, J. W., Brady, J. J., and Hunsucker, R. D. (2011). First results of mapping sporadic E with a passive observing network. *Space Weather*, 9.

Ritchie, S. E. and Honary, F. (2009). Observations on the variability and screening effect of Sporadic-E. *Journal of atmospheric and solar-terrestrial physics*, 71:1353–1364.

Rostoker, G. (1972). Geomagnetic indices. *Reviews of Geophysics*, 10:935–950.

Saksena, R. C. (1974). Relationship between various types of Sporadic-E & magnetic activity. *Indian Journal of Radio & Space Physics*, 3:189–195.

Schreiner, B., Kuo, B., Rocken, C., Sokolovskiy, S., Hunt, D., Ho, B., Yue, X., Wee, T. K., Hudnut, K., Sleziak-Sallee, M., et al. (2014). COSMIC Data Analysis and Archive Center (CDAAC) current status and future plans.

Schreiner, W., Rocken, C., Sokolovskiy, S., Syndergaard, S., and Hunt, D. (2007). Estimates of the precision of GPS radio occultations from the COSMIC/FORMOSAT-3 mission. *Geophysical Research Letters*, 34.

Schunk, R. and Nagy, A. (2009). *Ionospheres: Physics Plasma Physics, and Chemistry*. Cambridge University Press, second edition.

Shinagawa, H., Miyoshi, Y., Jin, H., and Fujiwara, H. (2017). Global distribution of neutral wind shear associated with sporadic E layers derived from GAIA. *Journal of Geophysical Research: Space Physics*, 122:4450–4465.

Singer, W., von Zahn, U., and Weiß, J. (2004). Diurnal and annual variations of meteor rates at the arctic circle. *Atmospheric chemistry and physics*, 4:1355–1363.

Smith, E. K. (1957). *Worldwide Occurrence of Sporadic E.*, volume 582. US Department of Commerce, National Bureau of Standards.

Solomon, S. C. (2006). Numerical models of the E-region ionosphere. *Advances in Space Research*, 37:1031–1037.

Sugiura, M. (1963). Hourly values of equatorial Dst for the IGY.

SWPC (2021). Space Weather Prediction Center SWPC.

Thayaparan, T. and MacDougall, J. (2005). Evaluation of ionospheric sporadic-E clutter in an arctic environment for the assessment of high-frequency surface-wave radar surveillance. *IEEE transactions on geoscience and remote sensing*, 43:1180–1188.

UCAR (2018). COMET Layers of the Atmosphere and Ionosphere.

Voiculescu, M., Haldoupis, C., Pancheva, D., Ignat, M., Schlegel, K., and Shalimov, S. (2000). More evidence for a planetary wave link with midlatitude E region coherent backscatter and sporadic E layers. *Ann. Geophysicae*, 18:1182–1196.

Wei, Y., Hong, M., Wan, W., Du, A., Lei, J., Zhao, B., Wang, W., Ren, Z., and Yue, X. (2008). Unusually long lasting multiple penetration of interplanetary electric field to equatorial ionosphere under oscillating IMF Bz. *Geophysical Research Letters*, 35.

Whitehead, J. D. (1970). Production and prediction of sporadic E. *Reviews of Geophysics*, 8:65–144.

Wu, D. L., Ao, C. O., Hajj, G. A., Juarez, M. D. L. T., and Mannucci, A. J. (2005). Sporadic E morphology from GPS-CHAMP radio occultation. *Journal of Geophysical Research: Space Physics*, 110.

Yu, B., Xue, X., Kuo, C., Lu, G., Scott, C. J., Wu, J., Ma, J., Dou, X., Gao, Q., Ning, B., Hu, L., Wang, G., Jia, M., Yu, C., and Qie, X. (2019). The intensification of metallic layered phenomena above thunderstorms through the modulation of atmospheric tides. *Scientific Reports*, 9.

Zaalov, N. and Moskaleva, E. (2019). Statistical analysis and modelling of sporadic e layer over europe. *Advances in Space Research*, 64(6):1243–1255.

Zeng, Z. and Sokolovskiy, S. (2010). Effect of sporadic E clouds on GPS radio occultation signals. *Geophysical Research Letters*, 37.

Zhang, Y., Wu, J., Guo, L., Hu, Y., Zhao, H., and Xu, T. (2015). Influence of solar and geomagnetic activity on sporadic-E layer over low, mid and high latitude stations. *Advances in Space Research*, 55:1366–1371.

Zuo, X. and Wan, W. (2008). Planetary wave oscillations in sporadic E layer occurrence at Wuhan. *Earth Planets Space*, 60:647–652.

Appendix

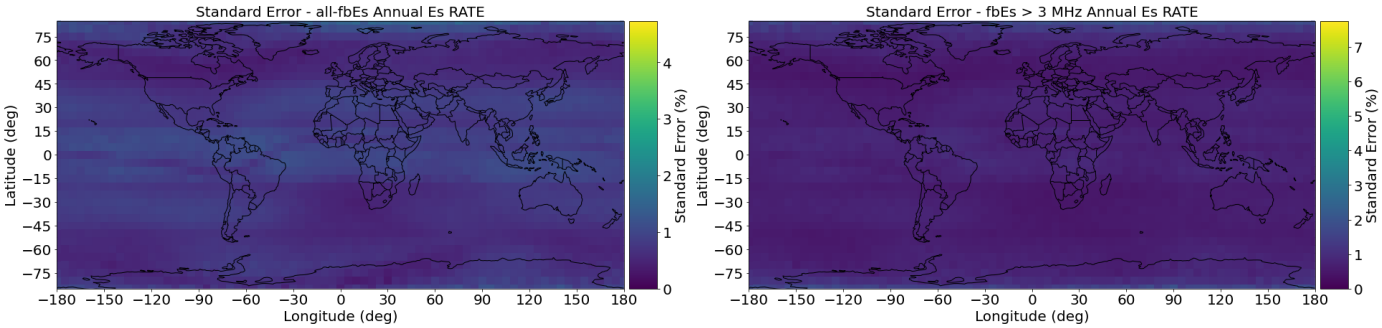

Figure 47. Standard error for the annual Es occurrence rates.

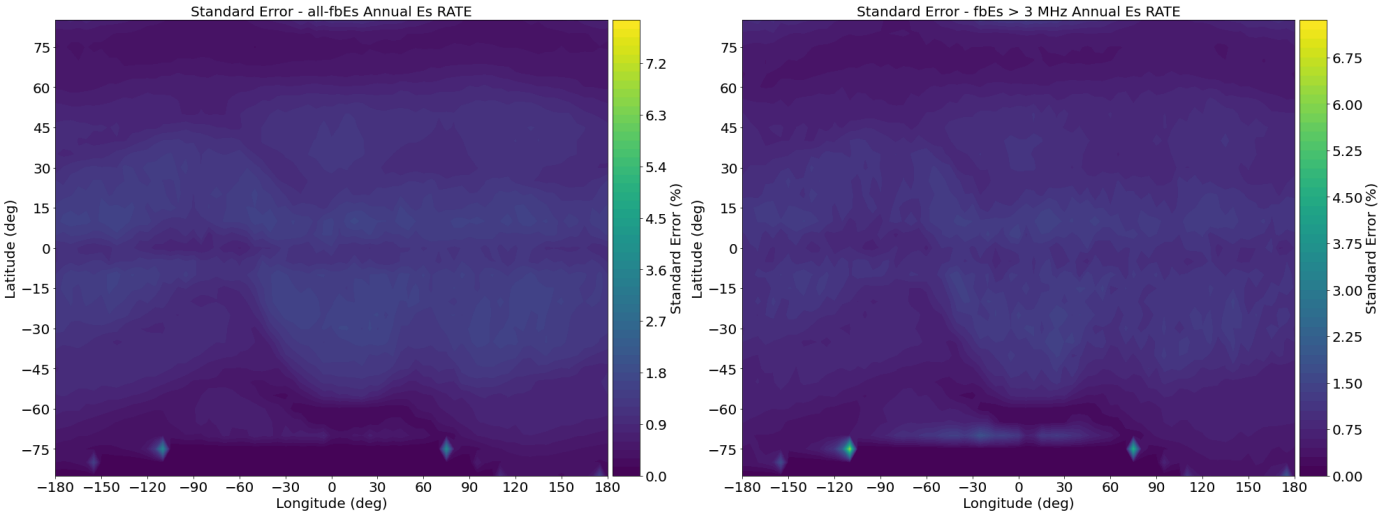

Figure 48. Standard error for the annual Es occurrence rates with geomagnetic adjusted coordinates.

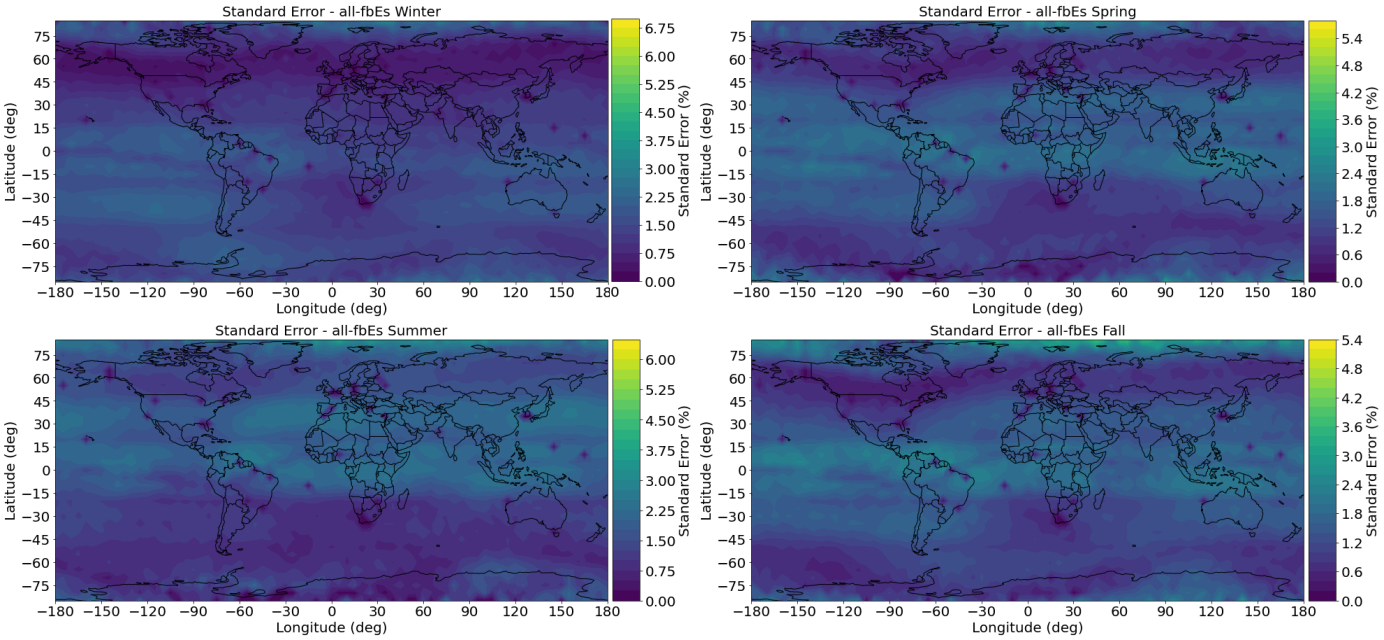

Figure 49. Standard error for the seasonal all-fbEs occurrence rates.

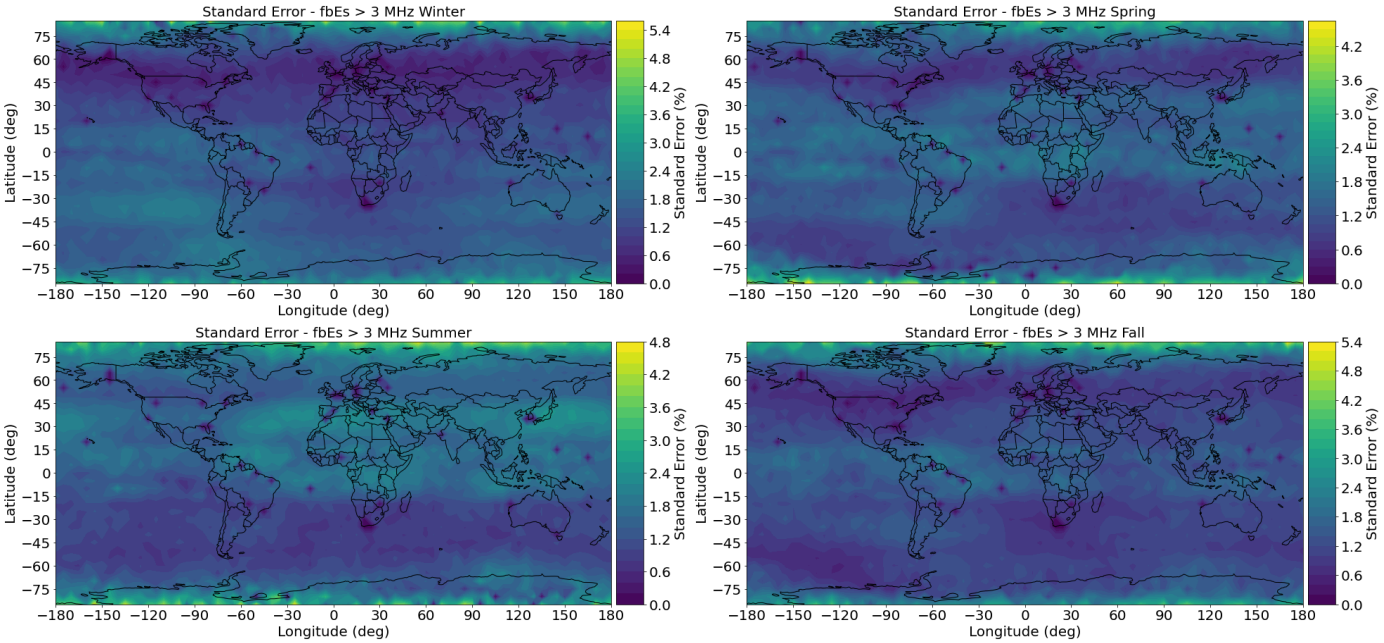

Figure 50. Standard error for the seasonal fbEs $\geq$ 3 MHz occurrence rates.

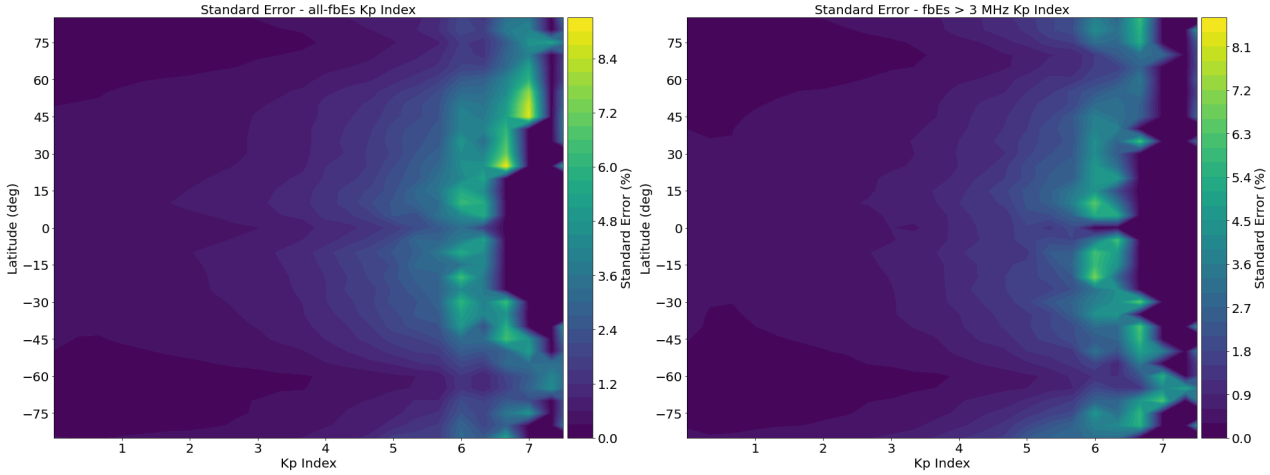

Figure 51. Standard error for the Es OR as a function of Kp and geomagnetic latitude.

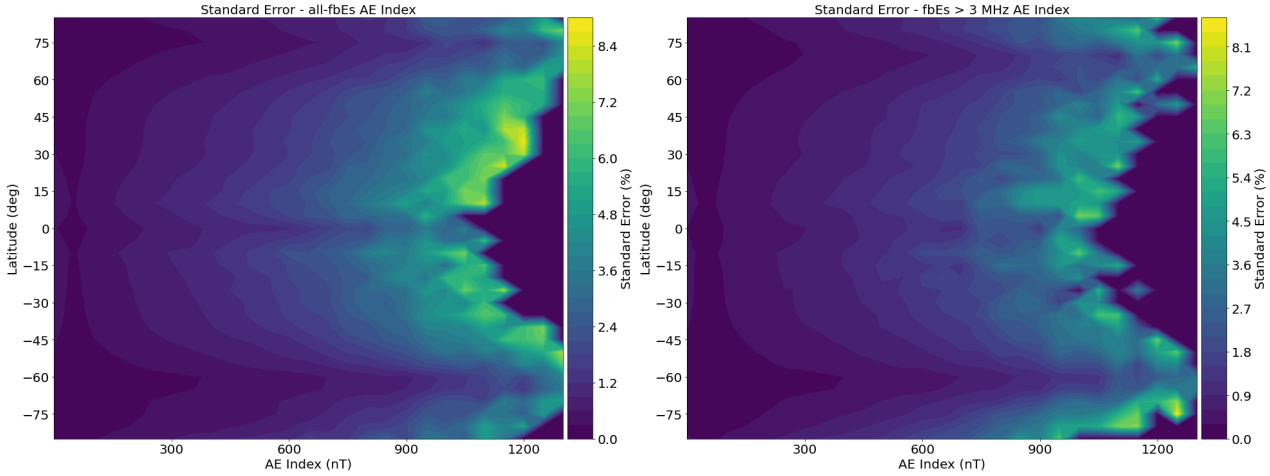

Figure 52. Standard error for the Es OR as a function of AE and geomagnetic latitude.

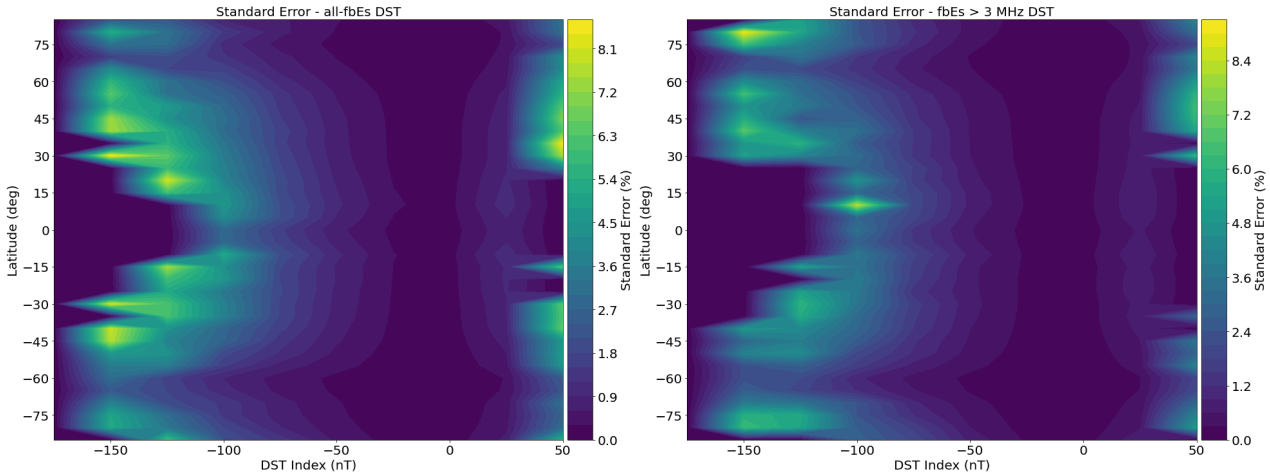

Figure 53. Standard error for the Es OR as a function of DST and geomagnetic latitude.

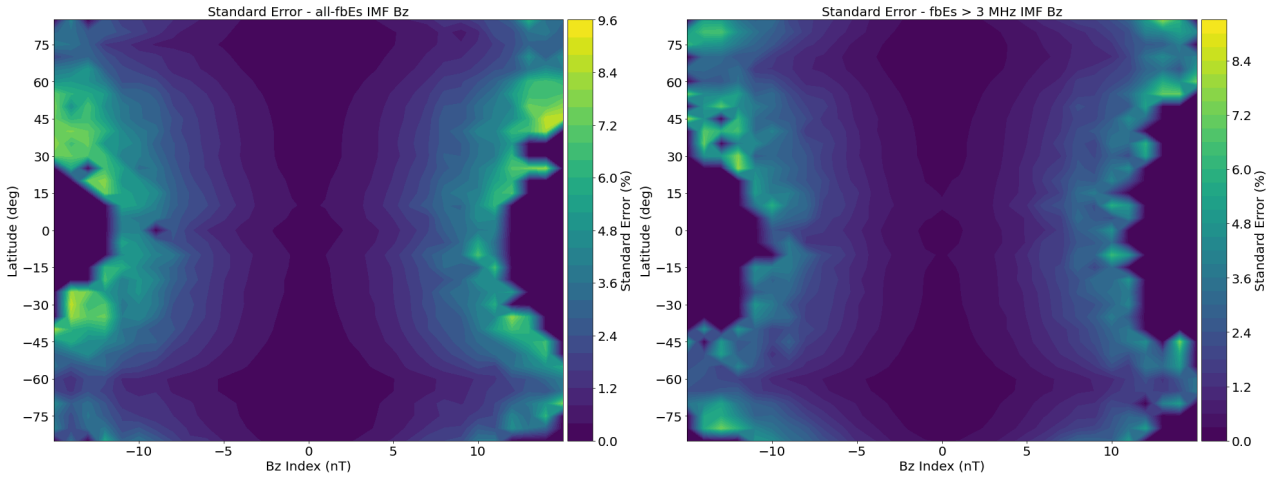

Figure 54. Standard error for the Es OR as a function of IMF Bz and geomagnetic latitude.

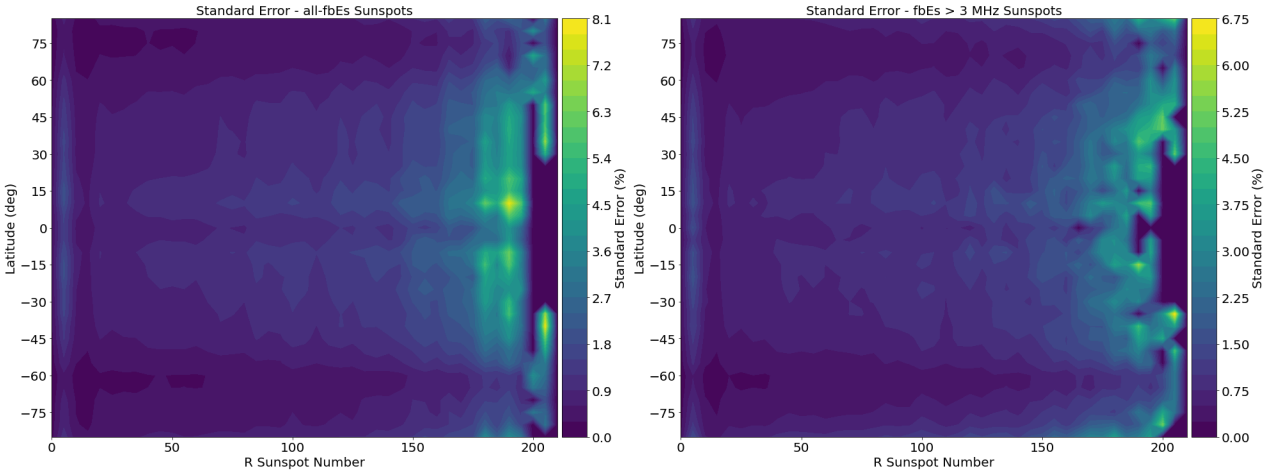

Figure 55. Standard error for the Es OR as a function of R sunspot number and geomagnetic latitude.

REPORT DOCUMENTATION PAGE

Form Approved
OMB No. 0704–0188

1. REPORT DATE *(DD–MM–YYYY)*	2. REPORT TYPE	3. DATES COVERED *(From — To)*
21–03–2022	Master's Thesis	May 2020 — Mar 2022

4. TITLE AND SUBTITLE

GLOBAL SPORADIC-E CLIMATOLOGICAL ANALYSIS USING GPS RADIO OCCULTAION AND IONOSONDE DATA

5a. CONTRACT NUMBER

5b. GRANT NUMBER

5c. PROGRAM ELEMENT NUMBER

6. AUTHOR(S)

Hodos, Travis John, Capt, USAF

5d. PROJECT NUMBER

5e. TASK NUMBER

5f. WORK UNIT NUMBER

7. PERFORMING ORGANIZATION NAME(S) AND ADDRESS(ES)

Air Force Institute of Technology
Graduate School of Engineering and Management (AFIT/EN)
2950 Hobson Way
WPAFB OH 45433-7765

8. PERFORMING ORGANIZATION REPORT NUMBER

AFIT-ENP-MS-22-M-096

9. SPONSORING / MONITORING AGENCY NAME(S) AND ADDRESS(ES)

Air Force Office of Scientific Research
Attn: Dr. Julie Moses
875 N. Randolph, Ste.325
Arlington Virginia, 22203
Phone: 703-696-7797
Email: info@us.af.mil

10. SPONSOR/MONITOR'S ACRONYM(S)

AFOSR/RTB1

11. SPONSOR/MONITOR'S REPORT NUMBER(S)

12. DISTRIBUTION / AVAILABILITY STATEMENT

DISTRIBUTION STATEMENT A:
APPROVED FOR PUBLIC RELEASE; DISTRIBUTION UNLIMITED.

13. SUPPLEMENTARY NOTES

14. ABSTRACT

A climatology of sporadic E (Es) derived from a combined data set of GPS radio occultation (GPS-RO) and ground-based ionosonde soundings is presented for the period from September 2006 to February 2019. The ionosonde soundings were measured using the Lowell Digisonde International (LDI) Global Ionosphere Observing Observatory (GIRO) network consisting of 65 sites and 13,141,060 total soundings. The GPS-RO observations were taken aboard the Constellation Observing System for Meteorology, Ionosphere, and Climate (COSMIC) satellites and processed using two binary Es detection algorithms, totaling 9,072,922 occultations. The first algorithm is an S_4 amplitude threshold calibrated to the occurrence of any blanketing Es (fbEs) with no lower limit on frequency, and the second is a threefold phase perturbation criteria calibrated to the occurrence of fbEs $\geq$ 3 MHz. It was found that Es primarily occurs in mid-latitude regions (10^o-60^o geomagnetic latitude) in the late afternoon and early evening (1500-2000SL)...

15. SUBJECT TERMS

GPS Radio Occultation, Sporadic-E, Ionosphere

16. SECURITY CLASSIFICATION OF:			17. LIMITATION OF ABSTRACT	18. NUMBER OF PAGES	19a. NAME OF RESPONSIBLE PERSON
a. REPORT	b. ABSTRACT	c. THIS PAGE			Maj Daniel J. Emmons, AFIT/ENP
U	U	U	U	99	19b. TELEPHONE NUMBER *(include area code)* (937) 255-3636, x4571; Daniel.Emmons@afit.edu